Progress in Materials Science 146 (2024) 101323

Contents lists available at ScienceDirect

Progress in Materials Science

journal homepage: www.elsevier.com/locate/pmatsci

Materials science-based guidelines to develop robust hard thin film materials

Paul H. Mayrhofer[a,*], Helmut Clemens[b], Franz D. Fischer[c]

[a] *Institutes of Materials Science and Technology, Technische Universität Wien (TU Wien), Getreidemarkt 9, 1060 Vienna, Austria*
[b] *Department Materials Science, Montanuniversität Leoben, Franz Josef Strasse 18, 8700 Leoben, Austria*
[c] *Institute of Mechanics, Montanuniversität Leoben, Franz Josef Strasse 18, 8700 Leoben, Austria*

ARTICLE INFO

Keywords:
PVD
Hard coatings
TiAlN
Thermal stability
Hardness
Fracture toughness
Oxidation resistance

ABSTRACT

For mechanically dominated load profiles, nitrides are preferred as the base material for structural and functional hard coatings, while oxide-based materials offer better protection against high-temperature corrosion (such as oxidation). Thus, when mechanical and thermal loads are combined, the nitrides used should also have excellent stability against temperature and oxidation. How to develop such nitride materials that can withstand both high mechanical and thermal loads is the focus of this review article. This is done primarily with the help of experimental and theoretical investigations of the Ti–Al–N system.

On the basis of transition metal nitride coatings, we discuss important material development guidelines for improved strength, fracture toughness as well as thermal stability and oxidation resistance. Using various superlattice coatings, we further discuss how such nanolamellar microstructures can improve both the strength and fracture toughness of hard coating materials. In addition, other concepts for improving fracture toughness are discussed, with a focus on those that can increase both fracture toughness and hardness.

The individual concepts allow to design materials to meet the ever-growing demand for coatings with a wide range of excellent properties and outstanding property combinations.

1. Introduction

The outstanding properties and property-combinations of transition metal nitrides (TMNs) – such as high strength, wear resistance, temperature stability, combined with chemical resistance – lend them their wide range of applications as structural, protective, and functional materials. In thin film or coatings form, they are used to protect machining tools and components (e.g., in automotive and aerospace industry) against sever abrasive, thermal, and corrosive loads, or they are used as functional layers (like for sensors) in microelectronics. Not to mention that thin films for the latter applications also need to be strong, tough, and thermally stable. Many of the TMNs (like TiN, NbN, TaN) are used as diffusion barriers or decorative coatings (especially TiN and ZrN). Further economic and ecological improvements in these areas requires that these materials become even more robust. For example, the cutting tools are usually the most stressed components in machining operations and limit the overall performance. Increasing the cutting speed (for economic reasons) leads to higher mechanical (e.g. bending stress) and thermal stress, which leads to increased wear of the tools and

---

* Corresponding author.
E-mail addresses: paul.mayrhofer@tuwien.ac.at (P.H. Mayrhofer), helmut.clemens@unileoben.ac.at (H. Clemens), fischer@unileoben.ac.at (F.D. Fischer).

https://doi.org/10.1016/j.pmatsci.2024.101323
Received 5 June 2023; Received in revised form 29 May 2024; Accepted 31 May 2024

their protective coatings [1–3]. At the application temperature, which easily exceeds 1000 °C at the cutting edge [4], hardness and strength must be maintained, and a certain toughness is required to prevent chipping and fracture, especially during interrupted cutting operations. The improved wear resistance enables an acceptable tool life before they need to be replaced. However, with increasing temperature, not only the strength of the materials decreases, but diffusion and chemical reactions are also promoted. Machining lubricants are used to alleviate these loadings, but they are often hazardous. In order to minimize or even avoid their use (for environmental and ecological reasons), the tool materials and protective coatings need to be stronger and have a higher thermal and corrosive stability to still allow a higher machining speed [1]; according to the motto “citius, altius, fortius”. Therefore, this review concentrates on understanding the mechanisms relevant for the strength of TMN-based materials and their thermal and chemical stability, and how these properties can be tuned. This is done with the help of experimental and theoretical investigations of the Ti–Al–N system. Its special features (discussed here in detail) make it both a most successful and important industrial coating system and a highly regarded scientific model system.

Surface and coating technologies have been used for a very long period to provide materials with properties that would otherwise be difficult or even impossible to achieve. For example, Pliny the Elder [5] reported already in the first century A.D. that thin metal-layers were applied to glass panes for the production of mirrors instead of simply polishing surfaces of metals. Usually, to protect against sea water, the wooden ancient ship hulls were coated with tar or other hydrophobic substances. Other examples are thin decorative gold coatings on less valuable base materials via various techniques such as mechanically or electroless plating [6], which have been practiced for thousands of years [7,8]. As effective barriers against environmental attacks, such gold coatings have also ensured that uncountable cultural treasures are still preserved today. Development of modern application-adapted materials requires detailed understanding of their intrinsic properties and how these can be combined most efficiently. Unlike diamond, which remains a highly valued material for various industrial applications (not only as jewelry), other technically important materials tend to obtain their optimized properties through alloy development and fine-tuning of their microstructure. For example, if both the hardness as well as toughness of materials need to be improved, it is necessary to optimize their microstructure and polycrystalline nature. A historical example of the crucial relevance of such structures for mechanical properties is “Damascus steel” or “Wootz steel” [9–11]. Developments and improvements of various materials can be based on classical design concepts as well as on new computer-aided methods [12–14].

The possibilities of surface modifications and the number of available coating materials have remarkably increased and are often the base for the innovative development of new components and tools. Thin films (i.e. coatings with thickness in the few nm to μm range) have been a technological driver in recent decades. As already mentioned, increased cutting speeds during machining lead to higher mechanical and thermal loads on the tool material and in particular its protective coating, which must be correspondingly more robust. Another example is that the higher temperatures in combustion processes and the necessary weight reductions of moving components require a knowledge-based coating solution for the applied materials. In this way, new materials help to improve the efficiency of technologies and costs of industrial processes, promoting a more economical and environmentally friendly use of resources. Such industrial and economic challenges heavily depend on advances in material developments and require innovative material concepts, such as the combination of structural base materials with coatings.

These together with achieving certain optical and electronic properties for specific applications in the microelectronics and optoelectronics industries are just a few examples of the industrial requirements met by thin-film technologies today. Important representatives of the latter are plasma-assisted physical vapor deposition (PVD) processes, such as sputtering or arc-evaporation, where the temperature T for synthesizing ceramic-like materials is typically below 0.2 of their melting point T_m (i.e. the homologous temperature $T/T_m < 0.2$). This leads to limited kinetics of adsorbed species during deposition and conditions far from thermodynamic equilibrium [15,16], allowing controlled synthesis of metastable phases and materials with improved mechanical and chemical properties with respect to their relatives [17]. Concerning these aspects, the development of Al-containing transition metal nitrides triggered a further improvement of the already excellent properties of TMNs [18–25].

The thermal stability of transition metal nitrides is strongly influenced by their defect structure, as recovery processes (e.g., defect annihilation and atomic rearrangements towards a lower energy configuration, which also leads to lower stress levels), interdiffusion, recrystallization, or phase transformation [21–23] occur during application at elevated temperatures. These phenomena are technologically relevant, since resulting structures and morphologies have a great influence on the coating properties. Novel hard coatings can also incorporate mechanisms based on phase transformations as in so-called TRIP steels (TRIP for transformation induced plasticity) or bulk ceramics [26].

For this reason, the present review article concentrates on the development of hard coatings allowing the important strengthening mechanisms to be active, while additionally improving oxidation resistance as well as fracture toughness. As mentioned at the beginning, these particular features are often decisive for the service life of the tools used, taking into account ecological, but also increasingly environmental aspects. We use $Ti_{1-x}Al_xN$ and their alloys as a model system to discuss the classical four strengthening mechanisms, all of which contribute to the high industrial relevance of these coatings. The temperature and time dependent evolution of their metastable and supersaturated phases is also discussed to provide a basic understanding of their age-hardening phenomena. In this context, density functional theory (DFT) calculations allow deeper insight and support modern materials development by their predictive nature and by explaining structure and property evolutions. The associated driving forces for the decomposition of supersaturated phases towards their thermodynamically stable constituent phases can be calculated [27]. Oxidation resistance of Ti–Al–N-based materials can also be improved with alloying concepts. Based on detailed investigations, we show that specific elements, particularly Ta, allow not only improving hardness but also thermal stability, oxidation resistance, as well as fracture toughness of $Ti_{1-x}Al_xN$ hard coatings.

With the help of superlattice and nanocomposite structures, allowing a simultaneous improvement in hardness and toughness, we conclude our review article. Important to mention to for such structures is the modification of TMNs through the combination with SiN_z and AlN, which additionally also improve their oxidation resistance. These can further be combined with alloying concepts to provide an additional boost.

2. Phase stability and mechanical properties

While binary transition metal nitrides continue to find widespread application, the kinetic limitations of low-temperature PVD processes also enable the development of more advanced coatings with metastable and even chemically unstable phases. Examples are the ternary Al-containing TMNs, as the model system used in this review, Ti–Al–N. Generally, increasing industrial demands for further improved coating systems with a wide range of properties and exceptional property combinations have driven the development of quaternary and multinary TMN-based hard coatings. However, this focus is not only based on chemical variation, but also on the associated microstructural changes. Those are the development of so-called superlattice coatings or nanocomposites, which allow increasing both hardness and fracture toughness [28–41].

2.1. Some basics of (Ti,Al)N coatings

Knotek et al. [18,19] and Münz [20] can be considered as the pioneers of $Ti_{1-x}Al_xN$ hard coatings. In fact, there are earlier reports about sputtered solid solution Ti–Al–N films [42,43], but Knotek et al. and Münz were one of the first reporting that substituting of Ti with Al improves the properties of TiN. In addition to improved oxidation resistance, the changed bond proportions and different atomic radii were expected to provoke solid solution strengthening, corresponding to the par-elastic (or first order elastic) and di-elastic (or second order elastic) interaction, due to atomic size and shear modulus misfit between solute and solvent atoms, respectively. The latter are considered in the classical Fleischer equation [44,45], which is applicable mainly to dilute alloys. The Labusch theory [46–49] extends the mathematical description to richer solutions. The most important theories express the solid solution strengthening as

$$\Delta\tau = AG\varepsilon^m c^n \tag{1}$$

with c the atomic concentration of the solvent, ε the elastic misfit parameter, G the shear modulus, A a fitting constant, m and n as concentration exponents (Fleischer [44,45]: $m = 3/2$, $n = 1/2$, and Labusch [46]: $m = 4/3$, $n = 2/3$). The elastic misfit parameter ε can be expressed as

$$\varepsilon = \sqrt{\eta'^2 + p^2\delta^2} \tag{2}$$

including the par-elastic interaction factor $\delta = \frac{1}{a}\frac{da}{dc}$ and di-elastic interaction factor $\eta' = \frac{\eta}{1+0.5|\eta|}$ with $\eta = \frac{1}{G}\frac{dG}{dc}$. The constant p is related to screw or edge dislocations (typical values for p are 3 for screw dislocations and 16 for edge dislocations). An overview of various expressions for ε is given in [50].

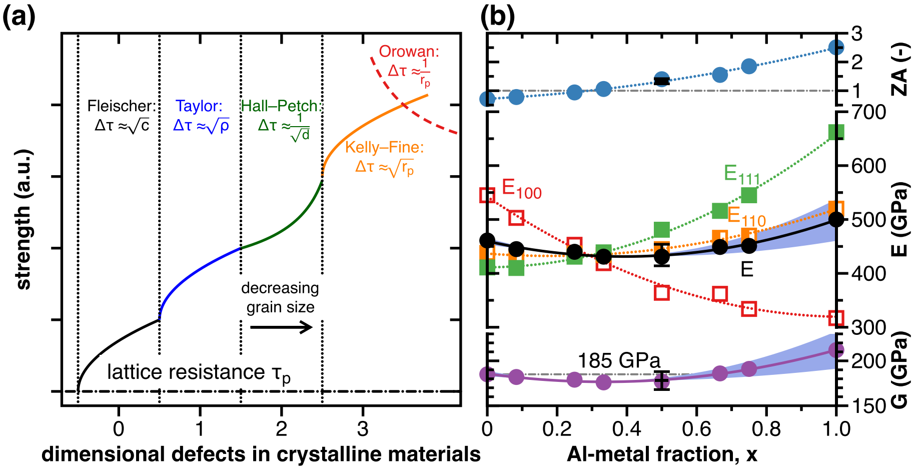

Fig. 1. (a) The classical four strengthening mechanisms based on the classical four defect categories: point, line, planar, and bulk defects, 0-, 1-, 2-, and 3-dimensional, respectively. The Peierls' barrier (lattice resistance) τ_P is 5.9 GPa for TiN [51] and 7.2 GPa for fcc-$Ti_{0.48}Al_{0.52}N$ [52]. (b) Calculated elastic properties, shear modulus, G, Young's modulus, E, of isotropic polycrystalline aggregates of fcc-$Ti_{1-x}Al_xN$. The actual values represent Hill's [53] averages, while the shaded areas demonstrate spread between Voigt [54] and Reuss [55] limits, for uniform strain and stress, respectively, calculated according to [56]. Additionally, the directional constants E_{111}, E_{110}, E_{100}, as well as Zener's anisotropy, $ZA = 2C_{44}/(C_{11} - C_{12})$ [57] are presented. The elastic constants C_{11}, C_{12}, and C_{44} to calculate these data are taken from [58,59]. The data-connecting lines are 2nd order polynomial fits, being $E = 459.7 – 144.8\cdot x + 184.3\cdot x^2$, $G = 185.6 – 53.9\cdot x + 80.4\cdot x^2$, and $ZA = 0.718 + 0.635\cdot x + 1.141\cdot x^2$. The error bar for G, E, and ZA at $x = 0.5$ is the standard deviation due to various configurations and supercell-sizes used in [59].

Essentially, all the classical four strengthening mechanisms (schematically presented in Fig. 1a) – which are based on the classical four defect categories – can be accessed with $Ti_{1-x}Al_xN$ coatings. The four classical defect categories in crystalline materials are point (interstitials, substitutional atoms, vacancies), line (dislocations), planar (grain-, phase-, and twin-boundaries, stacking faults), and bulk defects (precipitates, particles) with zero-, one-, two-, and three-dimensional geometry, respectively. Point defects – "solid solution strengthening" – are considered here with the simpler Fleischer equation, with its characteristic parameter of the solvent concentration c. Due to the approx. constant shear modulus of $G \approx 185$ GPa for fcc-$Ti_{1-x}Al_xN$ with $x \leq 0.7$ (see Fig. 1b) the di-elastic interaction factor η' is 0, which simplifies Eq. (1) for such solid solutions with the Fleischer exponents to $\Delta\tau = AGp^{\frac{3}{2}}\left|\frac{1}{a}\frac{da}{dc}\right|^{\frac{3}{2}}\sqrt{c}$. Actually, for fcc-$Ti_{1-x}Al_xN$ there a little difference exists between $\Delta\tau_L$ (Labusch) and $\Delta\tau_F$ (Fleischer), with $\Delta\tau_L = 1.33$ GPa and $\Delta\tau_F = 1.29$ GPa for $x = 0.5$, using $A = 0.038$ and $p = 10$ (thus, $\Delta\tau_F \cong 1.8\sqrt{c}$).

Each individual defect is an obstacle for the dislocation mobility. Consequently, an increased shear load ($\Delta\tau$) needs to be active on the dislocations to move them. The onset of dislocation glide separates the elastic from the plastic deformation (often represented by the yield stress σ_y). The minimum barrier, which needs to be overcome to move a dislocation (in the absence of thermal energy), is the Peierls' barrier τ_P, the lattice resistance against dislocation glide. Compared to a single-crystal (0 0 1) TiN bulk material (with $\tau_P = 5.9$ GPa [51]), a (close to single-crystalline) highly 200-oriented fcc-$Ti_{0.48}Al_{0.52}N$ coating (with $\tau_P = 7.2$ GPa [52]) exhibits a by ≈ 1.3 GPa larger lattice resistance.

Without dislocations – the only one-dimensional defects (line defects) but with various sorts of them like screw, edge, mixed, full, partial dislocations – crystals would be much stronger but also brittle. Dislocations give metals the invaluable properties of toughness and ductility and they do this also for nonmetallic crystals – but to a different extent as their Peierls' barrier is significantly larger. The concept of crystal dislocations dates back to 1934 when Taylor [60] (submission 7. February 1934), Orowan [61–63] (submission 5. April 1934), and Polanyi [64] (submission 2. Mai 1934) independently published their seminal work. Orowan and Polanyi knew of each other's work and referred to each other in their successive publications. Taylor [60] referred to Dehlinger's [65] "Verhakungen" – a translation of this German word could be "hookings" – when at the same time stayed with the name "dislocation". Other important historical contributions on that topic are [66–80].

The classical four strengthening mechanisms have in common that they impede the movement of dislocations. They are using either 0-, 1-, 2-, or 3-dimensional crystal defects and are named "solid solution strengthening", "strain hardening", "grain-refinement strengthening", and "particle strengthening". This shifts the yield point to higher values. "Strain hardening" is often named "work hardening" as typically in metals the density of dislocations ρ increases upon plastic deformation for example during metalworking processes. However, especially for PVD hard coatings the usage of "strain hardening" – which by the way was also named as such by Taylor [60] – seems to be more appropriate. Because the dislocation density of PVD coatings depends on the deposition conditions leading to different strains. In such hard coatings (like TiN), the dislocation density (number of dislocations per area or accumulated length of dislocations per volume) is comparable to strongly deformed steels and can be about 10^{17} m^{-2} [81]. The dislocation density – responsible for "strain hardening" – is considered in the Taylor relation [60]:

$$\Delta\tau_T = \beta G b\sqrt{\rho} \tag{3}$$

with b the magnitude of the Burgers vector and β an empirical factor. The higher ρ is, the shorter is the mean distance ($l = \frac{1}{\sqrt{\rho}}$, $\Delta\tau_T = \beta G b\frac{1}{l}$) between them and dislocation mobility is more difficult due to the appearing forest of dislocations. For TiN and fcc-$Ti_{1-x}Al_xN$ (with $x \leq 0.7$), $\Delta\tau_T$ amounts to 0.18–1.76 GPa (for $\rho = (1\text{–}100)\cdot 10^{15}$ m^{-2}), with $G \approx 185$ GPa, $b \approx 3$ Å, and $\beta = 0.1$. The relevant slip directions in these fcc-crystals are $\langle 110\rangle$, thus, the magnitude of b is ≈ 3 Å, i.e. half of the unit cells face-diagonal [52]. Together with the Peierls' barrier, $\tau \approx 6.08\text{–}7.66$ GPa and 7.38–8.96 GPa for TiN and fcc-$Ti_{0.50}Al_{0.50}N$, respectively, with such dislocation densities.

Planar defects (2-dimensional) are for example considered by the classical Hall–Petch relation [82,83]:

$$\Delta\tau_{HP} = k\frac{1}{\sqrt{d}} \tag{4}$$

with d for the grain size. Fine-grained materials provide more grain boundaries that hinder dislocation movement than coarse-grained ones. Typically, low-angle grain boundaries are less effective, but twin boundaries and phase boundaries are extremely effective. The Hall–Petch constant k might be even larger for nano-twinning than for grain-refinement, for which d would be the mean distance of twin boundaries, but the Hall–Petch type relationship breaks down earlier [84]. This is because the transition from dislocation-mediated deformation towards a deformation dominated more by interfacial activities occurs at a larger critical twin boundary distance than grain size [84–86]. Important note here: for metallic materials, this is the only strengthening mechanism allowing to increase ductility as well [87]. The others typically reduce ductility.

Last but not least the bulk defects, which are considered for example in the Kelly–Fine mechanism (Eq. (5) where dislocations would cut through coherent particles [88]) and the Orowan mechanism (Eq. (6) where dislocations bypass non-coherent or coherent particles [89], which leaves dislocation rings around them and thus in addition also strain-harden the crystal). The general forms of their equations are [90]:

$$\Delta\tau_{KF} \cong \frac{\widetilde{\gamma}^{\frac{3}{2}}}{b}\frac{\sqrt{r_p\cdot f_p}}{\sqrt{3Gb^2}} =$$

$$\Delta\tau_{KF} \cong \frac{\widetilde{\gamma}^{\frac{3}{2}}}{b}\frac{\sqrt{r_p}}{\sqrt{3Gb^2}}\frac{r_p}{D} \tag{5}$$

$$\Delta\tau_O = \frac{Gb}{D-2r_p}\alpha =$$

$$\Delta\tau_O \cong \frac{Gb\sqrt{f_p}}{r_p}\alpha \tag{6}$$

with r_p for the particle radius, f_p the particle volume fraction, and $\widetilde{\gamma}$ an effective surface energy ($\widetilde{\gamma} \cong \gamma_p + 2\Delta\gamma_{SF} + \gamma_{APB} + \gamma_\delta$, with interface energy between particle and matrix γ_p, stacking fault energy difference $\Delta\gamma_{SF}$ between particle and matrix, antiphase boundary energy γ_{APB}, par-elastic contribution in form of a surface energy term $\gamma_\delta = Gb\delta$). D is the mean distance of the forming particles (from center to center, so that D–$2r_p$ is the free dislocation length between particles) that retain the dislocations ($D \approx \frac{r_p}{\sqrt{f_p}}$ for constant particle volume fraction and $r_p \ll D$). The strength of the particle is represented by α, with $\alpha = \cos\frac{\phi}{2}$, where ϕ is the pinning angle of the dislocation line due to the interaction with the particles ($\frac{\phi}{2} = 0$ for impenetrable obstacles and 90° for weak ones). Consequently, α is between 1 and 0. Incoherent particles are always by-passed by dislocations, whereas coherent ones can be cut or by-passed, depending on their size. The critical domain size r_c for obtaining the peak-strength can be estimated with $\Delta\tau_{KF} = \Delta\tau_O$ to:

$$r_c \cong \frac{Gb^2}{\widetilde{\gamma}}\sqrt[3]{3\alpha^2} \tag{7}$$

For smaller domains, the Kelly–Fine mechanism (cutting through, Eq. (5)), is preferred, and for larger ones, the Orowan mechanism (by-passing, Eq. (6)) is preferred, see Fig. 1a.

There are various modifications to the original Orowan relation, Eq. (6), to consider the interaction of statistically distributed particles with screw and/or edge dislocations. The modification is of the general form [91]:

$$\Delta\tau_{AO} \cong \frac{1}{2\pi\sqrt{1-\nu}}\frac{0.81Gb}{(D-2r_p)}\ln\frac{r_p}{b} \tag{8}$$

with the Poisson's ratio ν and $\frac{1}{2\pi\sqrt{1-\nu}}$ being the geometric mean for edge and screw dislocations. Comparing Eqs. (6) and (8) shows that $\alpha \cong \frac{0.81}{2\pi\sqrt{1-\nu}}\ln\frac{r_p}{b}$, which is ≈ 0.13 for $\nu = 0.25$ and $r_p = 0.7$ nm.

Tabor was the first to propose a relationship between hardness and elastic limit Y_e ($H \cong CY_e$) – considering the von Mises flow criterion: that yielding under multi-axial conditions initiates when the elastic distortion energy reaches the same value as obtained for the uniaxial yield stress σ_y. For Vickers hardness C is 2.9–3.0 and Y_e is a representative value of the elastic limit around the indentation [92], corresponding to σ_y. Due to the indentation, the material will experience work hardening and Tabor found a representative deformation degree for Vickers of 8–10 %. For the provided values, Tabor mentions "the elastic limit Y_e being found from careful compression experiments" [92]. But C depends on the geometry of the indenter (especially its angle) [93,94] and the Y_e/E ratio of the material tested [95,96]. For a fully work-hardened steel, C increases nearly linearly from 2.3 to 2.9 with increasing cone-angle from 100 to 160°. A cone with a semi-angle β of 70.3° displaces the same volume as a Vickers or Berkovich indenter for the same penetration depth [97]. For $Y_e/E > 0.02$, C values below 2.4 are obtained [95]. For hard ceramic coatings like TiN (with $H \approx 20$ GPa [98], 21.2 GPa [52], 19.7 GPa [99], and $E \approx 463$ GPa [98], 430 GPa [99] for bulk TiN, as well as $Y_e \approx 14$ GPa for a Ti(C,N) coating [100]), Y_e/E is around 0.025, for which C would be 2.4 [95]. A detailed calculation with these parameters gives $C \approx 2.4$ after [52,101] and:

$$C = \frac{2}{3}\left\{1 + \frac{3}{3-6\lambda} ln\left(\frac{(3+2\mu)[2\lambda(1-\zeta)-1]}{2\lambda\mu-3\mu-6\lambda}\times\frac{1}{\zeta}\right)\right\} \tag{9}$$

with $\zeta = \left[\frac{E}{E-2(1-\nu^2)H\tan\beta}\right]$, $\lambda = \frac{(1-2\nu)Y_e}{E}$, $\mu = \frac{(1+\nu)Y_e}{E}$, where β is the semi-angle of the equivalent cone indenter. The more convenient approximation given by [101] again gives $C \approx 2.4$ with:

$$C \cong \frac{2}{3}\left\{1 + \ln\left[\frac{E}{3(1-\nu)Y_e}\right]\right\} \tag{10}$$

neglecting second-order terms in Y_e/E, which is valid for $Y_e/E < 0.1$ (thus, most materials).

Atkins and Tabor [93] provided also the relationship between H and the principal shear stress τ ($H \cong C_0\tau$), with $C_0 = \sqrt{3}C$ considering the von Mises yield criterion (with the Tresca criterion this would be $C_0 = 2C$; however, the von Mises criterion is preferred as a smooth, viable, completely general, as well as modern failure criterion) [102–104]. Thus, C_0 is around 4.2 for the Vickers hardness of hard ceramic coatings like TiN. Using these considerations, we can also write for such hard (TiN-like) materials:

$$\Delta H \cong 4.2\Delta\tau \tag{11}$$

The factor 4.2 agrees well with that for a cone-angle of ≈ 140° given in [93,105]. For completeness and because we recently encountered a confusion and incorrect usage: the von Mises yield criterion (which relates the multi-axial stress state of a material to an equivalent uniaxial stress) states that for pure shear the critical resolved shear stress τ_{crss} in the plane of flow is $\frac{1}{\sqrt{3}}$ of the uniaxial yield stress σ_{y} ($\tau_{crss} = \frac{1}{\sqrt{3}}\sigma_{y}$). The Tresca criterion states a factor of $\frac{1}{2}$. These should not be confused with the Schmid factor m, which gives the ratio between the uniaxial normal stress σ and the active shear stress τ for a slip system, in the shear-direction at the plane of shear, for single crystals ($\tau = m\sigma$). Thus, the Schmid factor depends strongly on the relative orientation of the single crystal to σ and varies between 0 and 0.5 [106,107]. The Sachs model [108] or the Taylor model [109] extend this to polycrystalline materials by treating the polycrystal as an agglomerate of single crystals, with the grains subjected to the same stress or strain, respectively. They are typically considered as lower and upper bounds of the corresponding M factor ($\sigma = M\tau$), which is, for example, 2.23 or 3.06 for a random orientation of fcc single crystals according to Sachs or Taylor, respectively [110]. Consequently, the M factor allows the estimation of τ_{crss} in a polycrystal based on σ_{y} obtained, for example, by micromechanical compression or tensile tests. Often the arithmetic mean of the two extremes for M is taken [111], corresponding to Hill's averages [53].

Interestingly, many of the basic mathematical descriptions dealing with plasticity and flow (such as Schmid's law, von Mises' flow criterion, Volterra's elastic fields around dislocation-like defects) are older than the concept of dislocations.

Using Eq. (11) and the above-mentioned variation of τ for TiN and fcc-$Ti_{0.50}Al_{0.50}N$, 6.08–7.66 GPa and 7.38–8.96 GPa (for dislocation density variations of (1–100)·10^{15} m^{-2}), their calculated hardness variation is 25.54–32.17 GPa and 31.00–37.63 GPa, respectively. These values are in perfect agreement with reported hardness variations of these materials, depending on the PVD parameters used [28,112]. If fcc-$Ti_{0.5}Al_{0.5}N$ is seen as a solid solution alloy of TiN, the above mentioned estimation according to Fleischer, $\Delta\tau_{\text{F}}$ of 1.29 GPa ($\Delta H \approx 5.24$ GPa), can explain their difference in τ_{P} and hardness. A pronounced reduction in grain size could further increase their hardness due to grain-refinement strengthening, discussed in more detail later in Chs. 2.2.2 and 2.2.3. While these first three strengthening mechanisms seem to be obvious for the Ti–Al–N alloy system, the latter require the realization that fcc-$Ti_{1\text{-}x}Al_{x}N$ coatings can contain highly supersaturated phases, which is a prerequisite for precipitation hardening (or age hardening).

In fact, such $Ti_{1\text{-}x}Al_{x}N$ coatings are not only superior to binary TiN coatings in hardness, oxidation resistance, and wear resistance [19,20,24,113–119], they also outperform TiN with their thermomechanical properties. In thermodynamic equilibrium, the solubility of AlN in TiN is very limited (<2 % at 1000 °C [120]). TiN crystallizes in the face-centered cubic fcc B1, NaCl prototype structure, while AlN crystallizes in the hexagonal close-packed hcp B4, wurtzite prototype structure. However, physical or chemical vapor deposition processes allow the synthesis of supersaturated $Ti_{1\text{-}x}Al_{x}N$ films with AlN mole fractions as high as $x = 0.9$ [121]. The kinetic limitation in the condensation of the vapor (condensation from the gas phase can be estimated with cooling rates up to 10^{13} K/s [122]) allows the synthesis of such supersaturated $TM_{1\text{-}x}Al_{x}N$ solid solutions. Due to a high deposition rate, the condensed regions are quickly overgrown and, thus, the thermodynamic equilibrium cannot be achieved even by the typically much higher surface diffusion. In other words, the "freezing" from the gas phase does not allow the condensing atoms to reach a stable configuration characterized by a maximum formation energy [123].

The supersaturated cubic structure is maintained due to limited diffusion. However, segregation of the supersaturated structure inevitably occurs when diffusion is sufficiently activated at elevated temperatures (e.g. in the case of application during machining processes). This induces spinodal decomposition in the $Ti_{1\text{-}x}Al_{x}N$ system, resulting in the formation of TiN-rich and AlN-rich fcc structured domains. The associated microstructural change leads to a hardness increase corresponding to the precipitation hardening. The phase transformation of the metastable fcc structured AlN-rich domains to the thermodynamically stable hcp-AlN modification also requires overcoming an additional energetic barrier, which is mainly due to the associated elastic distortion. A phase transformation from fcc-AlN to hcp-AlN would lead to a volume change of 26 % without external constraints [124,125]. Such a transformation, which typically occurs by shearing and resembles a martensitic-like transformation [126], can therefore only take place if the matrix also yields to deformation [127], e.g. by plastic deformation for which shearing is needed, which is particularly facilitated at higher temperatures.

The existence-ranges in terms of temperature and Al content of supersaturated mixed crystals in some quasibinary nitride systems

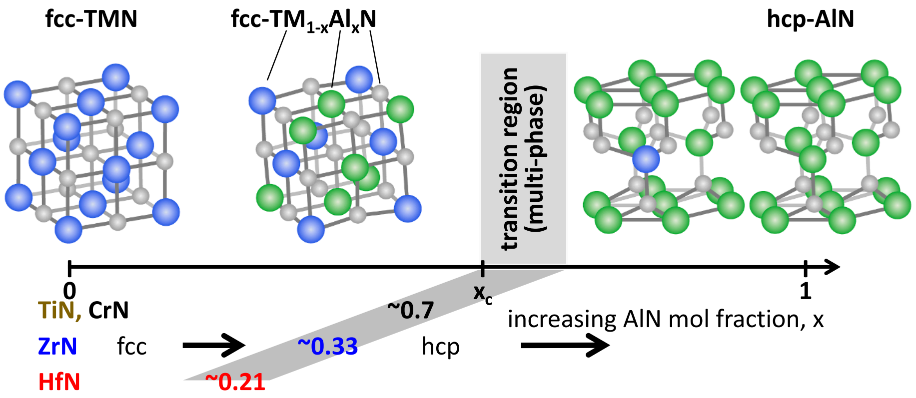

Fig. 2. Schematic representation of structure evolution in $TM_{1\text{-}x}Al_{x}N$ as a function of their Al metal-fraction x. The structure-transition from fcc (B1, NaCl-type) to hcp (B4, ZnS-wurtzite-type) $TM_{1\text{-}x}Al_{x}N$ solid solutions occurs at a critical value, x_c, which varies for different TMNs, adapted from [137,140].

were first defined by Holleck [123]. Since then, extensive research (both, experimentally and computationally) focused on details of the structural existence-ranges for many different $TM_{1-x}Al_xN$ systems, like $Ti_{1-x}Al_xN$ [24,30,128–137], $Cr_{1-x}Al_xN$ [113,137–146], $Zr_{1-x}Al_xN$ [137,147–151], or $Nb_{1-x}Al_xN$ [137,152,153]. Particularly, mechanical properties and oxidation resistance of $TM_{1-x}Al_xN$ hard coatings improve with their Al content as long as their fcc structure is maintained. This is only possible up to a certain critical Al content, x_c, above which the formation of the hcp structure is increasingly favored, see Fig. 2. Due to the different bonding ratios within various $TM_{1-x}Al_xN$ systems, the x_c values vary with the different TMNs.

The hcp crystallization of $TM_{1-x}Al_xN$ solid solutions or AlN reduces their mechanical properties, leading to lower hardness and wear resistance [113,115,131]. The presence of only a small fraction of hcp-AlN-based phases within an otherwise fcc-dominated matrix is not necessarily deteriorating the mechanical properties, as shown for $Ti_{1-x}Al_xN$ [154,155]. This behavior originates essentially on the precipitation strengthening (Fig. 1a, Eqs. (5) and (6)), but the presence of such nucleation sites for hcp-AlN-based phases initiates their rapid growth and promotes further decomposition of the fcc-$TM_{1-x}Al_xN$ solid solutions towards thermodynamic equilibrium, especially for Al-rich compositions.

As mentioned above, due to the extremely limited kinetics during synthesizing materials via PVD techniques, supersaturated $Ti_{1-x}Al_xN$ solid solutions are accessible [18–20,24–43,114,156,157], although fcc-TiN and hcp-AlN actually show no solubility for each other, see their quasibinary diagram, Fig. 3a [123]. The *ab initio* calculated formation energies E_f for fcc and hcp $Ti_{1-x}Al_xN$ solid solutions show that up to $x \approx 0.6–0.7$ the fcc structure is energetically favored, see Fig. 3b. In the concentration range where similar E_f values exist for both structures, a two-phase structure is to be expected [130,132,150,158,159]. The corresponding change in the mixed crystal regions (based on experimental observations by Spencer [160]) is shown by dashed lines for $Ti_{1-x}Al_xN$ in Fig. 3a.

$Ti_{1-x}Al_xN$ can be considered as a model system in materials science of thin films, because not just hardness, oxidation resistance, and thermal stability increase with the Al content x [30,130,131,158,161–168] – if synthesized as single-phase fcc – but also structural changes are possible upon annealing, which trigger age hardening effects. Thus, all four classical strengthening effects discussed above are accessible. $Ti_{1-x}Al_xN$ hard coatings form a dense, stable and protective Al_2O_3-based oxide layer especially for high Al contents, x. The incorporation of Al into other binary transition metal nitrides (TMNs, such as TM = V, Cr, Zr, Nb, Hf, Ta [113,118,147,148,150,152,169–173]) is comparable, both in terms of the formation of metastable phases and in terms of the superior properties of the ternary compounds when compared to the binary nitrides. With increasing Al content of the supersaturated fcc phase the driving force for its decomposition also increases pronouncedly. This is necessary for the structural changes/adaptations at elevated temperatures, triggering age hardening effects that lead to their extraordinary properties.

The preparation of hard coatings via PVD results in a very high defect density, such as point defects and line defects. This also leads to significant intrinsic (growth-induced) compressive stresses [23], and large stored driving forces for atomistic and structural changes, supporting recovery or recrystallization. Such diffusion-driven processes are activated as soon as sufficient energy is available and kinetics allow, typically at sufficiently high temperatures. The latter can also occur, for example, during the application of the materials (e.g. during machining processes). Usually, the temperatures required for this activation are above the deposition temperatures of the hard coatings [174,175]. The reduction in defect density leads to a significant decrease in hardness of these coatings, because there are fewer defects that could impede the mobility of the dislocations [21,23,28,176].

However, if the hard material layers have over-saturated solid solutions, as is the case for example with $Ti_{1-x}Al_xN$, then the hardness decrease can be counteracted or even over-compensated by the almost simultaneous spinodal decomposition [28,177–181]. Measurements at temperatures of up to 300 °C have shown that the hot hardness of $Ti_{1-x}Al_xN$ is clearly superior to that of TiN [52]. The domains formed via spinodal decomposition are effective obstacles to dislocation motion and, thus, also cause an increase in hardness [12,90]. For this reason, hard coatings containing Al-containing fcc $TM_{1-x}Al_xN$ solid solutions are superior to their binary counterparts

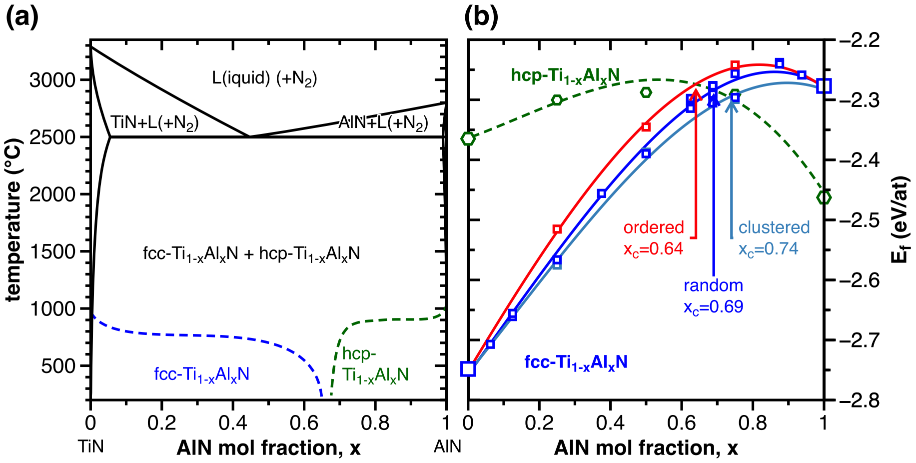

Fig. 3. (a) Quasibinary TiN–AlN phase diagram, modified from [123]. (b) Ab initio formation energies, E_f, obtained for the fcc and hcp crystal structure of the $Ti_{1-x}Al_xN$ solid solutions (adapted from Ref. [129]). The extended existence-regions of the vapor-deposited fcc and hcp $Ti_{1-x}Al_xN$ solid solutions are indicated by dashed lines in (a); based on experiments [160] and ab initio phase boundaries.

in terms of thermomechanical properties [19,20,113–119].

The TiN–AlN phase diagram exhibits a very wide miscibility gap, where even at ≈ 2500 °C only a few at% Al is soluble in TiN (essentially no Ti in AlN), see Fig. 3a. As mentioned, however, PVD techniques in particular allow the synthesis of enormously supersaturated fcc-$Ti_{1-x}Al_xN$ solid solutions, with a maximum Al metal-fraction of typically 66 at%. The resulting materials science capabilities justify the excellent performance of this coating system, especially when used at elevated temperatures [124]. Simplified, such supersaturated fcc-$Ti_{1-x}Al_xN$ solid solutions can be imagined as two interconnected fcc sublattices, one fully occupied by nitrogen and the other partially occupied by Al and Ti [129] (or: a fcc metal lattice, where the fcc positions are occupied by the metals Ti and Al and all octahedral interstices are occupied by N, see Fig. 2).

Knowledge of structure and distribution of atoms allows the calculation of the formation energy E_f of the fcc-$Ti_{1-x}Al_xN$ solid solutions and, consequently, of the enthalpy of mixing (ΔH_{mix}) of the ternary compounds with respect to the binary constituents fcc-TiN and fcc-AlN. This immediately yields the stored energy, i.e. the driving force contained in such solid solutions for segregation into the binary components fcc-TiN and fcc-AlN, see Fig. 4a [123,136,182]. From the calculated *G*–*x* curve and its dependence on the temperature, the binodal and the chemical spinodal (the additional consideration of the coherence stresses leads to the coherent spinodal, which always includes a smaller range; here these are drawn for 1 and 4 nm large domains) can be calculated for the quasibinary TiN–AlN phase diagram, according to Refs. [129,134,136], see Fig. 4b. In the region within the spinodals, the second derivative of the Gibbs free energy is negative ($\partial^2 G/\partial x^2 < 0$) and, thus, the smallest compositional fluctuations (fcc-$Ti_{1-x}Al_xN$ → fcc-$Ti_{1-x-\Delta x}Al_{x+\Delta x}N$ + fcc-$Ti_{1-x+\Delta x}Al_{x-\Delta x}N$) already lead to a reduction of the Gibbs free energy. Within this range, the chemical potential of Ti for Ti-richer solid solutions is smaller than for Ti-poorer ones, and correspondingly the chemical potential of Al for Al-richer solid solutions is smaller than for Al-leaner ones. Thus, a decomposition of the initially relatively homogeneous fcc-$Ti_{1-x}Al_xN$ solid solution into Ti-rich and Al-rich fcc-$Ti_{1-x}Al_xN$ crystals occurs, insofar as the necessary solid-state diffusion allows this [124,177,184].

Due to the diffusion of the metal (Me) atoms against their concentration gradients, this is also often referred to as "uphill diffusion". The region of spinodals is clearly limited by the coherence stresses that may be induced (in our example, there is a significant lattice-parameter reduction of fcc-$Ti_{1-x}Al_xN$ with increasing Al content) [124]. In the region outside the binodal, a fcc-$Ti_{1-x}Al_xN$ solid solution is stable; between the binodal and spinodal, the fcc-$Ti_{1-x}Al_xN$ solid solution is metastable, and decomposition toward the global minimum requires nucleation and growth. The positive mixing enthalpy ΔH_{mix} over the entire composition range shows that the fcc-$Ti_{1-x}Al_xN$ solid solutions have a very high driving force stored for decomposition into their fcc-TiN and fcc-AlN constituents (Fig. 4a, lines symbolized with a square). With increasing compressive stresses (symbolized here by the dashed line labelled 10 GPa), the driving force for this segregation is even higher (Fig. 4a).

This is because the lattice parameter of the fcc-$Ti_{1-x}Al_xN$ solid solutions is larger than the arithmetic mean of the corresponding fcc-TiN and fcc-AlN constituents [124] (positive deviation from Vegard's rule [186]). The situation is different when the decomposition of the fcc-$Ti_{1-x}Al_xN$ solid solutions into their thermodynamically stable phases fcc-TiN and hcp-AlN is considered. Here, there is a significant decrease in ΔH_{mix} with increasing compressive stresses, Fig. 4a (lines symbolized with a hexagon). This is due to the fact that the thermodynamically stable hcp-AlN phase occupies a significantly larger volume (about + 26 %) than its metastable fcc modification (which is also known as the high-pressure modification of AlN) [124,181,185,187]. Accordingly, the maximum AlN content, x_c, of the fcc structure is also highly dependent on the acting stresses, see Fig. 4c. Compressive stresses favor the fcc-$Ti_{1-x}Al_xN$ phase. In other words, as long as the matrix is strong enough, any phase-transformation of fcc-AlN-rich regions towards their thermodynamically stable hcp-AlN variant is hampered. Because, as soon as fractions of fcc-AlN transform to hcp-AlN, the associated volume increase leads

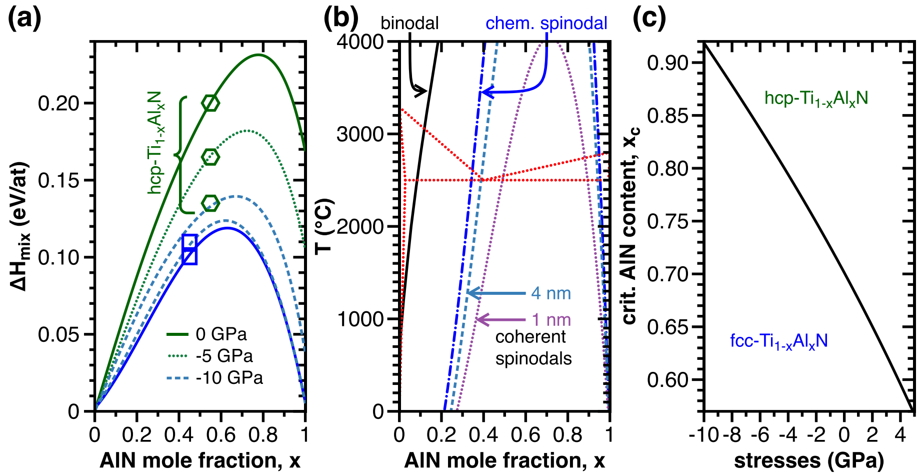

Fig. 4. (a) Mixing enthalpies ΔH_{mix} of fcc-$Ti_{1-x}Al_xN$ (from fcc-TiN and fcc-AlN, symbolized with a square; and from fcc-TiN and hcp-AlN, symbolized with a hexagon) as a function of AlN content, x, at different compressive stresses (adapted from Refs. [182,183]. (b) Phase diagram with binodal (fcc-$Ti_{1-x}Al_xN$ → fcc-TiN and fcc-AlN, its fcc-structured constituents) and chemical spinodal. The influence of coherence stresses at 1 and 4 nm domains is also shown (coherent spinodals) [181]. (c) Critical AlN content, x_c, of the fcc-$Ti_{1-x}Al_xN$ solid solutions as a function of the stresses (negative values indicate compressive stresses) [185].

to a significant increase in compressive stresses. These, if not released via dislocation slip or twinning, hinder any further fcc-AlN → hcp-AlN transformation.

The dependence of the stored driving force in fcc-$Ti_{1-x}Al_xN$ solid solutions on composition, temperature, vacancies, tensile or compressive stresses, as well as surface energies has been extensively studied both computationally [129,134,181,182,185,188] and experimentally [28,180,181]. In general, ΔH_{mix} increases with Al content up to about $x = 0.66$ and compressive stresses favor the fcc structure, see Fig. 4c. A comprehensive overview of the structural change of $Ti_{0.46}Al_{0.54}N$ hard coatings as a function of temperature and time is shown in the work of Rachbauer et al. [155,189].

Materials that have a large single-phase field, such as TiN, and whose hardness-increase has been achieved by a very high defect density (as in our example by the incorporation of point as well as line defects due to the PVD process) experience a softening under thermal loading (Fig. 5, usually as soon as the deposition temperature is exceeded) due to the onset of recovery and recrystallization processes. In contrast, the supersaturated fcc-$Ti_{1-x}Al_xN$ solid solutions allow a significant increase in hardness with increasing temperature, or at least a nearly stable hardness, Fig. 5a. Spinodal decomposition allows the Ti- and Al-rich fcc-$Ti_{1-x}Al_xN$ regions that form to be very homogeneously distributed throughout the matrix and their average spacing is also very small (≈ 3 nm [190,191]), at least initially [28,181,190,191]. This allows to obtain a maximum strength increase ($\Delta\tau$) based on the Orowan mechanism (Eq. (6)). Coarsening of the structure, loss of coherence stresses between fcc-TiN and fcc-AlN, and the onset of hcp-AlN formation lead to a steady decrease in hardness at high temperatures, typically above 900–1000 °C [28].

The mean spacing as well as the size of the forming domains change with time and temperature, and thus the associated increase in strength is also time and temperature dependent [23,184,194]. The time-dependent change in H for $Ti_{0.41}Al_{0.59}N$ during vacuum-annealing at 900 °C is given in Fig. 5b. The dash-dotted line indicates that the sweet-spot (for highest hardness) could have been missed by the relatively coarse intervals of 1, 120, and 480 min. The critical domain size for $Ti_{0.50}Al_{0.50}N$ to obtain the peak-strength can be estimated with Eq. (7) to be $r_c \approx 2.5$ nm, using a shear modulus G of 185 GPa (for $Ti_{0.50}Al_{0.50}N$ as well as for $Ti_{0.45}Al_{0.55}N$), magnitude of the Burgers vector b of 3 Å, $\alpha = 0.13$ and an effective surface energy $\widetilde{\gamma}$ of 2.4 J/m^2 (for which the major contributions are taken as $\gamma_p = 0.18$ J/m^2 [124] and the par-elastic surface contribution $\gamma_\delta = 2.20$ J/m^2).

A rough estimation of the possible strength-increase due to the Orowan mechanism (with $\alpha = 0.13$, as discussed when presenting Eq. (6)) results in $\Delta\tau_O \approx 4.38$ GPa (mean distance between Al-rich domains $D \approx 3$ nm [190,191] and an average particle size $2r_p = 1.4$ nm [181] for the ≈ 900 °C annealed sample, after 1 min). For such conditions, the Kelly–Fine mechanism, Eq. (5), would lead to $\Delta\tau_{KF} \approx 0.34$ GPa. Even if the mean distance between particles would be taken as the distance between Al-rich and Ti-rich ones (thus $D \approx 1.5$ nm), $\Delta\tau_{KF}$ would only double and be ≈ 0.68 GPa. Thus, definitely, the easier Kelly–Fine mechanism would be active, especially considering that it is highly unlikely that the small coherently formed domains are impenetrable for the dislocations. Even if the effective surface energy $\widetilde{\gamma}$ would be 3-times larger, $\Delta\tau_{KF}$ would "only" be ≈ 3.56 GPa for $D \approx 3$ nm and $2r_p = 1.4$ nm). Furthermore, for the situation that the matrix remains with $Ti_{0.45}Al_{0.55}N$ out of which Ti-rich and Al-rich domains form simultaneously, the remaining matrix would not experience a loss in solid solution strengthening. And for such a scenario, the mean distance of the forming particles would be 1.5 nm as mentioned above, causing the Orowan contribution (with $\alpha = 0.13$) to increase even to $\Delta\tau_O \approx 70.00$ GPa. The time dependent hardness evolution presented in Fig. 5b was obtained by using the smaller value of either $\Delta\tau_{KF}$, Eq. (5), or $\Delta\tau_O$ (Eq. (6) with $\alpha = 0.13$) calculated for a time-dependent evolution of particle size r_p [124,195], along with a volume fraction of these particles of $f_p = 0.3$ (for which $D \approx 2r_p$, thus representing the distance between Ti-rich and Al-rich domains). Additionally, the Taylor contribution $\Delta\tau_T$,

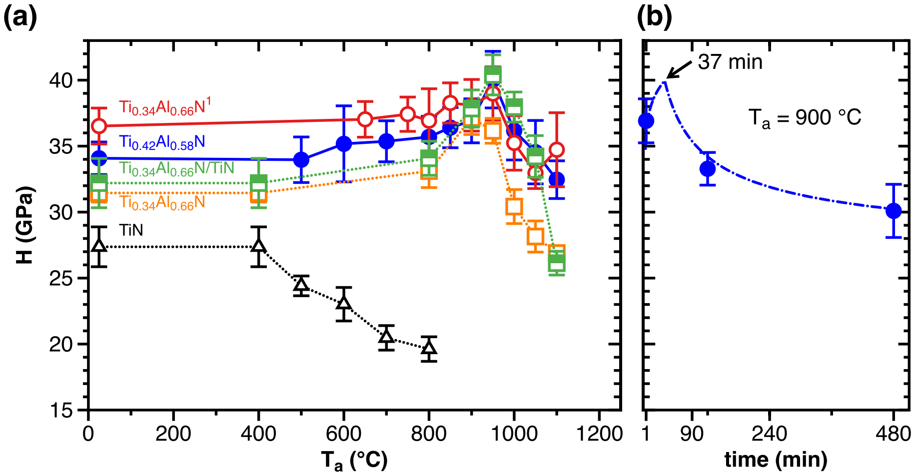

Fig. 5. (a) Hardness versus annealing temperature, T_a, for arc-evaporated TiN and $Ti_{0.34}Al_{0.66}N$ coatings and $Ti_{0.34}Al_{0.66}N/TiN$ multilayer (adapted from [192], the data for $Ti_{0.34}Al_{0.66}N^1$ are from [28]; these coatings were annealed 120 min at T_a in flowing Ar), as well as sputtered $Ti_{0.42}Al_{0.58}N$ (vacuum-annealing for 1 min at T_a). The increase in hardness with temperature is due to the formation of new domains, which are effective barriers to dislocation movement. (b) Hardness evolution with annealing time for $Ti_{0.41}Al_{0.59}N$ (vacuum-annealing at 900 °C) [193]. The dash-dotted line is an estimation based on strengthening according to Kelly–Fine $\Delta\tau_{KF}$, Eq. (5), and Orowan $\Delta\tau_O$, Eq. (6) with α = 0.13, and weakening according to a reduction in dislocation density (Taylor strengthening $\Delta\tau_T$, Eq. (3)).

Eq. (3), continuously reduced due to the reduced dislocation density upon annealing, see next paragraphs.

Fig. 6 shows the evenly and fine distributed formation of Al-rich domains upon the spinodal decomposition of $Ti_{0.50}Al_{0.50}N$, using a scanning TEM (STEM) investigation of a specimen annealed at 850 °C for 120 min. Detailed investigations yield that the compositional wavelength stays constant at ≈ 2.8 nm for the first 20 min and then increased to 5.8 nm after 120 min [190].

For smaller domains, the Kelly–Fine mechanism (cutting through, Eq. (5)) is preferred, and for larger ones, the Orowan mechanism (by-passing, Eq. (6)) is preferred. Fig. 7a – using the kinetics presented in [124,195] – shows that this critical particle size (being independent on f_p) is reached with ≈ 35 min during annealing at 900 °C (this is where $\Delta\tau_{KF}$ and $\Delta\tau_O$ cross). But for spinodally decomposed structures a more sophisticated scenario should be considered as well. The strength increase $\Delta\tau$ can be estimated for spinodal decomposition of fcc alloys [196,197] considering the size misfit:

$$\Delta\tau_{sp,s} = a_c\delta Y/\sqrt{6} \tag{12}$$

with $3a_c$ for the amplitude of the sinusoidal concentration modulation (which is 0.12 for the 900 °C annealed sample [181]) and $Y = (C_{11} - C_{12})(C_{11} + 2C_{12})/C_{11}$ representing a function of the cubic elastic constants C_{11} and C_{12} (for $Ti_{0.50}Al_{0.50}N$ $Y = 493$ GPa) yields $\Delta\tau_{sp,s} = 0.33$ GPa.

The composition modulation also leads to a modulus misfit, which can be estimated as [196]:

$$\Delta\tau_{sp,m} = 0.65\Delta Gb/\lambda \tag{13}$$

with λ for the modulation period and ΔG for the shear modulus misfit. For $Ti_{0.50}Al_{0.50}N$, with $\lambda \approx 8$ nm (after 60 min at 900 °C [190]) and $\Delta G \approx 8$ GPa (difference between $Ti_{0.35}Al_{0.65}N$ and $Ti_{0.65}Al_{0.35}N$, as Al-rich and Ti-rich fcc-structured domains form), $\Delta\tau_{sp,m}$ is calculated to be ≈ 0.20 GPa. If λ would be ≈ 3 nm, as obtained after ≈ 3 min at 900 °C [190,191], the λ-dependent contribution $\Delta\tau_{sp,m}$ (Eq. (13)) to the strength-increase by spinodal decomposition ($\Delta\tau_{sp}$) would increase to ≈ 0.52 GPa. Thus, $\Delta\tau_{sp}$ ($\Delta\tau_{sp,s} + \Delta\tau_{sp,m}$) would be ≈ 0.85 and 0.52 GPa for the 3 and 60 min annealed sample with $\lambda = 3$ and 8 nm, respectively. The maximum possible concentration amplitude and shear modulus difference (decomposition into fcc-TiN and fcc-AlN, $\Delta G \approx 26$ GPa and $3a_c = 0.5$) would lead to $\Delta\tau_{sp} = 3.08$ or 2.01 GPa for $\lambda = 3$ or 8 nm, respectively. For the time-dependent evolution of $\Delta\tau_{sp}$, the time-dependent evolution of the sinusoidal concentration-modulation-amplitude ($3a_c = 0.05$, 0.12, and 0.29 for $t = 0.2$, 1, and 120 min, respectively, at $T_a = 900$ °C [155]; fitted here with a power law: $3a_c = 0.09t^{0.25}$; with t in min) was used.

Fig. 7a shows that the course of $\Delta\tau_{KF}$ is similar to that of $\Delta\tau_{sp}$, and overlaps when using $f_p = 0.3$ and $\lambda = 2.4$ nm, respectively. Their cross-over with $\Delta\tau_O$ ($f_p = 0.3$) at the critical domain size (reached after 37 min) suggests for a peak-strengthening of $\Delta\tau_p \approx 1.54$ GPa for the 900 °C-annealed $Ti_{0.50}Al_{0.50}N$. The peak strengthening $\Delta\tau_p$ (cross-over between $\Delta\tau_{KF}$ and $\Delta\tau_O$, thus actually $\Delta\tau_O$ having a particle size of $r_c = 2.5$ nm) for increasing particle fraction f_p is also added. For this, f_p is assumed to follow the same time-dependence as the sinusoidal concentration-modulation-amplitude $3a_c$ ($f_p = 0.09t^{0.25}$; with t in min), to have $f_p \approx 0.45$ after 480 min. Converting a $\Delta\tau$ increase by ≈ 1.54 GPa (being $\Delta\tau_p$ with increasing f_p after 130 min, Fig. 7a) to a hardness increase, Eq. (11) yields $\Delta H \approx 6.47$ GPa. Perfectly explaining the measured hardness increase by ≈ 6.0 GPa, see Fig. 5a for $T_a \approx 950$ °C or Fig. 7b for $Ti_{0.46}Al_{0.54}N$ (#1) at 800 °C, $Ti_{0.34}Al_{0.66}N$ (#5) at 900 °C, and $Ti_{0.34}Al_{0.66}N$/TiN (#6) at 950 °C after $t = 120$ min.

Very often such a hardness gain is not observed. The above-mentioned considerations and discussions for explaining the hardness increase due to the spinodal decomposition make it clear, that easily the peak-hardness can be missed, or compensated by other softening-effects. The latter are for example the rearrangement of defects such as dislocations towards lower energy sites, leading to a reduction in dislocation density ρ, which reduces the Taylor strengthening contribution $\Delta\tau_T$. For example, with Eq. (3), $\Delta\tau_T = 1.76$ GPa

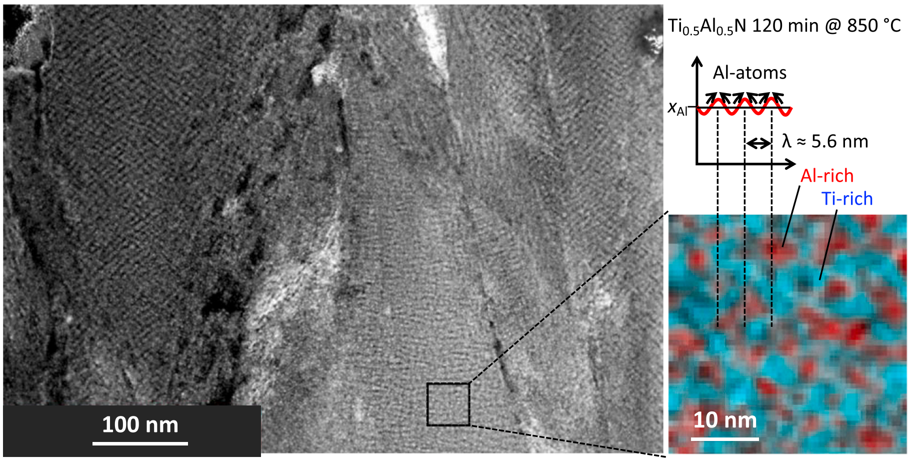

Fig. 6. Cross-sectional high-angle annular dark-field STEM overview of $Ti_{0.50}Al_{0.50}N$ after isothermal annealing for 120 min at 850 °C. The elemental map by energy dispersive scanning shows the Al-rich (red) and Ti-rich (blue) regions. The autocorrelation function yields a compositional wavelength λ of 5.6 nm. Adapted from [190]. (For interpretation of the references to colour in this figure legend, the reader is referred to the web version of this article.)

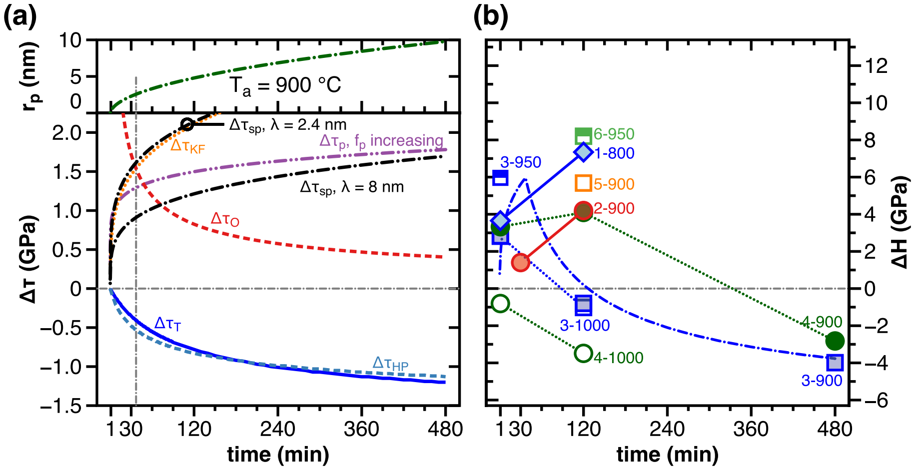

Fig. 7. Calculated and measured strength increase of (Ti,Al)N during isothermal annealing. (a) Evolution of the particle radius r_p of fcc-$Ti_{0.34}Al_{0.66}N$ during annealing at 900 °C [124,195], and the thereby calculated strengthening according to Kelly–Fine $\Delta\tau_{KF}$, Eq. (5), and Orowan $\Delta\tau_O$, Eq. (6) with $\alpha = 0.13$, for particle volume fraction f_p of 0.3. $\Delta\tau_{sp}$ for spinodally decomposed structures using the size misfit $\Delta\tau_{sp,s}$, Eq. (12), and modulus misfit $\Delta\tau_{sp,m}$, Eq. (13), are added for $\lambda = 2.4$ and 8.0 nm. $\Delta\tau_{KF}$ ($f_p = 0.3$) overlaps with $\Delta\tau_{sp}$ for $\lambda = 2.4$ nm. The cross-over between $\Delta\tau_{KF}$ and $\Delta\tau_O$, gives the critical particle size ($r_c \approx 2.5$ nm) – which is independent on the particle fraction f_p (see also Eq. (7)) – at which peak-strength $\Delta\tau_p$ is obtained. The evolution of $\Delta\tau_p$ ($=\Delta\tau_{KF}$ with r_c) with a time-dependent increasing f_p is given by the dash-dot-dot line. A possible reduction in the dislocation density ρ from 10^{17} m^{-2} (as-deposited value [81]) to $1\cdot10^{16}$ m^{-2} (after 480 min at 900 °C) causes the Taylor strengthening $\Delta\tau_T$, Eq. (3) to decrease by 1.20 GPa. Upon grain growth from 20 to 120 nm, the Hall–Petch contribution $\Delta\tau_{HP}$ decreases by ≈ 1.13 GPa. (b) Hardness change ΔH (with respect to the as-deposited state) during isothermal annealing of $Ti_{0.46}Al_{0.54}N$ (#1) [155] at 800 °C, $Ti_{0.34}Al_{0.66}N$ (#2) [198] at 900 °C, $Ti_{0.41}Al_{0.59}N$ (#3) at 900 °C [193], 950 and 1000 °C (unpublished), $Ti_{0.41}Al_{0.56}Ta_{0.03}N$ (#4) [193] at 900 and 1000 °C, $Ti_{0.34}Al_{0.66}N$ (#5) at 900 °C and $Ti_{0.34}Al_{0.66}N$/TiN (#6) at 950 °C [192]. The range of the ΔH-axis is 4.2-times that of the Δτ-axis (with the 0-line at level), according to Eq. (11).

for fcc-$Ti_{0.50}Al_{0.50}N$ (with $G = 185$ GPa and $b = 3$ Å) with a dislocation density of $\rho = 1\cdot10^{17}$ m^{-2} [81]. If ρ decreases to $1\cdot10^{16}$ m^{-2}, $\Delta\tau_T$ decreases to 0.56 GPa. The time-dependent reduction in dislocation density during an isothermal annealing can be obtained after [199] with:

$$\rho = 1/\left(\frac{1}{\rho_0} + c_1 t\right) \tag{14}$$

with ρ_0 being the initial dislocation density and c_1 a temperature-dependent time constant.

The kinetics of (sub)grain growth during isothermal treatment follow the general form of [199]:

$$d^n = {d_0}^n + c_2 t \tag{15}$$

with d and d_0 for the grain size at time t and 0, respectively, c_2 a temperature-dependent time constant, and n the growth exponent (frequently between 2 and 4). For $n \approx 2$, Eq. (15) has a form similar to that used to describe grain growth following recrystallization [199]. For the following simple estimation of the Hall–Petch contribution $\Delta\tau_{HP}$, $d_0 = 20$ nm and $d = 120$ nm (at $t = 480$ min) were used. With $n = 2$, c_2 would become 29 min^{-1}, which allows to obtain a time-dependent grain size evolution. This can be fed to Eq. (4) to obtain the time-dependent $\Delta\tau_{HP}$ evolution, presented in Fig. 7a. A simple estimation of the Hall–Petch constant k, needed in Eq. (4), was done with data published for Ti–B–N in Ref. [200]. There, a hardness reduction ΔH of ≈ 14.7 GPa upon a grain coarsening from ≈ 2–3 to 9 nm, without significant changes of the phases present, is given. Using ≈ 4 GPa for other annealing-induced hardness reduction processes leaves the Hall–Petch constant for a hardness change, k_H, with ≈ 35.8 GPa·$nm^{0.5}$, after:

$$k_H = \frac{\Delta H_{HP}}{\frac{1}{\sqrt{d_2}} - \frac{1}{\sqrt{d_1}}} \tag{16}$$

where d_1 is the large grains size (9 nm) and d_2 the smaller (≈ 2–3 nm). For comparison, $k_H = 9.7$ GPa·$nm^{0.5}$ for nanocrystalline Cu [201], 16.1 GPa·$nm^{0.5}$ for gradient structured Ni [202], 18.7 GPa·$nm^{0.5}$ for electrodeposited Ni [203], 19.1 GPa·$nm^{0.5}$ for Al–ZnO composites [204], and 33.4 GPa·$nm^{0.5}$ for an $MgAl_2O_4$ spinel ceramic [205]. The latter is in excellent agreement with our k_H of 35.8 GPa·$nm^{0.5}$ for nitride ceramic-like thin films, which with Eq. (11) corresponds to a k of 8.5 GPa·$nm^{0.5}$ for $\Delta\tau_{HP}$. Thus, upon grain-growth from 20 to 120 nm, the Hall–Petch contribution $\Delta\tau_{HP}$ decreases by 1.13 GPa during annealing for 480 min. Together with the reduction of the Taylor contribution $\Delta\tau_T$ by ≈ 1.20 GPa, the recovery-induced softening ($\Delta\tau \approx -2.33$ GPa, $\Delta H \approx -9.8$ GPa) can compensate the gain ($\Delta\tau_p = 1.54$ GPa for $f_p = 0.30$) due to the newly-formed domains. For TiN, where no strengthening processes are active during annealing, the value of ≈ 10 GPa fits to the hardness decrease during annealing of initially very hard coatings having ≈ 30 GPa [112,206], as indicated in Fig. 5a. Due to specific deposition processes, TiN can contain a high defect concentration, such as a dislocation density of ≈ 10^{17} m^{-2} [81], lending them the high hardness. TiN bulk ceramic would have $H \approx 20$ GPa [99]. Similarly, the hardness and compressive stress reduction by ≈ 4.5 GPa upon annealing TiN for 120 min at 700 °C [112] would also fit to the reduction in Taylor contribution $\Delta\tau_T$ by ≈ 1.20 GPa (equivalent to a 5.0 GPa hardness reduction).

What is yet to be considered for (Ti,Al)N is that the above-mentioned scenario considers the formation of Ti-rich and Al-rich domains, leaving the chemical composition of the remaining matrix unchanged and, thus, also its solid solution strength. If only Al-rich domains would form, the solid solution strengthening effect would decrease by $\Delta\tau_F \approx 0.38$ GPa (when the matrix changes from $Ti_{0.45}Al_{0.55}N$ to $Ti_{0.65}Al_{0.35}N$). If only Ti-rich domains would form, which causes an increase in the Al-content of the remaining matrix, there would be almost the same change (now we need to use fcc-AlN as the starting composition and Ti as its solvent and with Eqs. (1) and (2) the difference in $\Delta\tau_F$ between $Ti_{0.45}Al_{0.55}N$ and $Ti_{0.35}Al_{0.65}N$ is 0.35 GPa). However, the latter scenario is not very likely, as the diffusion of Al is higher than that of Ti.

The occurrence and interplay of these individual strengthening and weakening processes contribute to the measured hardness change ΔH (from the respective hardness in the as-deposited state) upon annealing (Ti,Al)N. A representative ΔH variation for some (Ti,Al)N coatings during isothermal vacuum annealing at 800, 900, 950, and 1000 °C is given in Fig. 7b. The gain in hardness can be as high as +8.0 GPa and the softening about –4.0 GPa. With Eq. (11) this would correspond to $\Delta\tau$ of about +1.9 and –1.0 GPa, corresponding to the discussed strengthening and softening processes. Comparison with measured hardness changes renders the calculated contributions relevant.

Fig. 7b also shows that the peak-hardness is sometimes only reached when annealed for longer times than 30 min. Especially the 800 °C annealed sample (#1) allows for the highest hardness gain (+8 GPa) of this comparison, which is obtained only after 120 min. That lower temperature annealing (but for longer time) can lead to higher peak-strengths is a known behavior especially for age-hardenable Al-alloys. Only when adjusting a more complex microstructure, like that of $Ti_{0.34}Al_{0.66}N$/TiN (#6), a similar hardness gain can be obtained even when annealed at 950 °C for 120 min, see Fig. 7b. The combination of $Ti_{0.34}Al_{0.66}N$ with TiN is also a combination of materials with nearly reversed E_{111}/E_{100} ratio (1.43 vs 0.75), Fig. 1b. Interesting is also the hardness evolution for $Ti_{0.41}Al_{0.59}N$ (#3), which seems to be identical when annealed at 900 and 1000 °C. However, a comparison with Fig. 7a (temperature dependence) and the specimen annealed at 950 °C, indicates that the evolution at 900 °C is more in line with the simulated one (added to Fig. 5b and 7b as dash-dotted lines).

These processes – which at least are responsible for a maintained hardness of fcc-$Ti_{1-x}Al_xN$ coatings even if they experience a thermal treatment at 900–1000 °C – contribute to the improved performance during machining processes as compared to TiN, which softens significantly (Fig. 5). The improved performance of (Ti,Al)N was already shown in 1987 by Knotek, Münz, and Leyendecker [207], showing also their massively improved oxidation resistance as compared to TiN. They further raised the question in their conclusion: "what needs to be done to prevent the rapid decline in performance of (Ti,Al)N coated drills at higher cutting speeds", see the reproduced Fig. 8a using data from [207].

Now that it is evident which microstructural changes are present in (Ti,Al)N upon a thermal exposure (next to oxidation, which is definitely important as well for the ability of tribo-film formation [208,209] and thermal stability, as discussed later in Ch. 3), it is understandable why (Ti,Al)N can increase its performance upon an increase in cutting speed (equivalent to an increased thermal exposure). The additional strengthening mechanisms – activated by the newly formed domains upon spinodal decomposition of the supersatuared matrix – allow for an increased number of drilled holes upon increasing the cutting speed from 30 to 35 m/min, see Fig. 8a. Hörling et al. [117], correlated the increased tool life of (Ti,Al)N protected square-shaped face milling inserts during machining of a 42CrMo4 steel with the increased Al content of single-phased fcc-structured coatings, as thereby both hardness and thermal stability increase. A drastic life-time reduction was obtained as soon as the Al content exceeded 66 at% (of the metal sublattice) due to the concomitant formation of hcp-AlN-based phases. Chen et al. [198] showed later that the performance of (Ti,Al)N can

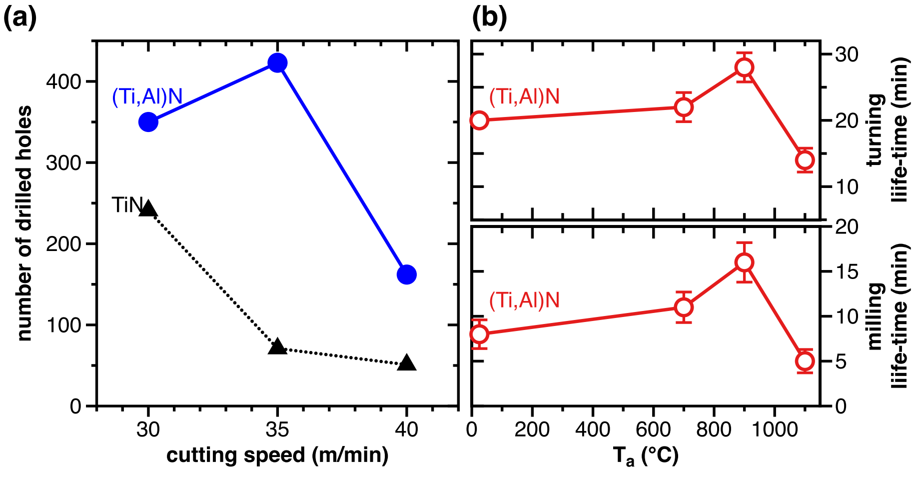

Fig. 8. (a) Drilling test conducted on 34CrNiMo6 (AISI4340) steel, adapted from [207]. (b) Life-time of $Ti_{0.34}Al_{0.66}N$ coated inserts during continuous turning of 1Cr18Ni9Ti (X12CrNiTi18.9, AISI321) stainless steel and milling of 42CrMo (42CrMo4, AISI4140) steel after annealing at T_a, adapted from [198].

in fact be improved upon a pre-annealing step (Fig. 8b), which initiates age-hardening. Again, as soon as the formation of hcp-AlN-based phases is noticeable, the life-time decreases.

As presented and discussed for Fig. 5, a too high thermal exposure causes the phase transformation of the Al-rich domains towards wurtzite structured hcp-AlN, leading to a rapid decline in hardness. This can be transferred to the rapid decline in performance of (Ti, Al)N for cutting speeds beyond 35 $m\cdot min^{-1}$, respectively the decline in life-time during milling and turning of inserts that have been annealed at temperatures beyond 900 °C, please see the similarities for TiN and (Ti,Al)N when comparing Figs. 5 and 8.

Important to mention here is, that a small fraction of hcp-AlN phase-formation may even lead to an increased hardness [154], but definitely to an increased straining [155] due to the massive change in specific volume (from fcc-AlN to hcp-AlN). The latter is also responsible for the increased density of dislocations [28] as well as stacking faults and nano-twins [210] in these areas and the formed hcp-AlN. The connected increase in specific volume (upon the phase transformation from fcc-AlN towards hcp-AlN) and nano-twinning may even lead to an increased fracture toughness, which will be discussed in Ch. 4.5. The associated massive straining is also one key to postpone the hcp-AlN phase formation, which will therefore be preferred at weaker regions. These could be special grain boundaries and grain boundary structures as well as a reduced lattice resistance, which typically drops with increasing temperature. And if this can be delayed, the noticeable formation of hcp-AlN-based phases will also be reduced.

Fig. 9 again schematically summarizes the major strengthening contributions during the course of the microstructural changes happening to fcc-(Ti,Al)N upon annealing. Especially the formation of the significantly weaker hcp-AlN causes the strength to decline. For better visibility, the individual curves are shifted with respect to each other, based on the following considerations: spinodal decomposition will start, but only until the chemical variation at the boundaries of the spinodal region is reached, see Fig. 4b. Thus, at 900 °C this would be approx. fcc-$Ti_{0.7}Al_{0.3}N$ and fcc-$Al_{0.98}Ti_{0.02}N$. This will be followed by nucleation and growth of phases with chemical compositions close to the binodal, which are approx. TiN and AlN at 900 °C, Fig. 4b. A major advantage of an initial spinodal decomposition step is that no preferred nucleation sites are needed (spinodal decomposition works without nucleation) and, thus, the decomposition will be most homogeneous throughout the microstructure of the material, see also Fig. 6. The curves of the Orowan, $\Delta\tau_O$, and Kelly–Fine, $\Delta\tau_{KF}$, mechanisms in Fig. 9 are calculated with the same parameters as used above (e.g. $f_p = 0.3$). But additionally, $\Delta\tau_O$ is also presented for much stronger particles (with α being doubled to 0.26), which causes the peak-strength to increase from 1.54 to 1.94 GPa. These strengthening mechanisms counteract the occurring softening mechanisms due to the reduction in dislocation density ($\Delta\tau_T$) and grain growth ($\Delta\tau_{HP}$). With the looming of the much weaker hcp-AlN, the overall strength decreases massively.

The course of $\Delta\tau_{hcp\text{-}AlN}$ in Fig. 9 is simply estimated by using the strength difference between these phases ($\Delta\tau_{AlN}$), the transformed volume fraction f_{AlN} of fcc-AlN into hcp-AlN, as well as the relevant fraction of AlN (x) in the alloy ($Ti_{1\text{-}x}Al_xN$) according to:

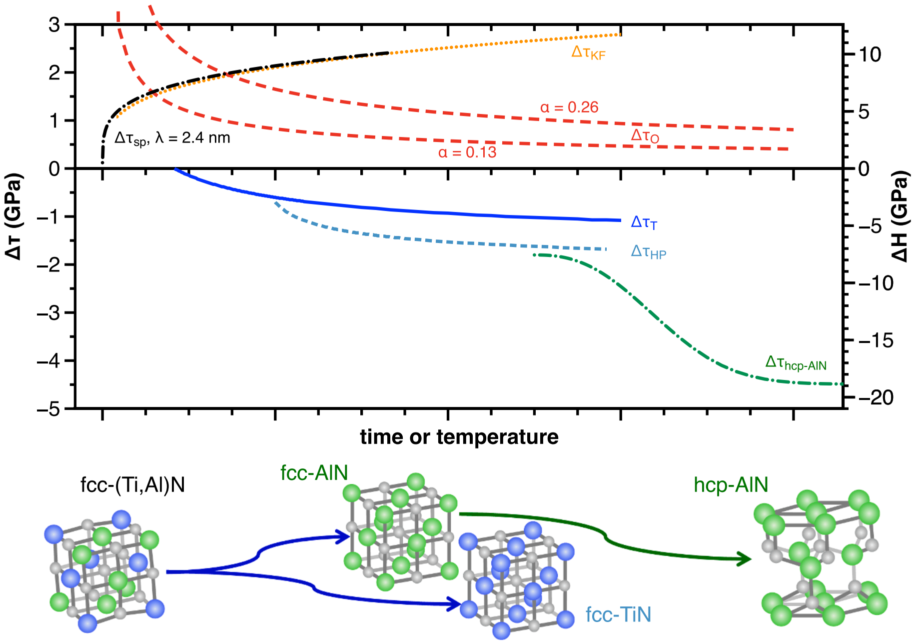

Fig. 9. Schematic representation of the decomposition of single-phase fcc-(Ti,Al)N towards the stable constituents fcc-TiN and hcp-AlN via an intermediate step of Al-rich and Ti-rich fcc-structured domains, based on [180]. The connected processes (spinodal decomposition, $\Delta\tau_{sp}$, Kelly–Fine, $\Delta\tau_{KF}$, Orowan, $\Delta\tau_O$, Taylor, $\Delta\tau_T$, Hall–Petch, $\Delta\tau_{HP}$, transformation of fcc-AlN to hcp-AlN, $\Delta\tau_{hcp\text{-}AlN}$) lead to a change in strength during annealing. $\Delta\tau_{KF}$ and $\Delta\tau_O$ were calculated for $f_p = 0.3$ (using the other parameters as above). Also shown is the impact of the strength of the particles, α, which can be between 0 for weak and 1 for strong particles, see Eq. (6). $\Delta\tau_T$ was shifted in x-axis as well as $\Delta\tau_{HP}$, which was also shifted by –0.7 GPa ($\Delta\tau_T \approx$ –0.7 GPa upon a reduction in dislocation density from $1\cdot10^{17}$ to $4\cdot10^{16}$ m^{-2}). $\Delta\tau_{hcp\text{-}AlN}$ was shifted in x-axis and by –1.8 GPa ($\Delta\tau_{HP}$ = –1.13 GPa for a grain-size increase from 20 to 120 nm). Like for Fig. 7, the range of the right ΔH-axis is 4.2-times that of the left Δτ-axis (with the 0-line at level).

$$\Delta\tau_{hcp-AlN} = -f_{AlN}\cdot x\cdot\Delta\tau_{AlN} \tag{17}$$

With Eq. (11), $\Delta\tau_{AlN}$ is estimated to ≈ 5.4 GPa from the hardness difference between fcc-AlN (40.5 GPa [211]) and hcp-AlN (17.9 GPa [211], 17.7 GPa [212]). The general form of the Johnson–Mehl–Avrami–Kolmogorov (JMAK) equation [199] is used to obtain f_{AlN}:

$$f_{AlN} = 1 - e^{-Bt^{n}} \tag{18}$$

with B a material constant (including the nucleation and growth rate at a given temperature) and n representing the transformation exponent. The latter is set to 5/2 for a continuous nucleation and B is set to $1\cdot10^{-5}$ min^{-n}, to have the transformation completed after ≈ 240 min. This leaves a maximum strength reduction of $\Delta\tau_{hcp\text{-}AlN} \approx 2.7$ GPa ($\Delta H \approx 11.3$ GPa) for $Ti_{0.50}Al_{0.50}N$.

As already indicated in Fig. 7b with the comparison of 900 and 1000 °C annealed $Ti_{0.42}Al_{0.58}N$ and $Ti_{0.41}Al_{0.56}Ta_{0.03}N$, alloying can postpone the hardness decline by postponing the hcp-AlN formation [193]. Therefore, a short overview on the impact of individual alloying elements will be given in the following chapter.

2.2. *Alloyed and microalloyed (Ti,Al)N*

In the last decades, a lot of research has been done to further improve $Ti_{1-x}Al_xN$ hard coatings. In combination with the architecture of the coatings, e.g. multilayer coatings consisting of $Ti_{1-x}Al_xN$ and other nitrides, the effect of certain alloying elements on friction, wear, oxidation resistance, and hardness has been investigated [213–220]. Alloying $Ti_{1-x}Al_xN$ with C essentially leads to a substitution of N and results in the formation of carbonitrides. In contrast, the addition of Si and B mainly leads to grain-refinement by the triggered formation of a grain-boundary phase [221–224], with an associated increase in hardness and, in the case of Si, also to improved oxidation resistance.

In contrast, the elements from groups III–VI mainly substitute Ti or Al at the metal-sublattice. Investigations of Cr-alloyed $Ti_{1-x}Al_xN$ hard coatings have shown the great potential for improving the oxidation resistance by Cr [225–227], but this can also be improved by Y [228,229]. It should be noted here that the mode of action of Cr is different from that of Y. Cr helps to form a dense, stable oxide layer, whereas Y helps to improve the adhesion of the oxide layer and also blocks the fast diffusion paths, i.e. the grain boundaries in the oxide layer. These are known as reactive element (RE) effect for structural and coating materials, especially those able to form protective chromia or alumina scales [230–235]. But small additions of REs, such as Y, Ce, and La to such materials may also enhance their mechanical properties, see Refs. [226,236,237]. Si also positively influences oxidation resistance as well as mechanical properties [237]. Addition of Mo or V can significantly improve friction and wear resistance [238–243]. Alloying $Ti_{1-x}Al_xN$ with group V and VI elements such as Zr, Hf, Nb, and Ta has shown significant improvements in mechanical properties and wear resistance [244–252], but also in oxidation resistance.

Even to present and discuss only the most promising alloying concepts would go beyond the scope of this review article. Therefore, we will recapitulate recent findings in this field that have been obtained by coating-developments using the same unbalanced magnetron sputtering system (a modified Leybold Heraeus Z400). No other microstructural modifications than obtained by using alloyed compound targets are made, thus, there was no substrate rotation, no alternating between individual sputter sources, no multilayers or even superlattices, no gradients, etc. This allows to extract the effect of the alloying elements themselves.

The system holds a 75-mm-circular magnetron – equipped with powder metallurgically (PM) prepared $Ti_{1-x}Al_x$ targets (mostly with an Al/Ti ratio of 1) and their alloyed variants (all from Plansee Composite Materials GmbH and typically with 99.7 % purity). The static

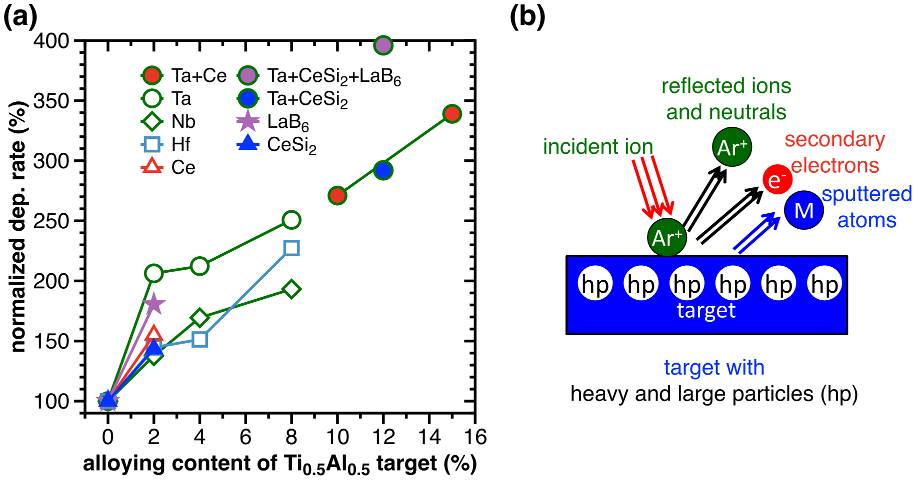

Fig. 10. (a) Normalized deposition rates (normalized to coatings sputtered from a $Ti_{0.5}Al_{0.5}$ target, allowing for ≈ 77 nm/min [255]) of alloyed and microalloyed $Ti_{1-x}Al_xN$ coatings when sputtering the corresponding $Ti_{0.5}Al_{0.5}$ PM targets [193,255–262]. (b) Schematic presentation of the heavy and large particle (hp) effect, based on the sputter yield amplification effect by heavy elements [254].

substrate holder is parallel to it at a distance of 4–6 cm. Typical deposition conditions were: base pressure $\leq 5\cdot10^{-4}$ Pa, total working gas pressure ≈ 0.35 Pa, bias potential –50 V, substrate temperature ≈ 430 °C, and mixed Ar/N_2 DC glow discharge (both gases with 99.999 % purity). For further details on the experimental and computational methods see the corresponding primary articles.

2.2.1. Sputter yield amplification effect on deposition rates

The alloyed PM prepared Ti-Al targets not only allow for a homogeneous distribution of the individual elements upon arrival at the substrates, they also allow for an increased sputter rate/deposition rate of the alloyed $Ti_{1-x}Al_xN$ coatings, see Fig. 10a. The selection of the alloying elements is/was based on the following considerations:

- group V (Zr, Hf) elements are isovalent to Ti and their larger size would basically lead to a di-elastic contribution in the solid solution,
- group VI (Nb, Ta) elements provide additional d-electrons promoting the $sp3d^2$-hybridisation and add par-elastic and di-elastic contributions to the solid solution,
- reactive elements (Y, Ce, and La) provide additional support for the formation of protective oxide scales, but only for small additions [253].
- Originally, Ce was added elementary to the Ti-Al targets to study its isolated effect. Better process-handling during the powder metallurgical manufacturing of the targets motivated the development of $CeSi_2$-doped $Ti_{1-x}Al_x$ targets. The usage of $CeSi_2$ allowed to extract the beneficial effects of Ce and Si. Based on the positive results for $CeSi_2$-doped $Ti_{1-x}Al_x$ targets and resulting coatings, La was added in the form of LaB_6 to the $Ti_{1-x}Al_x$ targets. Multiple processes are suggested in the individual papers to be relevant for the increased deposition rate, which is obtained by dividing the total coating thickness by the deposition time. Some target alloying

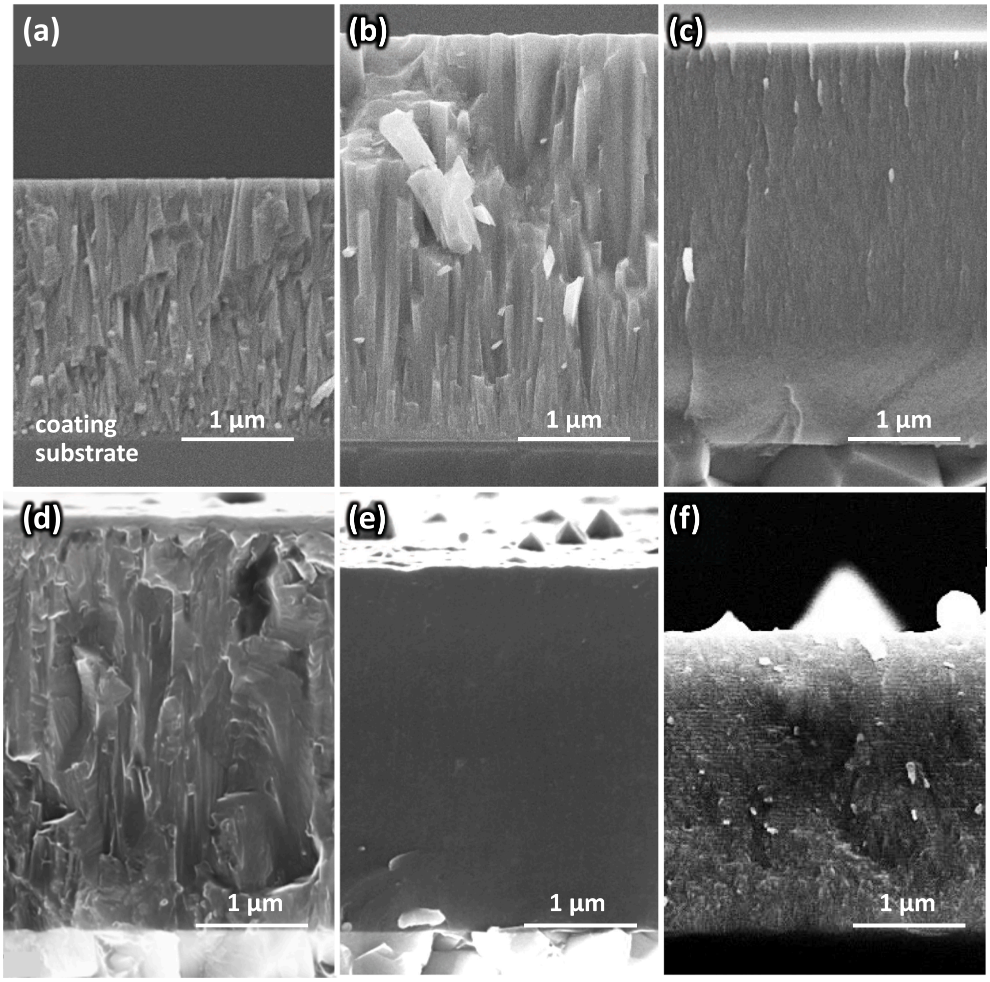

Fig. 11. Fracture cross-sectional SEM micrographs of as-deposited sputtered (a) $Ti_{0.49}Al_{0.51}N$ [257], (b) $Ti_{0.44}Al_{0.44}Ta_{0.12}N$ [258], and (c) LaB_6 doped $Ti_{0.43}Al_{0.57}N$ [255] coatings, and arc-evaporated (d) $Ti_{0.52}Al_{0.48}N$ [263], (e) $Ti_{0.34}Al_{0.54}Ta_{0.12}N$ [263], and (f) multilayered $Ti_{0.49}Al_{0.44}Ta_{0.07}N/Al_{0.62}Cr_{0.38}N$ [264] coatings.

elements/phases (like LaB_6) lead to an increased secondary electron emission. Additionally, the heavy and evenly distributed alloying elements (like Ce, Y, Zr, Nb, Hf, and Ta) and particles (like $CeSi_2$ and LaB_6) act as rigid regions within the target, Fig. 10b.

Consequently, the energy of impinging particles (like Ar and N_2 ions) is concentrated to a smaller region resulting in an increased collision cascade density during sputtering. A very similar process and outcome has earlier been reported for sputtering of heavy-element-doped Al targets [254]. A corresponding behavior during arc-evaporation of such cathodes could not observed, as there the collision cascade within the target is not that relevant.

2.2.2. Growth morphologies

While the alloying elements Ce, Y, Zr, Nb, Hf, and Ta, have only a minor influence on the columnar growth morphology of the fcc-$Ti_{0.50}Al_{0.50}N$-based coatings for the concentration range investigated (Ce and Y $\leq$ 2 at% and Zr, Nb, Hf, Ta $\leq$ 8 at%). Microalloying with $CeSi_2$ and LaB_6 led to a much finer growth morphology. Exemplarily, scanning electron microscopy (SEM) fracture cross-sections of as-deposited sputtered $Ti_{1-x}Al_xN$, $Ti_{1-x-y}Al_xTa_yN$, and LaB_6-doped $Ti_{1-x}Al_xN$ coatings are presented in Fig. 11a, b, and c, respectively. If the chemical composition is deep within a (metastable) single-phase field region, and thus no segregation events cause repeated nucleation and hamper coalescence during the early stages of nucleation, a coarse-grained structured with pronounced columnar growth will develop for sputtered coatings, Fig. 11a and b. This can be influenced by an increased ion bombardment during film growth, which promotes repeated nucleation [265]. However, this typically comes with a steep price of increased stresses and increased dislocation density, which recover as soon as the (application) temperature is above the deposition temperature.

Another possibility to reduce the grain size is the addition of elements during film growth that are prone to segregate to surfaces and interfaces, such as Si and B [266]. The grain size can be controlled by a careful selection of additional elements (or phases) [23]. Thus, growth morphology and column boundary fracture can massively be influenced through specific alloying elements (here shown for LaB_6-doped $Ti_{1-x}Al_xN$, Fig. 11c).

Although section 2.2 essentially is about the impact of alloying elements on deposition rate, growth morphology, preferred phase formation and their stability, as well as the strength of $Ti_{1-x}Al_xN$ films – for which magnetron sputtered films are used without modifying their growth morphonology by other techniques then alloying the sputter-target itself – additional important possibilities for obtaining a dense growth morphology are briefly mentioned.

These are for example, high power impulse magnetron sputtering (HiPIMS) and arc-evaporation as well as superlattices and multilayers, which typically lead to a much denser growth morphology, not necessarily a smaller grain size, but a more compact arrangement with less pronounced column boundaries. See for example the fracture cross-sections of arc-evaporated $Ti_{1-x}Al_xN$, $Ti_{1-x-y}Al_xTa_yN$, and the multilayered $Ti_{1-x-y}Al_xTa_yN/Cr_{1-x}Al_xN$, Fig. 11d, e, and f, respectively.

This comparison shows that the fracture-cross-sections of arc-evaporated coatings is not dominated by grain(column) boundary fracture as is typically the case for sputtered ones. This is especially valid for single-phased coatings, mild deposition conditions (e.g. low bias potential), and no segregating elements. In this context compare Fig. 11d and a, respectively. However, Fig. 11 shows that growth morphology and column boundary fracture of sputtered coatings can massively be influenced through specific alloying elements (like for LaB_6-doped $Ti_{1-x}Al_xN$, see Fig. 11c).

2.2.3. Maximum Al-content for fcc over hcp preference

The preferred crystal structure (fcc or hcp) of supersaturated $Ti_{1-x}Al_xN$ solid solutions can be determined by calculating the formation energy E_f of fcc-$Ti_{1-x}Al_xN$ and hcp-$Ti_{1-x}Al_xN$, such as shown in Fig. 3b. Their cross-over represents the critical Al-content x_c up to which fcc is preferred over hcp. For $Ti_{1-x}Al_xN$ with a "random" distribution of Al and Ti on the metal sublattice, this is at $x_c \approx 0.69$, see

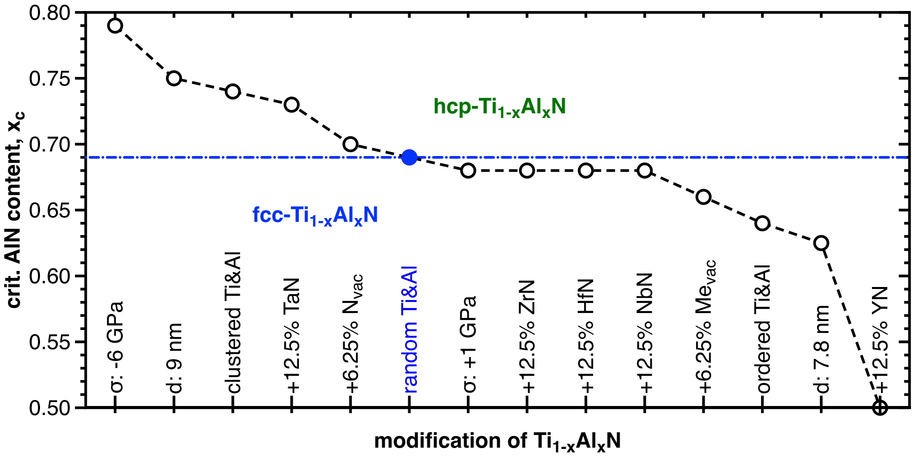

Fig. 12. Critical AlN contents, x_c, up to which the fcc-$Ti_{1-x}Al_xN$-based solid solutions are preferred and how this value can be tuned by various modifications. x_c: 0.79–0.68 (stresses σ: –6 and + 1 GPa) [185], 0.75–0.625 (grain size d: 9–7.8 nm) [267], 0.74–0.64 (configuration of Ti and Al atoms, Fig. 3c) [129], 0.73–0.5 (alloying with 12.5 % TMNs) [193,237,252,259–261,268], 0.7–0.66 (Me or N vacancies) [269].

Fig. 12. As already mentioned, “simply” redistributing Al and Ti at the metal sublattice changes x_c to 0.64 (ordered distribution of Al and Ti) and 0.75 (clustered distribution of Al and Ti), as indicated in Fig. 3b and 12.

A massive impact on x_c have stresses, where compressive ones increase x_c and tensile ones decrease it, Fig. 4c. While high compressive stresses such as –6 GPa are realistic in ceramic thin films, higher tensile stresses than +1 GPa usually cause the formation of cracks [270]. Therefore, these two values are chosen for Fig. 12 to highlight the pronounced increase in x_c to 0.79 (–6 GPa stresses) and a reduction to 0.68 (+1 GPa stresses) [185]. Additionally, surface energy contributions, such as present due to grain and column boundaries, have their impact on x_c, as shown in [267]. There, with a grain size increase from 7.8 to 9 nm the calculated x_c increases from 0.625 to 0.75. As reported in [267], the upper value seems to be the limit. But the formation of vacancies (commonly observed in PVD coatings) also cause a variation in x_c, which decreases to 0.66 for metal vacancies (Me_{vac}) and increases to 0.7 for nitrogen vacancies (N_{vac}), see Fig. 12.

Alloying $Ti_{1-x}Al_xN$ with the transition metals TM = Hf, Nb, and Zr – in order to form $Ti_{1-x-y}Al_xTM_yN$ solid solutions – only mildly reduces x_c from 0.69 to 0.68 for y up to 0.125 [193,237,252,259–261,268]. With the addition of up to 12.5 at% Y (to the metal sublattice) x_c drastically decreases to 0.5 [237]. For Refs. [237,268] 32-atom-containing supercells were used (thus $y = 2/16 = 0.125$), whereas this was increased to 36 for better randomization of fcc-$Ti_{1-x-y}Al_xTM_yN$ using the special quasi-random structure (SQS) approach for Refs. [259,260] (there, $y = 2/18 \approx 11.1$). The comparison yields no noticeable difference in x_c and because the hcp-$Ti_{1-x-y}Al_xTM_yN$ was always calculated with a 32-atom-containing supercell, the maximum y is simply stated here with 0.125. With the addition of up to 12.5 at% Ta (to the metal sublattice; 11.1 at% for fcc-$Ti_{1-x-y}Al_xTM_yN$) x_c noticeably increases to 0.73 [193,261].

Yttrium favors sp^3 hybridization and, thus, tends to favor the hcp crystal structure. This explains the massively decreased x_c value when adding Y, in agreement with experimental studies [237,259]. In contrast, Ta promotes the interaction of the metal-d states with the N-p states favoring sp^3d^2 hybridization [259] and thus x_c increases. But the induced changes in electronic structure and thereby on the cohesive energy E_{coh} have also implications on the mechanical strength, as presented with the increase in indentation hardness ΔH of sputtered single-phase fcc-$Ti_{1-x}Al_xN$ coatings in Fig. 13, due to alloying. Especially for Nb, Ta, and Hf alloyed fcc-$Ti_{1-x}Al_xN$ the hardness increase follows a $\sqrt{c}$ dependence, according to Eq. (1) with Fleischer. This is because the growth morphology of the $Ti_{0.50}Al_{0.50}N$-based materials is little influenced by the addition of up to 10 at% (metal-fraction, c) or even 12 at% as shown in Fig. 11a and b. However, as mentioned in [271–273], alloying with Ta, which easily forms other nitrides than those with N/Me ≈ 1 and promotes the formation of vacancies in fcc-TaN compounds, special attention needs to be paid to the obtained N/Me ratio. The hardness increase due to Zr-alloying nicely follows the trend provided by Hf-alloying – in agreement with their similarity in size and in influencing the electronic structure of fcc-(Ti,Al)N [259,260]. The Sc-alloyed epitaxially grown 001-(Ti,Al,Sc)N shows the highest ΔH of ≈16 GPa for these basically solid solution strengthened coatings [274].

The impact of Y, La, and Ce (being three-valent) is significantly less pronounced and might even result in a hardness reduction, as

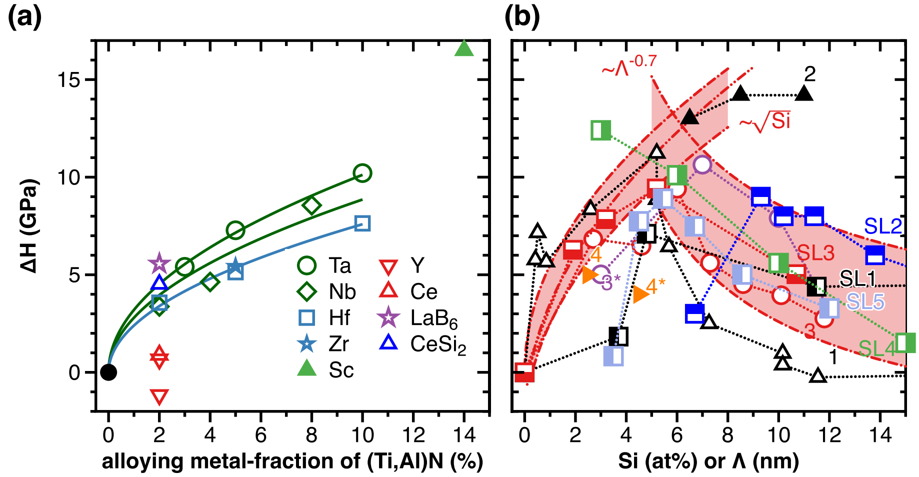

Fig. 13. Strengthening of various TMNs due to solid solution (a), grain-refinement and superlattice effect (b). (a) Change in hardness ΔH of sputtered single-phase fcc-(Ti,Al)N hard coatings, with an Al/Ti ratio = 1 of their respective targets, due to alloying with Nb and Ta (5 VE), Zr and Hf (4 VE and isovalent to Ti), Ce and Y (3 VE), $CeSi_2$ and LaB_6 (% refers to at% or mol%). The solid lines are fits (according to Eq. (1), with n = ½, thus according to Fleischer) to the data points of Ta, Nb, and Hf alloyed coatings. The Sc-alloyed one ($Ti_{0.5}Al_{0.36}Sc_{0.14}N$) is epitaxially grown on MgO [274], for which the epitaxial $Ti_{0.50}Al_{0.50}N$ with H = 29.5 GPa was used as reference [52]. In average, a single-phase fcc-$Ti_{0.50}Al_{0.50}N$ shows 30–35 GPa. (b) ΔH by Si-alloying of TiN (#1 [39], #2 [275]) or (Ti,Al)N (#3 [276], #3* (unpublished own data), #4 [217], #4* [277]) – #1 & 3 are sputtered coatings and #2 and 4 are arc-evaporated coatings. If the Si content was normalized with the metals (to have Ti+(Al) + Si = 100 %), it was divided by 2 for the comparative plot. Also given in (b) is ΔH by superlattice (SL) structures (half-filled squares): SL1: TiN/SiN_z [278], SL2: (Ti,Al)N/(Cr,Al)N [279], SL3: (Ti,Al)N/Si_3N_4 [280]), SL4: TiN/(Al,Sc)N [274], SL5: CrN/AlN (2-nm-thin AlN) [281]. For more details on superlattices see Ch. 4.2. The dash dotted red lines with a shaded region are fits proportional with $\sqrt{x}$ and $x^{-0.7}$ (x for Si or Λ). The red dash-double-dot line (which extends slightly beyond the shaded region) is a fit according to Eq. (4) with k ≈ 8.5 GPa·nm$^{0.5}$ as used above for the (Ti,Al)N example, with d ≈ 35 nm/Si at%, and converting Δτ in ΔH with Eq. (9). (For interpretation of the references to colour in this figure legend, the reader is referred to the web version of this article.)

presented for Y, Fig. 13a. These elements favor sp^3 hybridization and thus weaken the cohesive energy of fcc-$Ti_{1\text{-x-y}}Al_xN$ solid solutions [155], in agreement with the reduced x_c, see Fig. 12.

However, when using LaB_6 or $CeSi_2$ alloyed $Ti_{1\text{-x}}Al_x$ targets, the additionally provided B or Si favor the formation of a more compact and uniform growth morphology with a typically increased cohesive strength of the grain and column boundaries due to Si [282,283] and B [266]. In combination, this allows for a pronounced hardness increase of the resulting single-phase fcc-(Ti,Al)N coatings even if Ce and La is present. The latter are especially beneficial for increased oxidation resistance, which will be discussed in detail in Ch. 3, due to the promoted RE-effect. If only Si is added to fcc-(Ti,Al)N, frequently a similar trend as presented in Fig. 13b (#3) is obtained, where the hardness peaks for a certain Si content (often in the range of only a few at%). The overall behavior follows what has been studied in detail for Si-alloyed TiN (#1 in Fig. 13b) [38–40].

The initial increase in H with increasing Si is due to the concomitant reduction in grain size, d. As the dependence of d on Si up to the hardness-peak can be described by $\sim 1/\mathrm{Si}$ [221], the increase in H with $\sqrt{Si}$ (Fig. 13b) essentially corresponds to the Hall–Petch relation with $\frac{1}{\sqrt{d}}$. The red dash-double-dot line, extending slightly beyond the shaded region in Fig. 13b, is a fit according to the Hall–Petch relation, Eq. (4), with $k \approx 8.5\ \mathrm{GPa{\cdot}nm^{0.5}}$, as used above for (Ti,Al)N, and estimating d (in nm) through the Si content (in at%) according to $d \approx 35/\mathrm{Si}$. Thus, the hardness increases with the Si content as long as the grain size decreases and the Si-N grain boundary phase that forms is thin and has a high cohesive strength [39,221], as schematically presented in Fig. 14.

Typically, the grain size for such TiN/SiN_z nanocomposites is about 5–10 nm at the hardness-peak, but not necessarily equiaxed as shown by Kauffmann et al. [284]. They actually pointed towards two independent mechanisms for the hardness-increase of TiN/SiN_z coatings involving the size-dependent yield strength as well as the aspect ratio of the TiN grains. The smaller the grains but the larger their aspect ratio, the harder the composite. Large TiN grains with large aspect ratio would yield prior to SiN_z, this is where grain-refinement strengthening dominates. A decreasing aspect ratio of the TiN grains reduces their relative load at the expense of increased load on SiN_z. Since both the size and aspect ratio of the TiN grains decrease with increasing Si content, as illustrated in Fig. 14, a balance of these two leads to the hardness-peak. This is because the smaller TiN grains are stronger, but their decreasing aspect ratio also distributes the load more and more towards SiN_z, which is weaker. The maximum Si content up to which the hardness increases depends on the deposition conditions and whether there is also Si soluted in the encapsulated nitride grains. The latter is the case for the arc-evaporated Si-alloyed TiN (#2 in Fig. 13b).

Thus, such coatings would experience grain-refinement plus solid solution strengthening. Therefore, this coating shows a higher ΔH and maximum Si content up to which ΔH increases. The hardness-decline with increasing the Si content beyond the value (often 2–5 at% Si [40,284], not normalized to the metals) where the hardness peaks is essentially due to the increasing thickness of the weaker SiN_z grain boundary phase, with only a slightly further reduction in grain size, as indicated in Fig. 14. The increasing spacing between the TiN crystals with further increasing Si content has its similarities with the bilayer period Λ of superlattices. Therefore, this decline can be described with $\Lambda^{-0.7}$ respectively $\mathrm{Si}^{-0.7}$, see Fig. 13b and the next paragraph. For (Ti,Al)N not just the formation of a thick grain boundary SiN_z phase leads to a decline in hardness, but also the promoted hcp-phase formation beyond a critical Si content [287]. There are indications that the maximum hardness values, achievable through such modifications, are in the order of that obtained for diamond [288,289].

The formation of superlattice (SL) coatings, details on superlattices are given in Ch. 4.2, leads to a comparable hardness peak, but with respect to the superlattice modulation period Λ (often a bilayer period as here). Coming from the large Λ region, ΔH increases with decreasing Λ, according to the Chu and Barnett model for an increased shear stress due to the superlattice effect, $\Delta\tau_{SL}$, according to [290]:

$$\Delta\tau_{SL} \cong 1/\Lambda^p \tag{19}$$

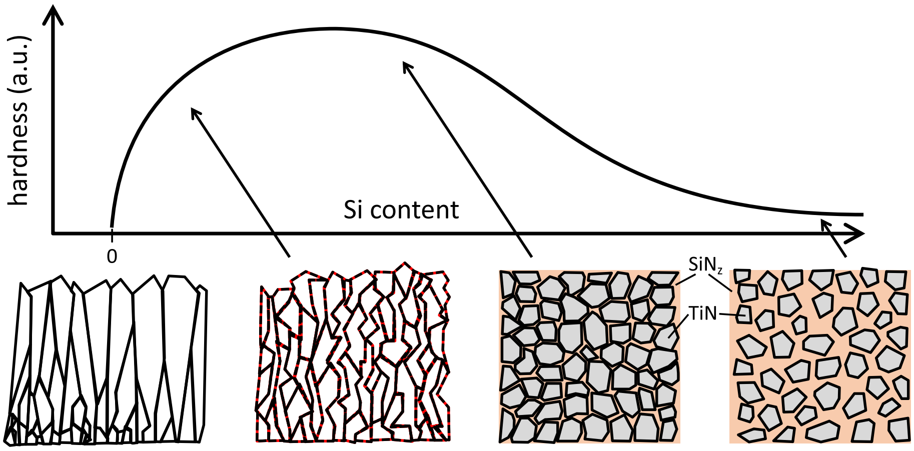

Fig. 14. Schematic presentation of the morphological evolution of TMNs when adding elements that promote segregation to grain boundaries – which impedes coalescence during nucleation leading to smaller grains (here on the example of $TiN–SiN_z$) – and how this correlates with the hardness evolution, adapted from [38,40,284–286].

with exponent p being between 0.74 and 0.67. The underlying mechanism considers that the coherently grown layers have the same slip systems (but different shear moduli and/or lattice spacings) being oriented with each other also in polycrystalline cases [290]. This is different to the underlying mechanism for the similar Hall–Petch relation (where $p = 0.5$, Eq. (4)), where stresses due to dislocation pile-ups at the grain boundary move dislocations and activate their sources in the neighboring grains, which are differently oriented. However, Hall–Petch, Orowan (Eq. (6)), and other mechanisms might be active in superlattices and contribute to the hardness gain, as summarized in Ch. 4.2. The decline in ΔH for Λ below the peak hardness value is caused by several processes due to dislocation gliding across the interfaces. For example, the thickness of the interface itself, which is not atomically sharp (especially for miscible layers), and the opposing forces that can act on dislocations at interfaces when they are close together. Thus, lower stresses are needed to move dislocations [291]. This is a bit similar to the Kelly–Fine mechanism, where dislocations glide and cut through particles [88]. Therefore, the ΔH-vs-Λ behavior can be fitted with a $\sqrt{\Lambda}$ dependence, thus replacing r_p with Λ in Eq. (5) for the small Λ region. Together, these effects result in the observed hardness peak, which is nicely presented in Fig. 13b by the SLs #1–4 (SL1 TiN/SiN$_z$ [278], SL2 (Ti,Al)N/(Cr,Al)N [279], SL3 (Ti,Al)N/Si$_3$N$_4$ [280]), SL4 TiN/(Al,Sc)N [274]), and SL5 CrN/AlN [281]. The latter shows an abrupt decline with decreasing Λ for values below the peak hardness (at $\Lambda \approx 5.5$ nm). This is because these superlattices always had the same layer thickness of AlN ($\approx$ 2 nm) and if the CrN layer becomes thinner than AlN, it is not stabilized anymore in its polymorphic fcc structure. Similarly, SL1 (TiN/SiN$_z$) always contained a 1.7 nm thin SiN$_z$ layer, except for the coating with the highest ΔH (at $\Lambda \approx 4.8$ nm). There, the SiN$_z$ layer was only 0.7 nm thin.

2.2.4. *Thermal stability of the phases and corresponding hardness evolution*

Before dealing with the mixing enthalpies ΔH_{mix} of some quaternary Ti$_{1\text{-}x}$Al$_x$N-based solid solutions – where Ta and Nb (5 VE), Zr and Hf (4 VE and isovalent to Ti), and Y alloyed ones are used as model systems – we will discuss the stability (based on the mixing enthalpies ΔH_{mix}) of their ternary components. For example, a quaternary fcc-Ti$_{1\text{-}x\text{-}y}$Al$_x$TM$_y$N could decompose into the three fcc-ternaries: Ti$_{1\text{-}x}$Al$_x$N, TM$_{1\text{-}x}$Al$_x$N, and Ti$_{1\text{-}y'}$TM$_{y'}$N. The mixing enthalpies ΔH_{mix} of the AlN-based ternary fcc-TM$_{1\text{-}x}$Al$_x$N (Fig. 15a) and the TiN-based ternary fcc-Ti$_{1\text{-}y}$TM$_y$N (Fig. 15b) solid solutions are calculated after:

$$\Delta H_{mix} = E_{f,ternary} - E_{f,binary} \tag{20}$$

with $E_{\mathrm{f,ternary}}$ and $E_{\mathrm{f,binary}}$ being the DFT-obtained energy of formations for the respective fcc ternary and fcc binary nitrides.

The Al-containing ternary fcc-TM$_{1\text{-}x}$Al$_x$N solid solutions generally provide positive ΔH_{mix} values (Fig. 15a). Only Nb- and Ta-based ternary solid solutions show slightly negative ΔH_{mix} values for small Al contents. Thus, there is even a stabilization of the fcc structure by a small addition of Al. This is remarkable since the stable structure of AlN is hcp. But not only in terms of decomposition into fcc-based binaries, the data suggest that Nb- and Ta-based ternary fcc solid solutions with low Al content might also be stable in terms of decomposition into fcc-TMN and hcp-AlN. This was validated by additional DFT and experiments for Nb-Al-N and Ta-AlN [292]. Fig. 15a shows this when using the dash-dotted line, which is the AlN-mole-fraction-based gain in energy for the transformation of fcc-AlN to hcp-AlN, as the base-line. On the Al-rich side, ΔH_{mix} shows a strong gradient.

The ΔH_{mix} values of the Ti-containing ternary fcc-Ti$_{1\text{-}y'}$TM$_{y'}$N solid solutions are strongly positive for Y and Zr, nearly zero for Hf and again slightly negative for Nb and Ta (Fig. 15b). Again, the already very stable fcc structure of TiN is further stabilized by the addition of Nb and Ta. These calculations indicate that, for the alloys considered here, the formation of ternary products during decomposition of quaternary fcc-Ti$_{1\text{-}x}$Al$_x$N-based solid solutions are only likely if alloyed with Nb, Ta, or Hf. There, fcc-structured ternary Ti$_{1\text{-}y'}$Nb$_{y'}$N, Ti$_{1\text{-}y'}$Ta$_{y'}$N, and Ti$_{1\text{-}y'}$Hf$_{y'}$N could form almost over the entire composition range (Fig. 15b); especially if considering that with increasing temperature (which would be necessary for such decomposition) the stabilizing effect of entropy

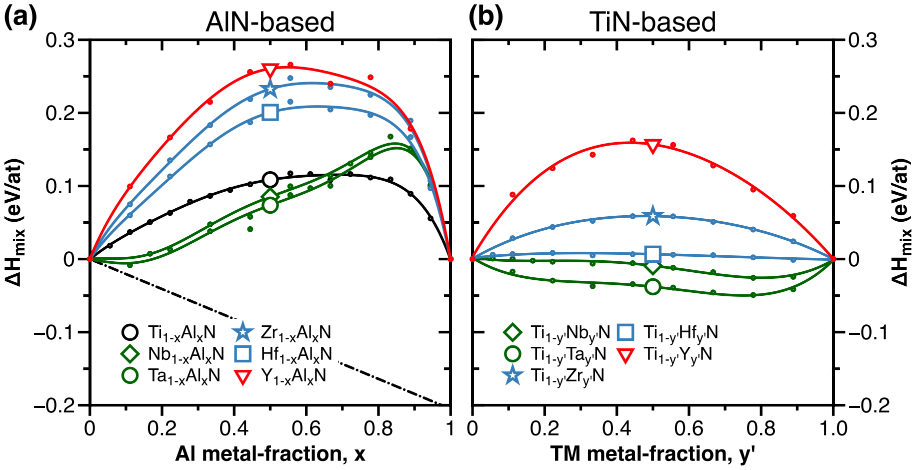

Fig. 15. Mixing enthalpies ΔH_{mix} of (a) fcc-TM$_{1\text{-}x}$Al$_x$N (the lines are 6th order polynomial fits) and (b) fcc-Ti$_{1\text{-}y'}$TM$_{y'}$N (the lines are 4th order polynomial fits) with respect to their binary fcc-nitrides. The dash-dotted line in (a) gives the base-line for the decomposition into fcc-TMN and hcp-AlN. Details are reported in Refs. [153,237,259,260,293].

steadily increases. It should be remembered, any system tries to minimize enthalpy, but to maximize entropy.

Ternary fcc-structured $Nb_{1-x}Al_xN$ and $Ta_{1-x}Al_xN$ would prefer a low Al-content, in the range of $x \approx 0.1$, see Fig. 15a. The Al-rich part is essentially always the binary AlN. This needs to be considered when discussing the stability of quaternaries based on ΔH_{mix}, as it requires the knowledge of the entire landscape. For this, machine learning (ML) would be an ideal tool, where DFT would provide some pillars. For example, the quaternaries fcc-$Ti_{1-x-y}Al_xTM_yN$ with 11.1 at% (metal-fraction) Nb, Ta, and even Hf, nearly show ΔH_{mix} of ≈ 0 eV/at, if considering a constitution of fcc-$Ti_{0.89}TM_{0.11}N$ and fcc-$Al_{0.89}TM_{0.11}N$, see Fig. 16a. Especially when considering the retarding components connected with any decomposition (such as formation of new interfaces and build-up of strains due to different specific volumes of the formed domains [124,195]) these quaternaries would hardly decompose into these ternaries. For fcc-(Ti,Al)N, the strain energy associated with the formation of fcc-AlN and fcc-TiN domains can be as high as 0.273 kJ/cm^3 (equivalent to 0.273 GPa or 0.0155 eV/at; for $x \approx 0.5$) and the interface energy amounts to another 0.275 kJ/cm^3 for spherical domains with 2 nm radius [124]. According to Fig. 15a and b, fcc-$Ta_{0.11}Al_{0.89}N$ would decompose into fcc-AlN and fcc-$Ta_{0.9}Al_{0.1}N$, while fcc-$Ti_{0.89}Ta_{0.11}N$ could be stable, respectively. This is similar for the Nb-alloyed alternative.

Thus, for example, fcc-$Ti_{0.39}Al_{0.5}Ta_{0.11}N$ would tend to decompose towards fcc-$Ta_{0.89}Al_{0.11}N$, fcc-$Ti_{1-y'}Ta_{y'}N$, and fcc-AlN (later hcp-AlN). Based on the elemental balance $y'_{max} = 0.22$ in fcc-$Ti_{1-y'}Ta_{y'}N$, for which the phase fraction of fcc-$Ta_{0.89}Al_{0.11}N$ becomes 0. A decomposition of fcc-$Ti_{0.39}Al_{0.5}Ta_{0.11}N$ into: $0.49 \cdot AlN + 0.07 \cdot Ta_{0.89}Al_{0.11}N + 0.44 \cdot Ti_{0.89}Ta_{0.11}N$ (all fcc-structured), is connected with an energy release of 0.095 eV/at. The energy is further decreased by 0.006 eV/at if no fcc-$Ta_{0.89}Al_{0.11}N$ forms, but therefore fcc-$Ti_{1-y'}Ta_{y'}N$ holds the maximum Ta of $y' = 0.22$. A decomposition into the binaries fcc-AlN, fcc-TaN, and fcc-TiN, would only decrease the energy by 0.087 eV/at. This is similar to fcc-$Ti_{1-x-y}Al_yNb_yN$, which show a slightly higher energy release, but still behaves very similar as non-alloyed fcc-$Ti_{1-x}Al_xN$ (being 0.108 eV/at for $x = 0.5$), see Fig. 16b. A decomposition of fcc-$Ti_{0.39}Al_{0.5}Nb_{0.11}N$ into $0.5 \cdot AlN + 0.5 \cdot Ti_{0.78}Nb_{0.22}N$ causes an energy-release of 0.110 eV/at and 0.109 eV/at into the respective binary fcc-nitrides. From the energy-of-formation point-of-view, an fcc-structured Al-containing ternary is unlikely to be formed during decomposition. Formation of the stable hcp-AlN modification further reduces the chances of remaining Al-containing ternary constituents. However, ternary fcc-$Ti_{1-y'}TM_{y'}N$ are likely formed (especially for Nb and Ta alloyed ones, Fig. 15b), which is in agreement with experiments conducted on (Ti, Al,Ta)N [261].

The Hf-containing fcc-$Ti_{1-x-y}Al_xTM_yN$ solid solution would hardly form Al-containing ternaries (already based on Fig. 15a), but fcc-$Ti_{1-y'}Hf_{y'}N$ solid solutions (with $y' = y/(1-x)$ if otherwise only AlN is formed) would be feasible according to Fig. 15b. However, the decomposition of fcc-$Ti_{0.39}Al_{0.5}Hf_{0.11}N$ into the binaries releases 0.123 eV/at; about 0.004 eV/at more than a decomposition into $0.5 \cdot AlN + 0.5 \cdot Ti_{0.78}Hf_{0.22}N$. But, decomposition-connected costs, like formation of new interfaces and build-up of strains as TiN and HfN have hugely different lattice parameters, and entropy-stabilization, $\Delta S_{mix} \approx 0.001$ kJ/Kcm^3 for $Ti_{0.50}Al_{0.50}N$; thus at 900 °C $T \cdot \Delta S_{mix}$ is ≈ 1.227 kJ/cm^3 or 0.07 eV/at, make these solid solutions quite possible, as observed experimentally during decomposition of (Ti,Al,Hf)N [260]. This is also to be expected for Zr, although ΔH_{mix} for fcc-$Ti_{1-y'}Zr_{y'}N$ is positive; however, during decomposition of fcc-$Ti_{0.39}Al_{0.5}Zr_{0.11}N$ the difference is only 0.022 eV/at between forming fcc-binaries or a remaining fcc-$Ti_{0.78}Zr_{0.22}N$. The Y-containing fcc-$Ti_{1-x-y}Al_xTM_yN$ solid solutions are different with their strong tendency to decompose into the constituting binary nitrides (YN, AlN, and TiN), see Fig. 15a and b; in agreement with experiments [228].

These considerations highlight that the formation of fcc AlN domains via spinodal decomposition is also expected for such alloys, like for fcc-$Ti_{1-x}Al_xN$. Especially for the Nb and Ta alloyed fcc-$Ti_{1-x}Al_xN$ solid solutions there is nearly no difference in ΔH_{mix} between the 5.5 or 11.1 at% alloys, and both provide a similar value as fcc-$Ti_{1-x}Al_xN$ up to $x \approx 0.7$, see Fig. 16b. Therefore, spinodal decomposition is observed in these alloys as well and sometimes even earlier (in terms of temperature and time), especially for those with large ΔH_{mix}. But at the same time, the decomposition process itself, if started, is retarded (in terms of temperature and time).

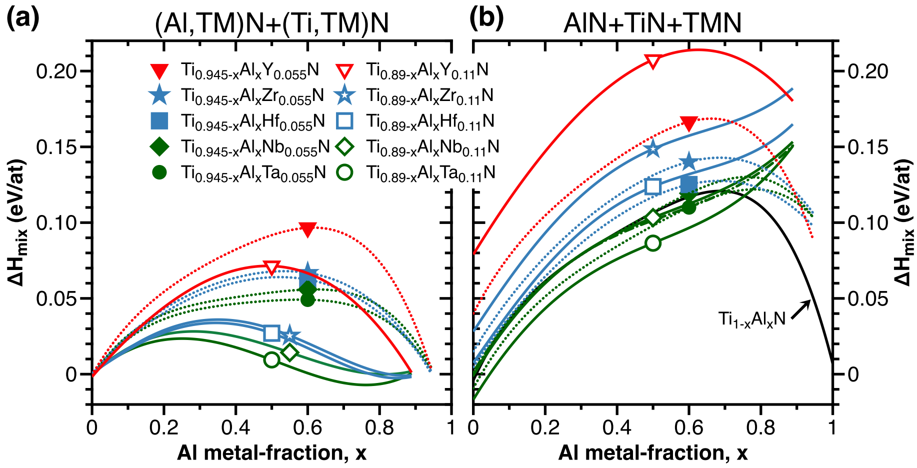

Fig. 16. Mixing enthalpies ΔH_{mix} of fcc-solid-solutions $Ti_{1-x-y}Al_xTM_yN$ with $y = 0.055$ and 0.111 as a function of Al content, x: **(a)** based on a constitution of fcc-$Al_xTM_{1-x}N$ (Fig. 15a) and fcc-$Ti_{1-y'}TM_{y'}N$ (Fig. 15b); **(b)** based on a constitution of fcc-AlN, fcc-TiN, and fcc-TMN. The lines are 4th order polynomial fits to the DFT data.

Several factors contribute to this, like higher lattice resistance at higher temperatures [52], increased retardation by the larger lattice-mismatch of evolving domains [124,195] and impeded diffusion. Therefore, typically the XRD peaks of alloyed (Ti,Al)N are broad (with marks of left- and/or right-hand shoulders) even after annealing at ≈ 1100 °C, while those of (Ti,Al)N passed this stage already and shift closer to the fcc-TiN positions, see Fig. 17a and b. Consequently, also the formation of the thermodynamically stable modification of AlN (hcp-AlN) is retarded. The process of spinodal decomposition and the retarding effect by alloying can be well observed by isothermal annealing treatments for different times, see, for example, the XRD patterns taken after 1, 120, and 480 min at 900 °C of $Ti_{0.41}Al_{0.59}N$ and $Ti_{0.42}Al_{0.48}Ta_{0.10}N$, Fig. 17c.

Alloying (Ti,Al)N with Si is special in the sense that a pronounced formation of Al-rich and/or Ti-rich fcc-structured domains upon annealing is hardly observed by XRD, see Fig. 17b. Furthermore, the addition of Si needs to be little (typically below 10 at%) and balanced with the Al content to avoid the formation of the hcp-phase already during deposition [287]. Contrary to these (Ti,Al)N-based materials, ΔH_{mix} of fcc-$Cr_{1-x}Al_xN$ (if considering magnetic moments, as needed) is ≈ 0.035 eV/at maximum [144,145]. The strain energy associated upon decomposition into fcc-AlN and fcc-CrN domains can amount to 0.055 kJ/cm^3 (equivalent to 0.003 eV/at; for $x \approx 0.5$; unpublished data). The remaining ≈ 0.032 eV/at is too little to compensate for the entropic loss and build-up of interfaces, this is why no spinodal decomposition is observed in this material system.

Upon annealing, typically direct formation of the thermodynamically stable hcp-AlN is present in (Cr,Al)N [294], because thereby the energy can massively be lowered (see the dash-dotted line in Fig. 15a, following $-0.205\cdot x$). Important to mention here also is that the formation of hcp-AlN with its much larger specific volume (about + 26 % compared to fcc-AlN without external constrains, Figs. 2 and 9) causes a strain energy of ≈ 6.705 kJ/cm^3 (equivalent to 6.705 GPa and 0.706 eV/at; for $x = 1.0$; unpublished data). The build-up of strain energy follows a 3rd-order polynomial fit with $0.239\cdot x + 0.297\cdot x^2 + 0.171\cdot x^3$ for $Ti_{1-x}Al_xN$. Thus, for $x \approx 0.5$ the thereby connected strain energy amounts to ≈ 0.216 eV/at, while the fcc–hcp transformation of AlN only releases ≈ 0.103 eV/at.

Consequently, the lattice resistance of the "matrix" plays a major role in allowing for the hcp-AlN formation. This, in addition to diffusion, explains why such a formation is typically observed at temperatures above ≈ 800 °C only, where the material is already much softer. If at the same time the matrix further weakens due to e.g. N_2-release (as observed for Cr–Al–N [294]) the hcp-AlN formation is accelerated. Contrary, improving the lattice resistance and avoiding N_2-release can postpone or at least retard the hcp-AlN formation, as observed for some of the alloyed (Ti,Al)N materials (e.g., Ta, Zr, and Si, see Fig. 17). As will be discussed in Ch. 4, the formation of hcp-AlN can be very beneficial for the fracture toughness due to the thereby connected massive compressive stresses. Thus, similar to transformation-induced toughening mechanisms, the propagation of cracks can be retarded (further discussed in Ch. 4).

Fig. 18a shows the simulated microstructural evolution during the spinodal decomposition process of a fcc-$Ti_{0.33}Al_{0.67}N$ alloy, during annealing at 850 and 900 °C [190], with the indicated change in Al content. A schematic phase evolution (based on experimental studies and DFT calculations) with increasing temperature is shown in Fig. 18b for the ternary fcc-$Ti_{0.50}Al_{0.50}N$ phase and in Fig. 18c for the quaternary fcc-$Ti_{0.4}Al_{0.5}TM_{0.1}N$ phases with TM = Zr, Nb, Hf, and Ta. The Y-containing fcc-$Ti_{1-x-y}Al_xY_yN$ solid solutions, which provide a much larger ΔH_{mix}, decompose faster, and as mentioned, towards AlN, fcc-TiN, and fcc-YN [228]. The schematic phase evolution is given in Fig. 18d.

A comprehensive DFT study over 126 equimolar Al-containing high-entropy sublattice nitrides [296] showed, that entropy-stabilization (≈ 0.06 eV/at at 800 °C) is always smaller than the 0.10–0.27 eV/at enthalpy-governed driving force for decomposition into stable binaries, ternaries, or quaternaries. But for 22 compounds the latter could be overruled with the additional strain-

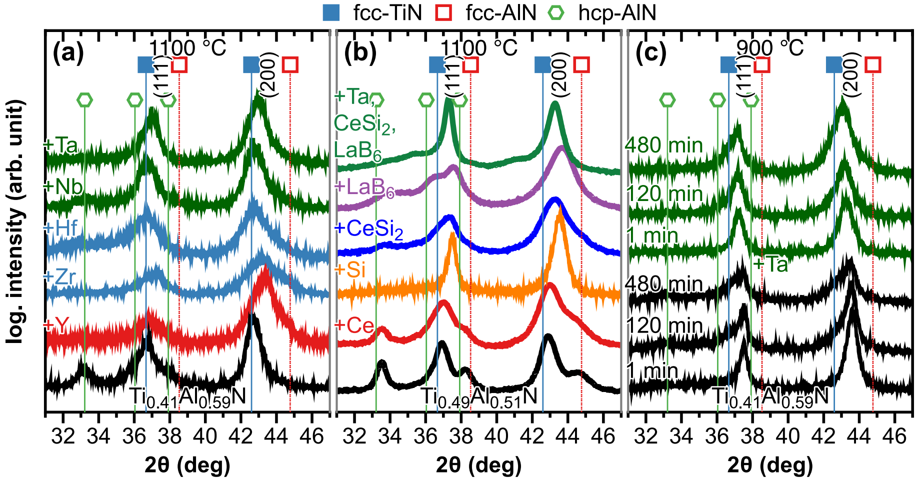

Fig. 17. XRD patterns of (Ti,Al)N and its alloys (which all were single-phase fcc in the as-deposited state) with (a) Y ($Ti_{0.51}Al_{0.47}Y_{0.02}N$ [228,229]), Zr ($Ti_{0.40}Al_{0.55}Zr_{0.05}N$ [252]), Hf ($Ti_{0.35}Al_{0.55}Hf_{0.10}N$ [260]), Nb ($Ti_{0.35}Al_{0.57}Nb_{0.08}N$ [268]), and Ta ($Ti_{0.42}Al_{0.48}Ta_{0.10}N$ [193]) after vacuum-annealing at 1100 °C for 1 min, and (b) Ce ($Ti_{0.48}Al_{0.50}Ce_{0.02}N$ [257,258]), Si (7 at% Si, unpublished), $CeSi_2$ ($Ti_{0.50}Al_{0.50}N(CeSi_2)_{0.02}$ [257]), LaB_6 ($Ti_{0.43}Al_{0.57}N(LaB_6)_{0.02}$ [255]), and Ta + $CeSi_2$ + LaB_6 ($Ti_{0.43}Al_{0.43}Ta_{0.14}N(CeSi_2)_{0.01}(LaB_6)_{0.01}$ [262]) after vacuum-annealing at 1100 °C for 10 min. (c) XRD patterns of $Ti_{0.41}Al_{0.59}N$ and $Ti_{0.42}Al_{0.48}Ta_{0.10}N$ film powder after vacuum-annealing at 900 °C for 1, 120, and 480 min.

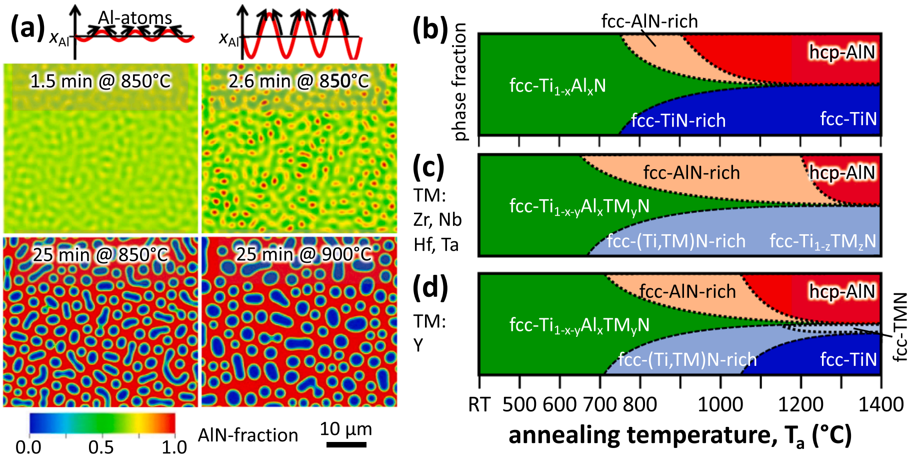

Fig. 18. (a) Phase-field simulated microstructure evolution of $Ti_{0.33}Al_{0.67}N$, with red representing AlN and blue TiN seen in the [001] direction, when annealed for 1.5, 2.6, and 25 min at 850 °C, and 25 min at 900 °C, adapted from [190]. (b) Schematic representation of the phase evolution of fcc-$Ti_{0.50}Al_{0.50}N$ as a function of temperature T_a. The fcc-AlN regions formed by spinodal decomposition [155,295] transform into the stable hcp modification (hcp-AlN) as the temperature continues to increase. (c) Schematic phase evolution of the quaternary fcc-$Ti_{0.4}Al_{0.5}TM_{0.1}N$ solid solutions for TM = Zr, Nb, Hf, and Ta. (d) Schematic phase evolution of the quaternary Y-containing fcc-$Ti_{0.4}Al_{0.5}Y_{0.1}N$ solid solutions. (For interpretation of the references to colour in this figure legend, the reader is referred to the web version of this article.)

stabilization (up to 0.28 eV/at; with an average decrease in driving force by 0.12 eV/at). This estimation does not consider any reduction in strain energy due to the formation of dislocations or other defects (like deformation twins), which will especially be promoted at higher temperatures needed for the decomposition. This is a major reason why the predicted strain-stabilized high-entropy sublattice nitride (Ti,Al,Hf,V,Zr)N stills shows small signs of decomposition when annealed for 30 h at 800 °C. However, (Ti,Al,Cr,Nb,Ta)N – predicted to be not that strain-stabilized – shows pronounced signs of decomposition after 30-h-annealing at 800 °C,

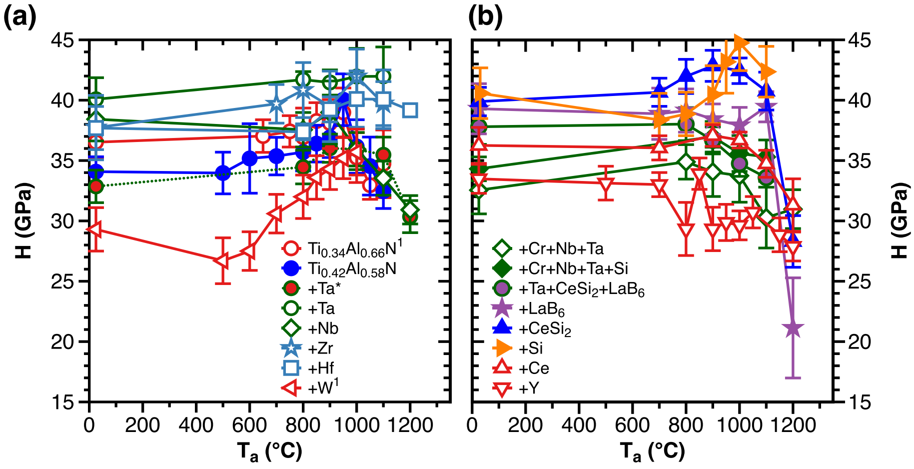

Fig. 19. Hardness of (Ti,Al)N and its alloys (which all were single-phase fcc in the as-deposited state) with (a) Hf ($Ti_{0.35}Al_{0.55}Hf_{0.10}N$ [260]), Zr ($Ti_{0.40}Al_{0.55}Zr_{0.05}N$ [252]), Nb ($Ti_{0.35}Al_{0.57}Nb_{0.08}N$ [268]), and Ta ($Ti_{0.42}Al_{0.48}Ta_{0.10}N$ [193]) after vacuum-annealing at T_a for 1 min, and (b) Y ($Ti_{0.51}Al_{0.47}Y_{0.02}N$ [228,229]), Ce ($Ti_{0.48}Al_{0.50}Ce_{0.02}N$ [257,258]), Si (7 at% Si, unpublished), $CeSi_2$ ($Ti_{0.50}Al_{0.50}N(CeSi_2)_{0.02}$ [257]), LaB_6 ($Ti_{0.43}Al_{0.57}N(LaB_6)_{0.02}$ [255]), Ta + $CeSi_2$ + LaB_6 ($Ti_{0.43}Al_{0.43}Ta_{0.14}N(CeSi_2)_{0.01}(LaB_6)_{0.01}$ [262]), and Cr + Nb + Ta and Cr + Nb + Ta + Si ($Ti_{0.21}Al_{0.21}Cr_{0.26}Nb_{0.16}Ta_{0.16}N$ and 6.4-at%-Si-alloyed $Ti_{0.21}Al_{0.20}Cr_{0.28}Nb_{0.16}Ta_{0.14}N$ [298]) after vacuum-annealing at T_a for 10 min. For comparison, data of $Ti_{0.44}Al_{0.44}Ta_{0.12}N$ [258] (labeled Ta*) are added to (a) to show that alloying elements require an adjustment in deposition parameters for optimized properties. This sample differentiates from $Ti_{0.42}Al_{0.48}Ta_{0.10}N$ (which presents the highest H-vs-T_a in (a)) by different deposition conditions (same type of deposition system and $Ti_{0.46}Al_{0.46}Ta_{0.08}$ target) and a longer annealing time of 10 min at T_a. The total (Ar + N_2) deposition pressure p_T = 0.5 Pa, N_2-to-total pressure ratio p_{N2}/p_T = 0.4, substrate temperature T_s = 500 °C, substrate bias U_b = –50 V, and target power density P ≈ 9 W/cm^2 for $Ti_{0.42}Al_{0.48}Ta_{0.10}N$ [193], while p_T = 0.35 Pa, p_{N2}/p_T = 0.2, T_s = 430 °C, U_b = –50 V, and P ≈ 11.5 W/cm^2 for $Ti_{0.44}Al_{0.44}Ta_{0.12}N$ [258]. Thus, the latter (with a lower H-vs-T curve) was prepared especially with a much lower N-supply (lower p_{N2}/p_T and larger P). For comparison, also the data of arc-evaporated $Ti_{0.34}Al_{0.66}N^1$ from [28] – also presented in Fig. 5a here – is added to (a) as well as those for $Ti_{0.53}Al_{0.39}W_{0.08}N$ (+W^1) [297], which exhibits the formation of W Guinier–Preston zones upon annealing. The annealing time at T_a for these coatings (marked with a superscript 1) was 2 h.

where AlN domains are embedded in an otherwise still homogenous (Ti,Cr,Nb,Ta)N matrix. This example and its Si-alloyed variant will be added to the discussion of hardness evolution and oxidation resistance of (Ti,Al)N based materials.

The change in hardness caused by the phase transformations upon annealing is given in Fig. 19a for the base material $Ti_{0.42}Al_{0.58}N$ and for its quaternary alloys with Nb and Ta (5 VE), Zr and Hf (4 VE and isovalent to Ti), and Y (3 VE). Due to the already discussed narrowing of the fcc-$Ti_{1\text{-}x}Al_xN$ phase range by the addition of Y only up to 2 at% Y could be alloyed to this base system (with $x \approx 0.52$) when keeping the structure single-phase fcc. All hard coatings presented in Fig. 19 had a single-phase fcc structure in their as-deposited state. The base system $Ti_{0.42}Al_{0.58}N$ shows very clearly the hardness increase induced by spinodal decomposition with $T_a \approx 950$ °C. Such a distinct hardness increase is not seen in the Y-alloyed coatings. On the contrary, the hardness declines at higher temperatures due to recovery processes occurring, the reduced cohesive energy by Y, and the formation of hcp-AlN. Coatings alloyed with Zr, Hf, Nb, and Ta show again a hardness increase with higher annealing temperatures, but not as pronounced as for $Ti_{0.42}Al_{0.58}N$. This may stem from the fact that these materials start at a much higher hardness level (due to the additional par-elastic and di-elastic interactions effective here, as discussed above). Or the “sweet-spot” was missed, which for $Ti_{0.42}Al_{0.58}N$ is for example only between 900 and 1000 °C and an annealing time of a few min, see Figs. 5, 7b, and 19a.

However, it is remarkable that the Zr, Hf, and Ta alloyed coatings still show hardness values of ≈ 40 GPa even after heat treatment at 1100 °C. These coatings accordingly do not show any hcp-AlN phase formation at this temperature (see Fig. 17a and 18b). The little increase in background of the XRD pattern for the Hf-alloyed one might indicate the formation of a small fraction of hcp-AlN, but as highlighted in [154,155], the thereby associated increased strain (due to the larger specific volume of hcp-AlN with respect to fcc-AlN) can cause the hardness to increase. Remarkable is also the pronounced H increase by ≈ 9 GPa when annealing a W-alloyed (Ti,Al)N at 1000 °C, which stems from the additional formation of W Guinier–Preston zones, where atomic-plane-thick W disks populate {1 1 1} planes of the nitride matrix [297].

Fig. 19a additionally shows that for similar chemical compositions, $Ti_{0.42}Al_{0.48}Ta_{0.10}N$ and $Ti_{0.44}Al_{0.44}Ta_{0.12}N$, the H-vs-T curves can be shifted by ≈ 5 GPa to lower H values for $Ti_{0.44}Al_{0.44}Ta_{0.12}N$. Both coatings were prepared with the same type of deposition equipment and using the same $Ti_{0.46}Al_{0.46}Ta_{0.08}$ PM target, but the coatings with lower H values are obtained with a significantly lower N_2-to-total pressure ratio (p_{N2}/p_t, some details about the deposition parameters are given in the caption of Fig. 19). Unfortunately, the N/Me ratios of the coatings were only estimated with energy dispersive X-ray spectroscopy (EDS). However, upon vacuum-annealing the $Ti_{0.44}Al_{0.44}Ta_{0.12}N$ coating, prepared at lower p_{N2}/p_t, experiences the formation of a hex-Ta_2N phase [258], hinting towards a N-deficiency. This might be the reason for the observed lower hardness values.

The so-called high entropy metal sublattice coating, (Ti,Al,Cr,Nb,Ta)N, which contains Cr, Nb, and Ta, and thus many metals with a preference for Me_2N phases, experiences the formation of Me_2N phases already when vacuum-annealed to 900 °C [298] (≈ 100 °C earlier than hcp-AlN can be detected). Consequently, the hardness for this coating – after a small increase with $T_a = 800$ °C – declines early, Fig. 19b. This can be postponed by the additional alloying with Si, which also increases the overall hardness by ≈ 2 GPa.

Also, the Ta + $CeSi_2$ + LaB_6-alloyed (Ti,Al)N experiences an early formation of a hex-Ta_2N phase (even ≈ 200 °C earlier than the formation of hcp-AlN can be detected) [262], causing the hardness to decline already with $T_a \geq 900$ °C, Fig. 19b. This is not the case for the Ta-free films presented in Fig. 19b, and especially the B or Si alloyed ones exhibit rather high (close to and even above 40 GPa) hardness values. Further details on the individual material systems can be found in the references given in the caption of Fig. 19.

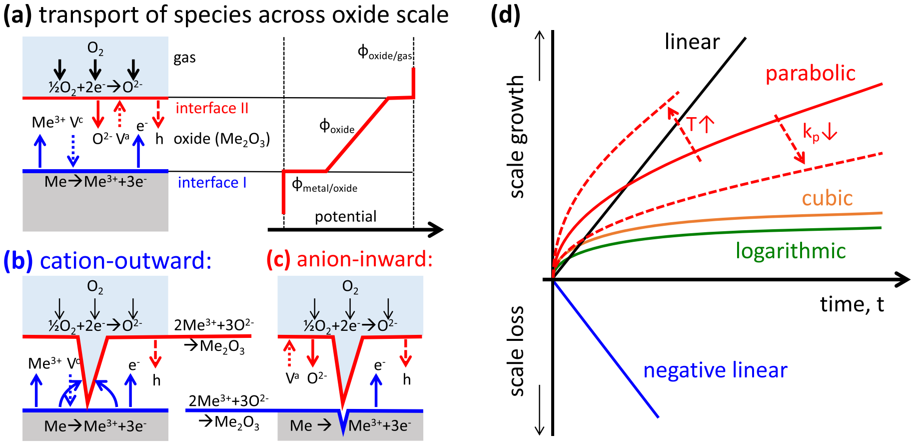

Fig. 20. (a) Transport of species (Me^{n+}, O^{2-}, e^-, electron holes, h, cation and anion vacancies, V^c, V^a) across the oxide scale (here for the example of Me_2O_3, and Me^{3+}), which solely grows at the interfaces I or II driven by the potential (Φ) gradient. If e^- are the slowest (like in Al_2O_3), the faster species (cation or anion) determine the place of oxidation. (b) Cation outward diffusion dominated growth promotes growth at outer interface II (allowing small cracks to be healed), according to an n-type semiconductor. Coupled movement of Me^+ and e^-. (c) Anion inward diffusion dominated growth promotes growth at the inner interface I (cracks can and will grow into metal), according to a p-type semiconductor. (d) Schematic presentation of the major oxide scale growth kinetics. Typically, the oxides grown on Ta and Nb follow a linear kinetic, those on Fe, Ni, Cu, Al, and Si follow a parabolic law, and those on Mo and W follow a negative linear kinetic (above certain temperatures, where volatile oxides form). Adapted from [300,301].

3. Oxidation and oxidation protection

In addition to the excellent thermomechanical properties of hard coatings, their stability in oxidizing and corrosive ambient media is crucial. In the following, this is illustrated in more detail using the example of oxidation resistance.

3.1. Some materials science basics

Oxidation in its most general sense is a chemical reaction between two species, one donates electrons (the oxidizing species, being oxidized) to the other (the oxidizing agent, being reduced). Considering that all base metals are eager to form oxides [299], the question is not whether oxidation occurs, but on what time scale it occurs.

At low temperatures, the diffusion processes required for this run relatively slowly, but at elevated temperatures, the strong oxidation tendency of many metals can negatively influence their property profile. If the forming oxide can cover the surface of the material with a continuous thin layer and allows even a low mobility for the reactants (metal, oxygen, or in the case of the nitrides discussed here, also nitrogen), a progressing oxidation process is very strongly inhibited by the forming oxide layer. Further oxide growth can only occur – which takes place solely at the inner interface (I, oxide/metal) or outer interface (II, oxide/gas) – upon a transport of needed species (Me^{n+}, O^{2-}, e^-, electron holes h, cation and anion vacancies, V^c, V^a) across the oxide scale driven by the potential gradient, as schematically presented in Fig. 20a.

A very prominent example of this is Al, which immediately (on contact with atmospheric oxygen) covers itself in a protective thin layer of Al_2O_3. Al_2O_3 offers one of the slowest ionic mobility in solids and is therefore an excellent protective layer against further oxidation. SiO_2 or Cr_2O_3 behave similarly. Therefore, alloys with additions of Al, Cr, and Si (where thin, well-adherent Al_2O_3, Cr_2O_3, and SiO_2 oxide layers can form) provide excellent protection in oxidizing atmospheres [302–304].

3.1.1. Transport mechanisms

The oxidation of metals (e.g. $3Me + O_2 \rightarrow Me_2O_3$) proceeds by two basic separate reactions: the anodic reaction at interface I ($Me \rightarrow Me^{3+} + 3e^-$) and the cathodic reaction at interface II ($^2/_3 O_2 + 3e^- \rightarrow 3O^{2-}$) [301], see Fig. 20a.

The metal cations – released from the nitride at the metal/oxide interface – migrate through the oxide to the oxide/gas interface via vacancy diffusion (cation vacancies, V^c) or using interstitial sites. The electrons also migrate with them and enable the cathodic reaction at this interface to produce the oxygen anions. These simultaneously migrate through the oxide via vacancy diffusion (anion vacancies, V^a) or using interstitial sites. If the cation outward diffusion is dominating, the oxide formation tends to occur/proceed at the outer interface II (oxide/gas), Fig. 20b. Via this mechanism, cracks within the oxide scale could even be healed. Contrary, if anion inward diffusion is dominating, the oxide formation tends to occur/proceed at the inner interface I (metal/oxide). Any cracks within the oxide scale, which provide fast-diffusion channels, would promote oxidation into the metal at these regions, Fig. 20c. The vacancies can coalesce to form cavities/pores (sometimes named Kirkendall voids) at or behind the oxide/metal interface, which usually favors such accumulation [301].

Just to give a short insight into the complexity of the oxidation and diffusion processes: In *p*-type oxides like NiO, cation vacancies (due to excess oxygen) provide a transport mechanism for the metal. While in *n*-type oxides such as TiO_2, anion vacancies (due to excess metal) provide a transport mechanism for the metal. But other *n*-type oxides like Al_2O_3 accommodate the excess metal interstitially, which is then also the transport mechanism for this type of materials (via interstitial cations) [305]. Thus, any change in chemistry of the metal or nitride that oxidizes can easily alter the dominating transport mechanisms within the oxide scale that forms on it.

However, effective protective oxides are characterized by low diffusion coefficients for the species involved, which generally correlate with the melting point. This explains why α-Al_2O_3 ($T_m = 2054$ °C [306]), Cr_2O_3 ($T_m = 2424$ °C [307]), and SiO_2 ($T_m = 1713$ °C [308]) are protective oxides, while Cu_2O ($T_m = 1229$ °C) [307]) and FeO ($T_m = 1371$ °C [309]), for example, are less protective. Moreover, Al_2O_3, Cr_2O_3, and SiO_2 are electrical insulators and efficiently slow down the transport of electrons, which are typically the fasted among the species involved [303,304], see Fig. 20.

Diffusion data for single-crystal Cr_2O_3 show that the diffusion of oxygen ions is three orders of magnitude smaller than that of Cr, thus, strongly indicating a cation-dominated defect structure, and that Cr_2O_3 layers grow mainly via cation diffusion [310–313], Fig. 20b. The actual cation transport at the Cr/Cr_2O_3 interface (at low oxygen partial pressures) occurs via an interstitial mechanism [302,312–315]. In contrast, at near-atmospheric oxygen partial pressures, i.e. on the outside of the Cr_2O_3 layer, Cr_2O_3 is an intrinsic electron conductor [313].

At temperatures well below the melting point T_m (i.e. at $T < 0.6\ T_m$), the dominant transport mechanism of the growing oxide layers is via defect sites such as dislocation cores or grain boundaries, rather than via bulk diffusion itself. In most applications, Cr_2O_3 or Al_2O_3 are in this “low” temperature range [316]. Along with the predominant cation transport, diffusion of O- anions also occurs along the oxide grain boundaries [317–322]. Thus, in the mostly polycrystalline oxide layers, both cation and anion diffusion (Fig. 20c) are involved in the thickness growth of the oxides [302,323–325].

Preferred cation diffusion is noticed in Cu_2O, FeO, Fe_3O_4, NiO, CoO, and Cr_2O_3, while preferred anion diffusion is noticed in TiO_2, ZrO_2, SiO_2, and Fe_2O_3, when exposed to air.

3.1.2. Oxide scale growth rates

Tammann [326] used Wagner’s oxidation theory [327], which considers that the rate determining step of oxide growth is the diffusion of species through it, to show that the oxide scale thickness *y* follows a parabolic law with time *t* [328]:

$$y^2 = k_p \cdot t + A_p \tag{21}$$

k_p is the parabolic rate constant and A_p is a constant. This is valid if there is a steady chemical potential gradient between the oxide/metal and gas/oxide interfaces (Fig. 20a), allowing to use Fick's first law [329]. Hence, the oxide scale needs to be dense, homogeneous, charge neutral, or relatively thick to have chemical equilibrium at these interfaces I and II. Otherwise, the scale growth kinetics deviates from parabolic [330] to follow more a linear, cubic or logarithmic law, see Fig. 20d. The latter applies for oxides having thicknesses below the Debye length, according to the Cabrera and Mott theory [331]:

$$y = k_{lg} \cdot \log\left(A_{lg} \cdot t + B\right) \tag{22}$$

k_{lg} is the logarithmic rate constant, A_{lg} and B are further constants.

There, the rate determining step is point defect formation in the oxide at the interfaces I or II. Because the ion transport through the film is accelerated by an electric field, built by tunneling of electrons from the metal to the adsorbed oxygen at the oxide/gas interface. As this is predominant at lower temperatures, oxide scale growth often follows a logarithmic law only at lower temperatures [328]. With increasing film thickness the electric field decreases resulting in negligible growth rates after some time. Such critical thicknesses, up to which space charges are present, are a few 100 nm for Cr_2O_3 or Al_2O_3, due to their inherently low defect concentration (their Debye length is a few 10 nm) [330]. If electron transport is possible, e.g., in semiconducting oxides or by thermionic emission, the model is valid also for thicker oxides.

For oxides with dominating grain boundary mechanisms, the scale growth often follows another sub-parabolic law, e.g. the cubic one [332]:

$$y^3 = k_c \cdot t + A_c \tag{23}$$

k_c is the cubic rate constant and A_c is a constant. For example, the alumina scale growth on Fe–Cr–Al alloys (containing reactive elements, RE) follows a sub-parabolic kinetic, because there the rate determining step is diffusion of O at the oxide grain boundaries. As the grain size increases along the thickness of the scale and thus with increasing scale thickness, but also with ongoing thermal exposure (causing the grain boundary density to decrease with time), the kinetics follow a sub-parabolic law (often close to cubic) [332].

If the phase boundary reactions to form the oxide (at interface I and/or II, see Fig. 20) are rate determining, the oxide scale growth follows a linear law ($y = k_l \cdot t$, where k_l is the linear growth rate). This is likely for porous oxide scales, allowing for a fast diffusion of the reactive species, not like in compact layers. But especially for the oxidation of ceramic-like materials, the metal species need to be provided fast enough at interface I (ceramic/oxide), otherwise the diffusion of metals from such a ceramic (like the nitride coatings considered here) to this interface is rate-limiting. Therefore, nitrides show typically only at the beginning a linear-like oxidation kinetic, even if the oxide scale is porous. If oxidation of metals, or other materials with fast supply of metals species to the oxide interface, causes the formation of a compact scale, the phase boundary reactions (at interface I and/or II) only limit the overall kinetics at the beginning. As soon as the diffusion through the scale is limiting the growth rate, the oxidation kinetics change from linear to parabolic (or cubic or logarithmic).

Whenever characterizing the oxide growth kinetic for metal nitrides (MeN) through the detection of mass changes (as typically done for characterizing the oxidation kinetics of metals), we need to consider that simultaneous to the weight gain (upon oxidation) there is also weight loss due to the conversion of a nitride into an oxide, e.g.:

$$2MeN + \frac{3}{2}O_2 \rightarrow Me_2O_3 + N_2, \text{ or} \tag{24}$$

$$2MeN + 2O_2 \rightarrow 2MeO_2 + N_2 \tag{25}$$

A simultaneous mass-gain and loss during oxidation occurs also if the oxidation product is (partly) volatile, like during oxidation of Mo, W, Cr, or B. For Cr_2O_3, especially at temperatures above 1000 °C, volatile oxides may form [$Cr_2O_3(s) + 3/2O_2(g) \rightarrow 2CrO_3(g)$] [310,333,334]. Therefore, thermo-gravimetric measurements should always be complemented by other methods like X-ray diffraction or electron microscopy, otherwise incorrect conclusions could be drawn. Especially if mass-gain and loss are completely superimposed, which would indicate that there is no change. Very often, parabolic oxide growth may also be superimposed on linear oxide growth.

According to Eqs. (24) and (25) any oxidation of nitrides releases N_2, thus N_2 needs to be removed, which might be difficult especially if there is a considerable oxide formation at the interface I (coating/oxide). If the oxide scale is an effective barrier against N_2-diffusion, the Me/N ratio within the nitride coating will change as well, especially close to interface I. This naturally influences any ongoing oxidation. Furthermore, the stoichiometry of the nitride coating itself can change, which is nicely shown for the oxidation of Cr_2N, in which the fraction of CrN gradually increases upon ongoing oxidation [335]. The effective volumes (per one mole of metal atoms) for Cr_2O_3, CrN, and Cr_2N are $\approx$ 14.6, 10.7, 8.8 cm^3, leading to PBR's of $\approx$ 1.4 and 1.7, respectively.

Analogous to diffusion, the oxidation rates also follow the Arrhenius law and, thus, increase exponentially with temperature [304]:

$$k_p = k_{0,p} \cdot e^{-\frac{Q_p}{RT}} \tag{26}$$

where $k_{0,p}$ is a constant and Q_p the activation energies for parabolic growth, correspondingly, this is valid for the other rate laws, e.g., logarithmic or cubic.

The temperature dependence of typical parabolic growth rates for Al_2O_3, Cr_2O_3, and TiO_2 forming metallic compounds is shown in

Fig. 21a. Furthermore, oxidation rates obviously depend on the O partial pressure, so that increasing O partial pressures cause increasing rates [303,304]. This figure shows that whenever the oxidation resistance needs to be improved, alumina, silica, or chromia formers are added. And relevant for (Ti,Al)N-based coatings, the formation of TiO_2 should be suppressed. Therefore, high-Al-containing (Ti,Al)N coatings typically provide a better oxidation resistance, as well as Cr and/or Si alloyed ones.

In contrast to Cr_2O_3, which crystallizes only in its stable corundum structure (α-Cr_2O_3), several metastable, fast-growing polymorphs occur in Al_2O_3 in addition to the stable α-modification. Metastable Al_2O_3 polymorphs (e.g., γ and θ) generally form below 900 °C, while the slow-growing α-Al_2O_3 tends to occur at higher temperatures [336,337]. The γ- and θ-phase most likely grow via transport of Al^{3+} ions [338–340]. However, even the slowest growing oxide layer can only protect the underlying material from further oxidation if it has excellent adhesion to that material. In addition to these important parameters, we always need to consider any volume changes connected with the oxidation process.

Small compressive stresses are manageable (sometimes even wanted as thereby the compactness increases or fast diffusion pathways like grain boundaries become less preferrable), but tensile stresses (even small ones) are often intolerable. Correspondingly, also phase transformations within the oxide scale during exposure that would cause a reduction in specific volume are not wanted. A typical example for this is TiO_2, which tends to start forming in its anatase structure, but then transforms into the thermodynamically more stable rutile structure. If the accumulated compressive stresses within the oxide scale become too high – and the adhesion is too weak – the oxide scale tends to spall off, see the schematic of in Fig. 21b how compressive stresses could evolve and lead to local detachment (Fig. 21c), which finally cause failure (Fig. 21d).

As summarized in [305], Pilling and Bedworth [343] made the earliest attempt to describe the molar volume ratio between the oxide produced and the metal, respectively nitride, consumed, which is known in literature as the Pilling–Bedworth ratio, PBR ($PBR = \frac{V_{Oxide}}{n \cdot V_{Metal}}$, with n representing the number of metals in the oxide Me_nO_m). They assumed – based on the knowledge at those days that the predominating transport was always O to the metal – that a larger molar volume of the oxide than the metal consumed by its production leads to compressive stresses, while a lower oxide volume leads to a cellular and porous scale. In brittle oxide layers, these easily exceed their strength leading to spallation and/or cracking, providing an easy access of gaseous oxygen to the metal surface. A PBR of 1 would suggest a stress-free growth, < 1 leads to tensile stresses, whereas >1 tends to compressive stresses – preferred values are between 1 and 2. However, with proceeding experimental evidence, especially due to the development of marker and tracer experiments, it has become clear that transport of species through the oxide scale is much more complex, and that the PBR ratio provides a too simplified picture. Therefore, in practice the PBR is a poor descriptor, but still it is used to have an idea about possible stress developments. For the model-system of this review, (Ti,Al)N, the relevant primary oxides are α-Al_2O_3 and TiO_2 in its anatase (a-) and rutile (r-) structure [344]. The effective volume (per mole of metal atoms) of fcc-$Ti_{0.50}Al_{0.50}N$ is ≈ 11.0 cm^3, which is much smaller than that for the relevant oxidation products, α-Al_2O_3 (≈ 13.5 cm^3), a-TiO_2 (≈ 20.5 cm^3), and r-TiO_2 (≈ 18.9 cm^3). The derived PBR is thus smallest for α-Al_2O_3 (≈ 1.2), followed by r-TiO_2 (≈ 1.7), and highest for a-TiO_2 (≈ 1.9) when grown on (Ti,Al)N. As mentioned above, if used at all, these values need to be considered with care. But for sure problematic is the anatase-to-rutile TiO_2 transformation, because the connected volume reduction by 5–10 % [345,346] promotes the formation of pores and cracks within the oxide scale [301].

Thus, protective oxide scales should have the following most important characteristics:

- Dense, pore-free with continuous growth

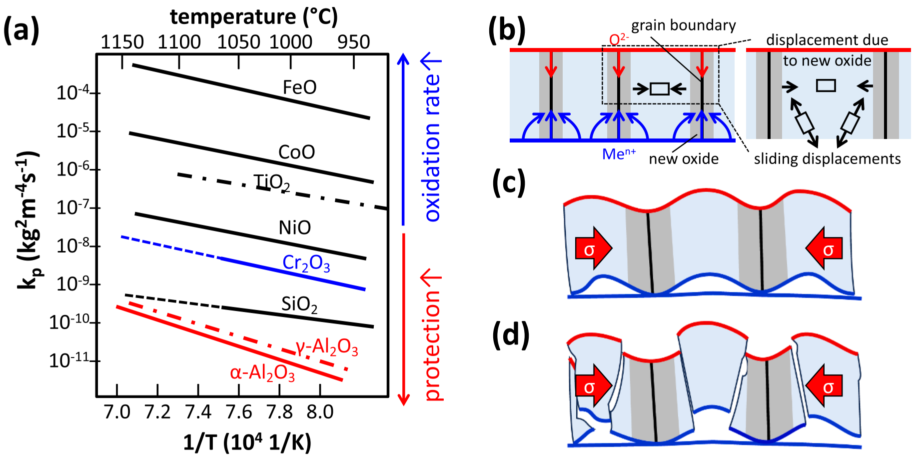

Fig. 21. (a) Arrhenius-plot of apparent parabolic growth rates k_p for Al_2O_3, SiO_2, Cr_2O_3, and TiO_2, compared to NiO, CoO, and FeO (modified from [302,336,341,342]). The transition from the solid to dashed lines for SiO_2 and Cr_2O_3 indicates that there the formation of volatile oxides may form, depending on the atmospheric conditions. Schematic presentation on how new oxide formation within scale grain boundaries of α-Al_2O_3 or Cr_2O_3 can lead to build-up of compressive stresses, which can cause interfacial sliding displacement (b). Local stress concentrations at interfacial irregularities or voids cause local detachment (c), which can cause scale failure (d), adapted from [337].

- Thermodynamically stable (high melting point and low vapor pressure)
- Low scale growth rate (low electrical conductivity and low diffusivity for anions and cations)
- Good adhesion to the material on which it grows (including not too high tensile and compressive stresses)

Additionally important are (which are not explicitly described here further):

- High temperature plasticity
- Self-healing ability of cracks
- Similar thermal expansion coefficient to the material on which it grows
- No local attack (like on grain boundaries)

Before discussing the oxidation resistance of (Ti,Al)N and how it can be improved – based on oxide scale growth rates derived from isothermal ambient air exposure at 850, 900, and 950 °C – we shortly look into the oxidation kinetics of CrN. This, because CrN is often a benchmark for transition metal nitrides in terms of oxidation resistance. Due to the rather limited thermal stability of CrN itself, as it dissociates towards Cr via Cr_2N upon exposure above ≈ 900 °C [347,348]. However, most oxidation studies available for CrN have been conducted at temperatures below 800 °C and only for a rather short time (a few hours). In order to have a plausible bench-mark also for 850 °C (the lowest temperature for the (Ti,Al)N-based materials discussed in Ch. 3.2), the oxide scale thicknesses on CrN after oxidation at 725, 750, 775, 800, and 825 °C presented in Fig. 22a, whereas the Arrhenius-plot for k_p is given in Fig. 22b [349]. This allows to estimate the k_p value for 850 °C using Eq. (26). The slope of the Arrhenius-plot gives the activation energy, which is ≈ 323 kJ/mol for the oxidation of this CrN coating. Other reported values cover quite a wide range from 110 kJ/mol [350] to 225 kJ/mol [351] to even 440 kJ/mol [335]. Important to mention is that the large value of 440 kJ/mol is for the parabolic oxidation step after the initial oxidation of the CrN surface. Reported activation energies of self-diffusion coefficients for Cr in Cr_2O_3 are 256 kJ/mol (61.1 kcal/mol) [352] and 419 kJ/mol (100 kcal/mol) [353].

The activation energy for the oxidation of Cr in the temperature range of 1000–1100 °C is 249 kJ/mol (59.4 kcal/mol), while the value at lower temperatures appears to be only 157 kJ/mol (37.5 kcal/mol) due to the interference from linear oxidation [333]. The comparison with these literature values for self-diffusion and oxidation of Cr suggests, that the wide range of activation energy for CrN oxidation indicates a wide range of morphologies of the Cr_2O_3 oxide scale formed. The latter also pronouncedly depends on the growth morphology of the CrN itself. The comparison of various CrN coatings showed an increased activation energy for their oxidation with increased compressive stresses, due to the more compact and dense growth morphology of the nitride itself [335].

The estimated k_p value for 850 °C corresponds to the results obtained for CrN reported in [350]. There, the presented SEM fracture cross-section for CrN after ambient air exposure for 2 h at 850 °C indicates an oxide scale thickness of 0.52 ± 0.04 μm (average of 4 measurement points). The corresponding parabolic fits border the colored region in Fig. 22b. When comparing oxidation studies, important is also to compare the conditions of the experiment, for example if the atmosphere was Ar + O_2, synthetic or ambient air. Especially if materials easily release nitrogen (like CrN), the results can be different when comparing studies done in Ar + O_2 or ambient air. Here, the massive N_2-supply of air will influence the dissociation of CrN to Cr_2N [348] and thereby the oxidation process itself.

However, the structure of the oxide layer on (Ti,Al)N is more complex than on CrN or TiN, which is due to different diffusion properties and tendencies to oxide formation of Ti and Al. The composition of oxide scales formed on (Ti,Al)N was studied in detail early on [157,355], and air-oxidized samples between 500 and 900 °C show a typical two-layer structure in all cases. Outermost there

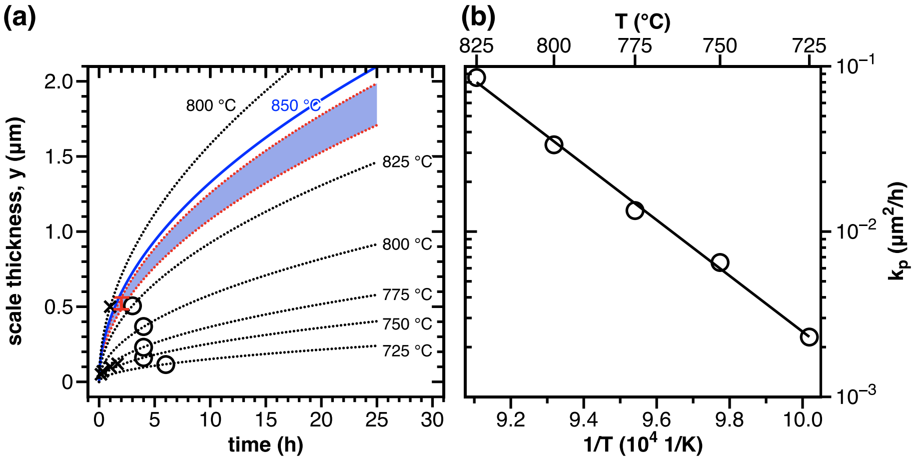

Fig. 22. (a) Oxide scale thicknesses on CrN as a function of time. The circles are from [349] and the crosses are from [354]. The parabolic fits give their k_p values, which are used to draw the Arrhenius plot (b). From this the k_p for 850 °C was calculated to draw the blue solid line in (a). This corresponds to the parabolic fits through the maximum and minimum value of the oxide scale thickness after 2 h at 850 °C, measured from [350], red dotted lines bordering the shaded region.

is Al_2O_3 with only a bit of Ti, followed by a layer composed mainly of titaniumoxide and oxynitride (with only a small amount of Al) above the nitride [356]. Additionally of importance is, if the substrate material is inert or if there is a massive diffusion into the nitride coating. For example, often Si is used as substrate for laboratory investigations, but Si massively diffuses into the coating already at temperatures slightly above 500 °C. Especially, if the coating is thin, e.g. below 2 µm, Si would influence also the oxidation process itself.

As mentioned above, the reactive element effect – improved adhesion of the oxide scale and blocking of their fast diffusion pathways such as grain boundaries by alloying small additions of REs like Y, Ce, and La to chromia and alumina formers – helps to improve the oxidation resistance of both structural and coating materials. But other alloying elements, like Nb and Ta (5 VE), Zr and Hf (4 VE and isovalent to Ti) are also able to improve the oxidation resistance. In one or another way, these elements promote the direct formation of r-TiO_2 or retard the transformation from anatase-to-rutile or promote the formation of a more-dense TiO_2. Important for our model system (Ti,Al)N is, that many of these elements are also beneficial for their thermomechanical behavior, as discussed in Ch. 2.2.4.

3.2. *Alloyed and microalloyed (Ti,Al)N*

The influence of the alloying elements on the oxidation resistance of (Ti,Al)N-based coatings is obtained by investigations of the oxide scales grown during isothermal treatments in ambient air at 850, 900, and 950 °C, see Fig. 23. To avoid any cross-diffusion with the substrate materials, mostly sapphire or polycrystalline Al_2O_3 substrates are used in the individual studies, as indicated in the caption of Fig. 23. As a reference, the oxide scale thickness grown on TiN is ≈ 2.2 µm after 2 h at 700 °C [39] respectively 0.5 µm after 1 min at 850 °C [357]. During dynamical DSC/TGA treatments, TiN shows with ≈ 500 °C an ≈ 400 °C earlier onset for massive oxidation than (Ti,Al)N [161]. CrN exhibits an ≈ 0.5 µm thick oxide scale after 3 h at 825 °C [335], Fig. 22.

The oxidation resistance of (Ti,Al)N generally increases with increasing Al content, see the results for samples #1, 2, 3, 4 (increasing Al content) at 850 °C in Fig. 23. $Ti_{0.25}Al_{0.75}N$, the one with highest Al content (#4), even survived 40 h at 850 °C, while the others fully transferred their ≈ 4 µm nitride into oxides [161]. Alloying (Ti,Al)N with Ta (#5, 6, 7), Nb (#8), Hf (#9), Zr (#10), Cr (#12), and Si (#13), or microalloying with Ce (#14), Y [229,344], LaB_6 (#15), and $CeSi_2$ (#16), further improves the oxidation resistance.

As mentioned above, the oxide scales grown on the (Ti,Al)N-based coatings consist of a relatively dense Al_2O_3 layer and a Ti-rich mixed oxide layer, see Fig. 24a. For an estimation, if $Ti_{0.50}Al_{0.50}N$ transforms into TiO_2 and Al_2O_3, their molar fractions would be 66.7 and 33.3 %, respectively. Thus, upon a full oxidation, the thickness of the original nitride would increase to 155 % (using molar

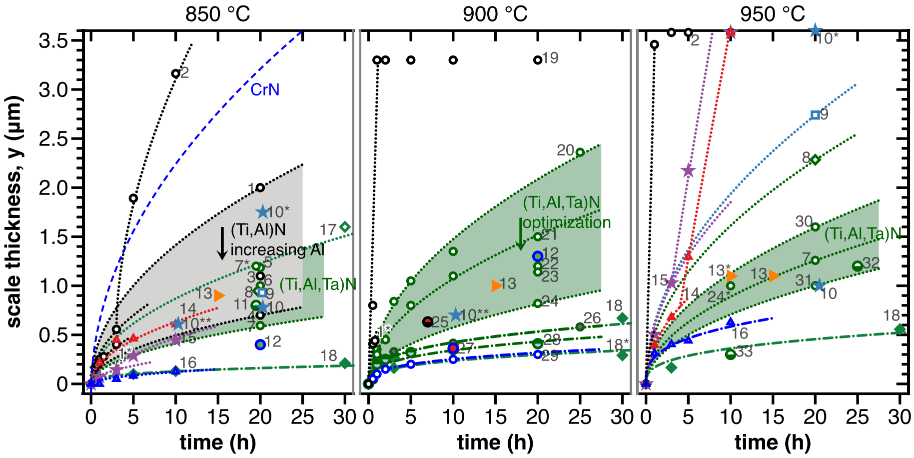

Fig. 23. Oxide scale thicknesses grown during isothermal ambient-air treatments at 850, 900, and 950 °C on (Ti,Al)N and its alloys: $Ti_{0.48}Al_{0.52}N$ (#1 [161]), $Ti_{0.50}Al_{0.50}N$ (#1* [114]), $Ti_{0.42}Al_{0.58}N$ (#2 [256]), $Ti_{0.38}Al_{0.62}N$ (#3) and $Ti_{0.25}Al_{0.75}N$ (#4) [161], $Ti_{0.43}Al_{0.42}Ta_{0.15}N^{arc}$ (#5 [358]), $Ti_{0.45}Al_{0.36}Ta_{0.19}N^{arc}$ (#6 [359]), $Ti_{0.42}Al_{0.48}Ta_{0.10}N$ (#7 [193]), $Ti_{0.47}Al_{0.45}Ta_{0.08}N^{arc}$ (#7* [344]), $Ti_{0.35}Al_{0.57}Nb_{0.08}N$ (#8 [268]), $Ti_{0.35}Al_{0.55}Hf_{0.10}N$ (#9 [260]), $Ti_{0.40}Al_{0.55}Zr_{0.05}N$ (#10 [252]), $Ti_{0.49}Al_{0.44}Zr_{0.07}N^{arc}$ (#10* [344]), $Ti_{0.45}Al_{0.49}Zr_{0.06}N^{arc}$ (#10** [360]), $Ti_{0.54}Al_{0.45}N^{arc}/Ta_{0.82}Al_{0.18}N^{rsd}$ (#11 [359]), $Ti_{0.18}Al_{0.35}Cr_{0.47}N$ (#12 [361]), $Ti_{0.43}Al_{0.48}Si_{0.09}N^{arc}$ (#13 [287]), $Ti_{0.56}Al_{0.34}Si_{0.10}N^{arc}$ (#13* [360]), $Ti_{0.48}Al_{0.50}Ce_{0.02}N$ (#14 [257,258]) – $Ti_{0.50}Al_{0.48}Y_{0.02}N^{arc}$ (#14* [344]) and $Ti_{0.51}Al_{0.47}Y_{0.02}N$ (#14** [229]) show oxide scale thicknesses of ≈ 1.2 and ≈ 0.95 µm after 20 h at 850 °C, respectively, which are not presented as there are too many data points in this region – $Ti_{0.43}Al_{0.57}N(LaB_6)_{0.02}$ (#15 [255]), $Ti_{0.50}Al_{0.50}N(CeSi_2)_{0.02}$ (#16 [257]), $Ti_{0.21}Al_{0.21}Cr_{0.26}Nb_{0.16}Ta_{0.16}N$ (#17), 6.4-at%-Si-alloyed $Ti_{0.21}Al_{0.20}Cr_{0.28}Nb_{0.16}Ta_{0.14}N$ (#18), and 9.8-at%-Si-alloyed $Ti_{0.21}Al_{0.20}Cr_{0.27}Nb_{0.17}Ta_{0.14}N$ (#18*) [298,362], $Ti_{0.54}Al_{0.46}N^{arc}$ (#19 [363]), $Ti_{0.44}Al_{0.44}Ta_{0.12}N$ (#20 [258]), $Ti_{0.49}Al_{0.44}Ta_{0.07}N^{arc}$ (#21) and $Ti_{0.44}Al_{0.41}Ta_{0.15}N^{arc}$ (#22) [264], $Ti_{0.40}Al_{0.54}Ta_{0.06}N^{arc}$ (#23) and $Ti_{0.34}Al_{0.54}Ta_{0.12}N^{arc}$ (#24 [263]), $Ti_{0.34}Al_{0.48}Ta_{0.18}N^{arc}$ (#24* [360]), $(Ti,Al)N^{arc}/MoSiB^{rsd}$-multilayer (λ = 37 nm, #25 [364]), $Ti_{0.43}Al_{0.43}Ta_{0.14}N(CeSi_2)_{0.01}(LaB_6)_{0.01}$ (#26 [262]), $Cr_{0.45}Al_{0.53}Y_{0.02}N$ (#27 [253]), $Ti_{0.49}Al_{0.44}Ta_{0.07}N^{arc}/Al_{0.62}Cr_{0.38}N^{arc}$ (#28) and $Al_{0.62}Cr_{0.38}N^{arc}$ (#29) [264], $Ti_{0.30}Al_{0.54}Ta_{0.16}N^{arc}$ (#30) and $Ti_{0.32}Al_{0.60}Ta_{0.08}N^{arc}$ (#31) [358], $Ti_{0.51}Al_{0.43}Ta_{0.06}N^{arc}/Ta_{0.77}Al_{0.23}N^{rsd}$-multilayer (λ = 13 nm, #32 [365]), $Ti_{0.34}Al_{0.48}Ta_{0.18}N^{arc}/Ti_{0.56}Al_{0.34}Si_{0.10}N^{arc}$-multilayer (#33 [366]). The dotted lines are parabolic fits through the individual oxide scale thickness values, while the dash-dotted ones are cubic fits (for #16, 18, 26, 28, 29).

volumes of ≈ 11.0, 13.5, and 18.9 cm^3 for fcc-$Ti_{0.50}Al_{0.50}N$, α-Al_2O_3, and r-TiO_2, respectively) or its weight would increase to 170 % (using molar weights of ≈ 51.4, 102.0, and 79.9 g for $Ti_{0.50}Al_{0.50}N$, Al_2O_3, and TiO_2). With the difference in molar fraction and volume between α-Al_2O_3 and r-TiO_2, the oxide scale grown on $Ti_{0.50}Al_{0.50}N$ easily consists of 70–75 % TiO_2. The thermodynamically more stable form of TiO_2 is rutile, but anatase easier nucleates and is preferred for small grain sizes. This is why typically a-TiO_2 is formed first and phase-transforms to r-TiO_2 upon a time or temperature increase. This is unfortunately connected with a volume reduction as a-TiO_2 has 20.5 cm^3/mol, leading to cracks (see Fig. 24a), which, in turn, promotes further oxidation. As McInyre et al. [114] noted, the mobile species are essentially Al and O (at ≈ 800 °C), and while Al diffuses through the sublayer of the Ti-rich oxide towards the oxide/gas interface, the oxygen counterdiffusion flow delivers O to the nitride/oxide interface for a further formation of the Ti-rich oxide.

With a much higher Al content, here shown for $Ti_{0.25}Al_{0.75}N$, especially the porous Ti-rich mixed part massively decreases, Fig. 24b, leading to the much-improved oxidation resistance. Unfortunately, the $Ti_{0.25}Al_{0.75}N$ coating typically crystallizes with the hcp structure, due to the Al content being above x_{max} for a complete single-phase fcc structure, see Fig. 12. This leads to reduced mechanical strength, and therefore we will concentrate here on possibilities to improve oxidation resistance of (Ti,Al)N-based materials without sacrificing mechanical strength. In particular, the Ti-rich mixed oxide layer needs improvements (i.e. it should be less porous and without cracks) so that the Al-rich oxide layer above it can develop its full effect [114,252]. Especially for the TM alloyed materials, the Ti-rich mixed oxides contain these elements often as a solid solution, and therefore thereby alloyed (Ti,Al)N shows a further improvement in oxidation resistance, Fig. 23. This is particularly the case for Ta, where fully oxidized (Ti,Al)N/(Ta,Al)N multilayer exhibits a homogenous distribution of Ti, Ta, and O throughout the scale [359]. These observations agree well with studies on arc-evaporated Ti-Al-Ta-N films [250], which suggest that partial-substitution of Ti in TiO_2 with Ta also leads to a lower density of oxygen vacancies, which delays oxygen diffusion [250,367].

The a-TiO_2-to-r-TiO_2 transformation can be retarded by Al, Y, or Zr [345,368,369]. Therefore, Zr addition to $Ti_{1-x}Al_xN$ improves its oxidation resistance especially in the lower temperature regions [360]. Contrary, Ta promotes the direct formation of r-TiO_2 [358,344]. One of the Ta-oxides is isostructural related to r-TiO_2, thus solid solution r-$(Ti,Ta)O_2$ phases are observed during oxidation of (Ti,Al,Ta)N. Tantalum is thus able to completely avoid the undesirable anatase-to-rutile transformation (by promoting the direct formation of rutile), while Y and Zr can only delay or postpone it. However, extremely important is the Al content, which should be maximized first, as mentioned above for non-alloyed (Ti,Al)N. $Ti_{0.25}Al_{0.75}N$ shows even after 40 h oxidation at 850 °C only a 1.1 μm thick oxide scale [161]. This is also valid for the alloyed (Ti,Al)N coatings, which should have a high Al-content as well, compare for example #5 and #7 of the (Ti,Al,Ta)N coatings in Fig. 23 for 850 °C. As Ta modifies the growing r-TiO_2, also the Ta content should not be too high, compare #6 and #7. Detailed studies show that (Ti,Al,Ta)N provides excellent oxidation resistance for Al/Ti ratios ≈ 2 and Ti/Ta ratios ≈ 3 [358] (hence, a composition close to $Ti_{0.3}Al_{0.6}Ta_{0.1}N$), compare #20 ($Ti_{0.44}Al_{0.44}Ta_{0.12}N$) and #24 ($Ti_{0.34}Al_{0.54}Ta_{0.12}N^{arc}$) at 900 °C, or $Ti_{0.30}Al_{0.54}Ta_{0.16}N^{arc}$ (#30) and $Ti_{0.42}Al_{0.48}Ta_{0.10}N$ (#7) as well as $Ti_{0.32}Al_{0.60}Ta_{0.08}N^{arc}$ (#31) at 950 °C in Fig. 23. Interestingly, the chemically very similar coatings $Ti_{0.42}Al_{0.48}Ta_{0.10}N$ (#7) and $Ti_{0.47}Al_{0.45}Ta_{0.08}N^{arc}$ (#7*) form the lower and upper bound of various (Ti,Al,Ta)N coatings at 850 °C, see the green-shaded regions.

The use of arc-evaporation instead of sputtering (or vice versa) cannot be considered a guarantee of better oxidation resistance. More important is a dense microstructure and the optimized chemical composition. As the coatings presented in Fig. 23 were mostly developed for improved mechanical performance (or at least to have excellent mechanical properties as well), an important point was their single-phase fcc structure in the as-deposited state. Often, arc-evaporation allows to combine this with a higher Al content, particularly for standard-near deposition conditions.

Important for the protectiveness of the oxide scale formed is also its structural complexity. For the Ta-alloyed (Ti,Al)N, even after 30 h oxidation treatments at 950 °C, solely α-Al_2O_3 and r-TiO_2-structured (with Ta solid solution) oxides are present (#30 and 31). Corresponding to the phases present in the oxide scale after 20 h at 850 °C (#7*), see the XRD patterns summarized in Fig. 25. But the

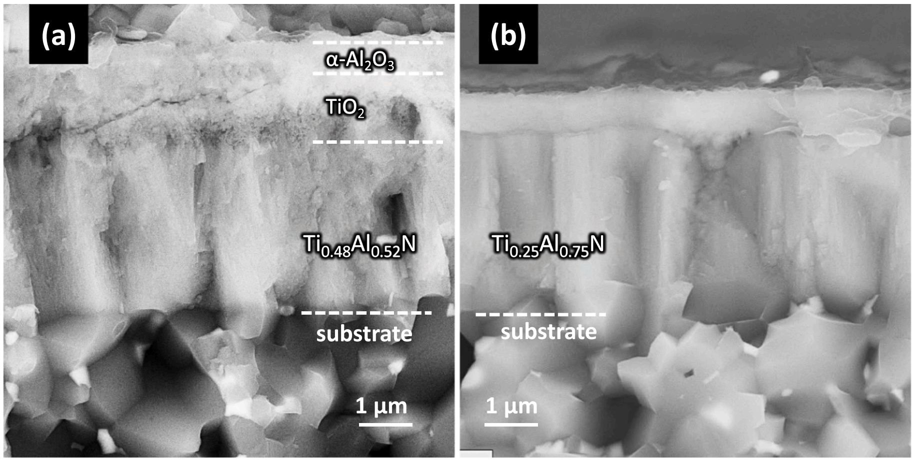

Fig. 24. SEM fracture cross-sections of (a) $Ti_{0.48}Al_{0.52}N$ and (b) $Ti_{0.25}Al_{0.75}N$ (on polycrystalline Al_2O_3) after isothermal oxidation for 20 h at 850 °C [161].

Y- and Zr-alloyed (Ti,Al)N coatings also provide other complex oxides such as yttrium titanate, like $Y_2Ti_2O_7$, and zirconium titanate, like $ZrTiO_4$, respectively, next to a-TiO_2, r-TiO_2, and α-Al_2O_3 [344]. Thus, Ta is helpful in this regard as it promotes the direct formation of r-TiO_2, avoiding other complex oxide phase formations, and additionally Ta enhances the formation of α-Al_2O_3. ZrO_2 and TiO_2 react to form $ZrTiO_4$ at ≈ 850 °C, which further reacts with TiO_2 to form $ZrTi_2O_6$ ($Zr_{0.33}Ti_{0.67}O_2$) [370].

These are the major phases (next to ZrO_2 and TiO_2) within the ZrO_2–TiO_2 phase diagram. Within the phase diagram SiO_2–TiO_2, there is no additional phase but a eutectic point at 6.3 % TiO_2 and 1552 °C [371], but there is a $ZrSiO_4$ phase within the SiO_2–ZrO_2 phase diagram [372]. The SiO_2–Al_2O_3 phase diagram also holds one additional phase, i.e. mullite ($3Al_2O_3{\cdot}2SiO_2$) [373]. However, its formation was not observed during oxidation of a Si-alloyed (Ti,Al)N, not even when increasing the temperature to 1200 °C (followed by an immediate cooling segment) [287]. No separate SiO_2-based crystalline phase could be detected there even after oxidation at 1200 °C. This is because SiO_2 has a strong glass-forming ability (e.g. it is the principal glass former in glazes) and combines with almost all oxides to bring them into a glass structure. Moreover, pyrochlore-type $Y_2Ti_2O_7$ forms during annealing of TiO_2 and Y_2O_3 powders at ≈ 800 °C [374]. Contrary, aluminum titanate Al_2TiO_5 (the only additional phase within the Al_2O_3–TiO_2 phase diagram) is formed above 1283 °C (upon a reaction between α-Al_2O_3 and TiO_2). Therefore, the latter is present if (Ti,Al)N was oxidized at 1450 °C, while only r-TiO_2 and α-Al_2O_3 is present if the oxidation temperature was only 950 °C, Fig. 25.

In this overview, the high entropy metal sublattice coating (Ti,Al,Cr,Nb,Ta)N (#17, 850 °C) is comparable to the weakest (Ti,Al,Ta)N coating (#5), mostly because of the much lower Al content. Considering this, the coating shows a remarkable oxidation resistance. This can be related to its single-crystalline-phase oxide scale (being rutile), which shows an excellent adhesion to the nitride from which it grows, Fig. 26a.

The oxide scale adopts the morphology from the nitride it substrates, but provides chemically a rather sharp transition and exhibits pores with 20–30 nm in diameter, Fig. 26b. By alloying this with 6.4 at% Si, the oxidation resistance can massively be improved to match that of the $CeSi_2$ microalloyed (Ti,Al)N, compare #18 and #16 in Fig. 23, respectively. With the help of Si, the oxide scale thickness even after 100 h at 850 °C is only 0.25 µm (2.7 µm without Si) [298]. Although the oxide scale still shows only a single-crystalline-phase r-TiO_2-based structure, it is divided in two regions, Fig. 26c. The inner oxide (oxide 1) is Si-rich and provides a gradual transition in chemistry and morphology to the nitride from which it grows, see Fig. 26d.

Very often the addition of Si massively improves the oxidation resistance of nitride coatings, see the Si-containing coatings (#16, 18, 26), which are among those with the thinnest oxide layers during oxidation at 850, 900, and 950 °C, Fig. 23. The effect is similar to that one presented for the HESN-Si coating, which has a well-adherent and dense Si-rich inner oxide layer and essentially a simple oxide structure. Interesting is here also the coating $Ti_{0.43}Al_{0.48}Si_{0.09}N^{arc}$ (#13), which shows an oxide scale thickness of ≈ 1 µm at 850, 900, and 950 °C, indicating a very stable scale formation. The oxide growth kinetics of the Si-containing nitride coatings follow more a cubic like behavior rather than a parabolic one. Thus, the oxide scale initially grows faster, but then provides a protective nature with slow kinetics.

The Arrhenius-plot, as shown in Fig. 27a, indicates an activation energy Q_p of 45.8 kJ/mol for the parabolic oxidation of $Ti_{0.43}Al_{0.48}Si_{0.09}N^{arc}$ (#13). Interestingly, $Ti_{0.40}Al_{0.55}Zr_{0.05}N$ (#10) also provides a rather low Q_p of 56.8 kJ/mol, but its chemical relative, i.e. $Ti_{0.49}Al_{0.44}Zr_{0.07}N^{arc}$ (#10*), was already fully oxidized after 20 h at 950 °C (which indicates a much larger Q_p as both have a similar k_p at 850 °C). The Al-leaner $Ti_{0.57}Al_{0.38}Zr_{0.05}N$ (2.1 µm thin), even fully oxidized during the 1 h exposure to air at 700 °C [164]. The reasons for the better performance of $Ti_{0.40}Al_{0.55}Zr_{0.05}N$ compared to $Ti_{0.49}Al_{0.44}Zr_{0.07}N^{arc}$ could be the higher Al and lower Zr content. Both coatings exhibit a layered oxide scale with an outermost, dense α-Al_2O_3, but the mixed Ti-Zr-O layer is more likely a $Zr_{0.33}Ti_{0.67}O_2$ on $Ti_{0.40}Al_{0.55}Zr_{0.05}N$ [370] and a $ZrTiO_4$ on $Ti_{0.49}Al_{0.44}Zr_{0.07}N^{arc}$ [344]. The chemically closer $Ti_{0.45}Al_{0.49}Zr_{0.06}N^{arc}$

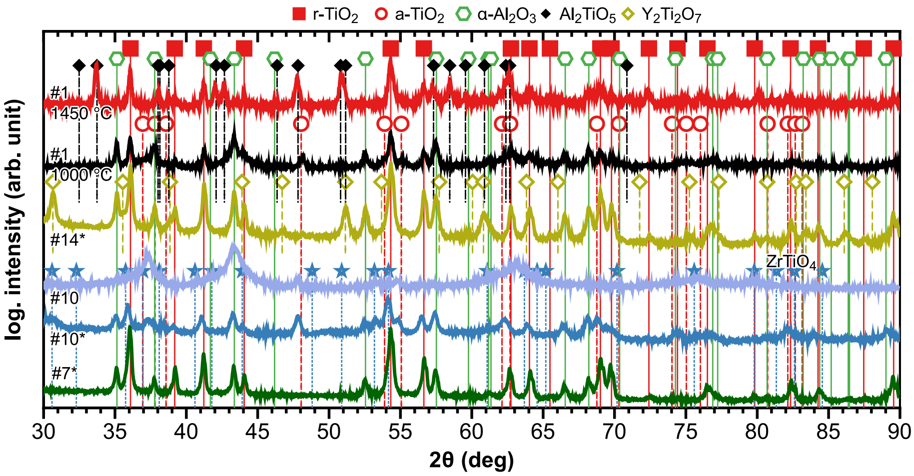

Fig. 25. XRD patterns of $Ti_{0.48}Al_{0.52}N$ (#1) after dynamic oxidation to 1450 °C and isothermal oxidation at 1000 °C for 1 h (in synthetic air). The alloyed (Ti,Al)N coatings (#7* $Ti_{0.47}Al_{0.45}Ta_{0.08}N^{arc}$ [344], #10* $Ti_{0.49}Al_{0.44}Zr_{0.07}N^{arc}$ [344], and #14* $Ti_{0.50}Al_{0.48}Y_{0.02}N^{arc}$ [344]) are oxidized for 20 h at 950 °C, while #10 ($Ti_{0.40}Al_{0.55}Zr_{0.05}N$ [252]) is oxidized for 1 h at 1000 °C, which still shows pronounced contributions from the fcc nitride (broad XRD peaks at 2θ ≈ 37 and 43°).

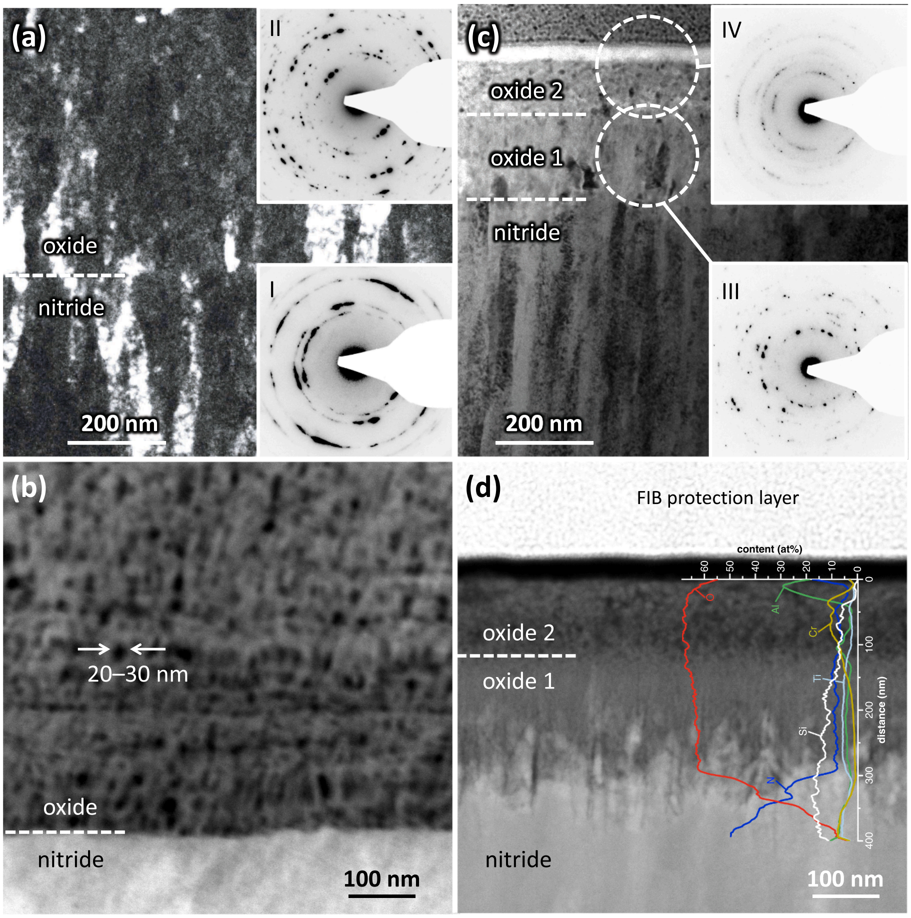

Fig. 26. Cross-sectional TEM investigations of the HESN coating (Ti,Al,Cr,Nb,Ta)N (#17) without Si (a) and (b), and with 6.4 at% Si (#18) (c) and (d) after oxidation in air at 850 °C for 100 h. (a) is a dark field TEM, (c) a bright field TEM, (b) and (d) STEM studies. The remaining nitride is still single-phase fcc structured (SAED inset I), and all oxide regions indicate a single-phase rutile structure (SAED inset II for Si-free; and III and IV for oxide 1 and oxide 2 of the Si-containing film). (b) The oxide scale itself is homogeneous in morphology and chemistry, except for the Al-and O-rich outermost region (not shown). (d) The oxide itself has gradual changes in morphology and Si as well as Cr contents. The inner Si-rich region (oxide 1) is denser than the outer Cr-rich region (oxide 2), which shows much smaller pores than for the Si-free sample (20–30 nm in diameter (b)) [298].

(#10**) coating [360] also provides a small Q_p of 92.9 kJ/mol and even smaller k_p values than $Ti_{0.40}Al_{0.55}Zr_{0.05}N$. Again, there the mixed Ti-Zr-O layer is more likely a $Zr_{0.33}Ti_{0.67}O_2$. These results suggest that the oxidation resistance of Zr-alloyed (Ti,Al)N coatings strongly depend on the nature of the mixed Ti-Zr-O layer. Here, the $Zr_{0.33}Ti_{0.67}O_2$ seems to provide a more protective behavior than $ZrTiO_4$.

The LaB_6 and $CeSi_2$ microalloyed (Ti,Al)N coatings, $Ti_{0.43}Al_{0.57}N(LaB_6)_{0.02}$ (#15) and $Ti_{0.50}Al_{0.50}N(CeSi_2)_{0.02}$ (#16), have quite large Q_p values of 442.8 and 435.6 kJ/mol, respectively. Only $Ti_{0.18}Al_{0.35}Cr_{0.47}N$ (#12) provides a larger one with 516.5 kJ/mol. Due to their high Q_p values, these coatings have larger k_p values at 950 °C although providing the lowest ones at 850 °C. Contrary, the Ta-alloyed (Ti,Al)N coatings, which are not among the best ones at 850 °C, provide smallest k_p values at 950 °C (0.05 $\mu m^2/h$ for #31) – granted by the relatively small Q_p, which is 171.6 kJ/mol for $Ti_{0.42}Al_{0.48}Ta_{0.10}N$ (#7). This compares well with the reported activation energy for oxidation of (Ti,Al)N of 187 kJ/mol [164], but for temperatures between 700 and 850 °C (200 ± 30 kJ/mol [375] at 500–800 °C, 2.2 eV (212 kJ/mol) at 750–800 °C and 4.2 eV (405 kJ/mol) at 850–900 °C [114]). At higher temperatures the oxidation of (Ti,Al)N accelerates [114], in agreement with results presented in Fig. 23. Evaluating the oxidation data for AlN bulk ceramic yields 212 kJ/mol (51 kcal/mol) [376] and 234 kJ/mol (56 kcal/mol) [377] for the initial parabolic kinetic at 900–1100 °C (TiN bulk ceramic provides 194 kJ/mol at 625–1075 °C [378]) and those of TiN-Si (14 at% Si) [39] yields 288 kJ/mol, Fig. 27a. All solely Ta-alloyed (Ti,Al)N coatings presented in Fig. 23 (#5–7, 20–24, 30–32) have k_p values within the green-shaded region of Fig. 27. The Nb and Hf alloyed (Ti,Al)N, $Ti_{0.35}Al_{0.57}Nb_{0.08}N$ (#8) and $Ti_{0.35}Al_{0.55}Hf_{0.10}N$ (#9), are also in this region, but their larger Q_p values of 201.0 and 246.8 kJ/mol, respectively, cause their change from the midfield at 850 °C to the upper bound at 950 °C.

Contrary, the solely Si-alloyed (Ti,Al)N ($Ti_{0.43}Al_{0.48}Si_{0.09}N^{arc}$, #13), which is in the midfield of the green-shaded region at 850 °C, comes closer to the lower bound at 950 °C. As highlighted in [287], the formation of a dense and protective outermost α-Al_2O_3-based scale requires a high temperature. This might be due to the bonding with SiO_2 and its glass-forming ability, which better works at

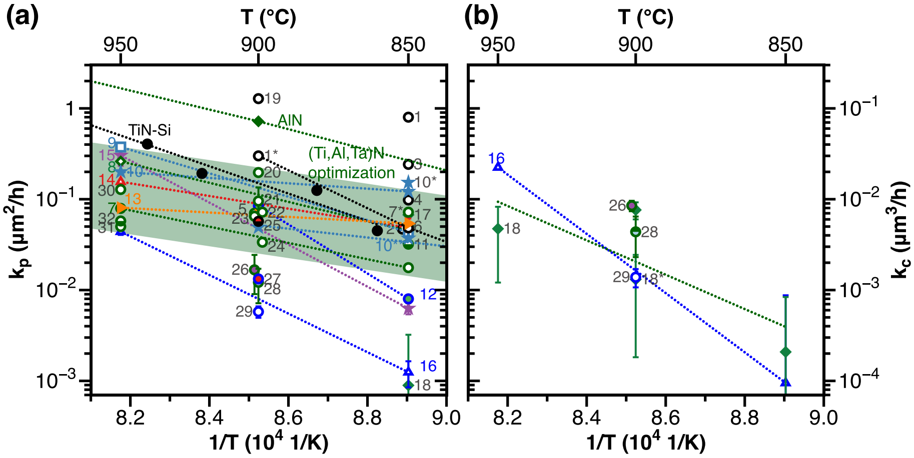

Fig. 27. (a) Arrhenius-plot of the apparent parabolic growth rates k_p for the (Ti,Al)N-based coatings presented in Fig. 23 (with the same numbering). Coatings showing a breakaway oxidation where only considered up to this point. Colored numbers refer to coatings with more than just one data point here. The data for AlN bulk ceramics [114] and TiN-Si coatings (14 at% Si) [39] are added as an additional reference. For comparison reasons, the growth rates of oxide scales on #16, 18, 26, 28, and 29 are fitted with a parabolic law (although they follow more a cubic one). Therefore, they have quite large error bars in (a). (b) Arrhenius-plot of the apparent cubic growth rates k_c for these coatings, $Ti_{0.50}Al_{0.50}N(CeSi_2)_{0.02}$ (#16 [257]), 6.4-at%-Si-alloyed $Ti_{0.21}Al_{0.20}Cr_{0.28}Nb_{0.16}Ta_{0.14}N$ (#18) and 9.8-at%-Si-alloyed $Ti_{0.21}Al_{0.20}Cr_{0.27}Nb_{0.17}Ta_{0.14}N$ (#18*) [298,362], $Ti_{0.43}Al_{0.43}Ta_{0.14}N(CeSi_2)_{0.01}(LaB_6)_{0.01}$ (#26 [262]), $Ti_{0.49}Al_{0.44}Ta_{0.07}N^{arc}/Al_{0.62}Cr_{0.38}N^{arc}$ (#28) and $Al_{0.62}Cr_{0.38}N^{arc}$ (#29) [264]. The error bar is typically smaller than the symbol size.

higher temperatures. Generally, the overview displayed in Fig. 27 shows that the protectiveness of the oxide scale formed depends on the temperature, which can alter the most promising alloying concept.

The combination of the Ta-, Si-, and RE-effect helps $Ti_{0.43}Al_{0.43}Ta_{0.14}N(CeSi_2)_{0.01}(LaB_6)_{0.01}$ (#26) to be among the best ones at 900 °C, although the chemistry of $Ti_{0.43}Al_{0.43}Ta_{0.14}N$ is not ideally and outscored by the one closer to the mentioned ideal composition $Ti_{0.3}Al_{0.6}Ta_{0.1}N$, $Ti_{0.34}Al_{0.54}Ta_{0.12}N^{arc}$ (#24). At 900 °C, only the (Al,Cr)N-based coatings, $Cr_{0.45}Al_{0.53}Y_{0.02}N$ (#27), $Ti_{0.49}Al_{0.44}Ta_{0.07}N^{arc}/Al_{0.62}Cr_{0.38}N^{arc}$ (#28), and $Al_{0.62}Cr_{0.38}N^{arc}$ (#29) provide smaller k_p values. For comparative reasons, the oxide growth rates of the coatings #16, 18, 26, 28, and 29 were fitted with a parabolic law, although they follow more a cubic one, Fig. 27b.

4. Fracture toughness

4.1. Some materials science basics

Typically, ceramic-like materials provide high strength and thermal stability but exhibit only limited fracture toughness. Fracture mechanics and especially the fracture toughness of ceramics is a very complex field in itself, for which the reader is referred to further literature such as [379–384]. We present here only some basics, which we understand as tools to increase the fracture toughness of ceramic-like coating materials. According to the Griffith criterion, the critical stress σ_c at which instable crack propagation (fatal failure) occurs can be estimated based on the liner-elastic-fracture mechanics theory, see e.g. [384–389], as

$$\sigma_c = \frac{K_c}{Y\sqrt{\pi a_c}} \tag{27}$$

K_c is the critical stress intensity factor (or fracture toughness, which is the materials resistance against instable crack propagation). Y represents a geometry factor (considering the specimen and crack geometry) and a_c is the crack length or critical failure size (like the pore size in ceramics). The critical stress intensity factor K_c (for a plain stress) can be estimated as

$$K_c = \sqrt{G_c E} \tag{28}$$

with E being the Young's modulus and G_c the energy a crack consumes. Without any plastic deformation this is often associated with 2γ, where γ is the specific surface energy, and the factor 2 belongs to the two surfaces of the crack (in other words, two opposite surfaces are created). For a plain strain situation (as in the middle of a sample), $\frac{E}{1-\nu^2}$ instead to E (for a plane stress situation and a plane specimen) needs to be used for Eq. (28), with ν being the Poisson's ratio. Generally, due to the three major loading modes of the crack-tip, three K_c values, K_{Ic}, K_{IIc}, and K_{IIIc} are classified. Let us assume a plane specimen with crack, Mode I refers to the opening or tensile mode (tensile stresses are active at the crack-tip), mode II to the shear or slide mode (shear stresses are active at the crack-tip in crack propagation direction), and mode III to the shear or tear mode (with shear stresses at the crack-tip perpendicular to the crack propagation direction) [387]. Mode I is the most demanding one and, generally, $K_{Ic} < K_{IIc}$ or K_{IIIc}. Failure occurs if the active stress at the crack-tip is above σ_c. This is schematically presented in Fig. 28a (according to Eq. (27)), which also indicates what measures can be taken (without decreasing σ) to enter the safe zone. Obviously, a reduction in a_c helps, but if that is not possible, we need to increase K_c, and, according to Eq. (28), this is possible via an increase in E or G_c.

As summarized by Ritchie [390], contributions to G_c can be divided into extrinsic and intrinsic ones. Intrinsic mechanisms (typically in front of the crack-tip like microplastic zones, additional stress-fields, cleavage fracture of microparticles) are determined by material properties and are therefore independent of component geometry and crack morphology. Extrinsic mechanisms (typically behind the crack-tip like oxide-wedging, grain-bridging, fiber-bridges, crack displacement) are strongly dependent on the formation of the crack and on the shape. They locally reduce the stress intensity at the crack-tip, so-called crack-tip shielding, and thereby increase the crack propagation resistance. In macroscopic terms, the energy absorption of both mechanisms increases the critical energy release rate G_c.

In ductile materials, mainly intrinsic mechanisms are active and used to increase toughness. These intrinsic mechanisms include pile-up of mobile dislocations with a subsequent cleavage fracture or microscopic interfacial detachment and the formation of micro-defects and their joining. This leads to the formation of a microplastic zone in front of the crack-tip. Extrinsic mechanisms can also act in an inelastic zone behind the crack-tip. This occurs primarily during thermomechanical fatigue by crack-bridging or by sliding of the crack-faces. Since the extrinsic mechanisms act in the crack-wake, i.e. behind the crack-tip, they have no influence on crack initiation. They only start to act after a crack has formed. For this reason, in materials in which extrinsic mechanisms act, the toughness (resistance to failure) increases with increasing crack length. In brittle materials (such as ceramics), mainly extrinsic mechanisms are suitable to increase toughness [390,391].

The major energy dissipation mechanisms to increase the toughness of ceramic materials are based on "*crack deflection* (1)" and "*crack shielding* (2)" – being the most effective – followed by "*contact shielding* (3)" and increasing intrinsic material properties through "*improved ductility* (4)".

Crack deflection (1) can be achieved by particles that have a higher crack resistance than the matrix or another Young's modulus. Crack deflection also occurs at the interfaces of laminates (or multilayers) in front of a propagating crack. If layers with low crack resistance are arranged perpendicular to the crack propagation, then a crack can be deflected at the interface. The stress at the two crack fronts is now significantly lower and also two new surface pairs had to be formed (needs energy) – such a scenario is schematically presented in Fig. 28b and can be extracted in hard coating materials through superlattices for example (see Ch. 4.2). The difference in Young's modulus can either attract or repel the crack. This leads to bulging of the crack or deflection of the crack in the crack plane (plane perpendicular to the applied stress) or out of the crack plane. In both cases, the crack front sees a lower stress. The splitting from mode I into mode I + II or I + III directly at the crack-tip reduces the intensity (because, $K_{Ic} < K_{IIc}$ or K_{IIIc}) [391].

As pointed out by Gabel et al. [395] on the example of a layered eutectic NiAl–Cr(Mo) in-situ composite, when in addition to crack deflection (Fig. 29a) also crack renucleation and crack bridging (Fig. 29b and c) can be activated, the fracture toughness is much higher.

There are different *mechanisms to shield* (2) a crack from the applied stress. The best known is transformation strengthening/toughening, which works for metals (e.g. steels) and ceramics (a lot is known for ZrO_2-toughened ceramics). The principle is based on the intercalation of a metastable second phase into the matrix which transforms under mechanical stress with an increase in volume (but not otherwise).

The classical example is the intercalation of some vol.% ZrO_2 in oxides or other brittle ceramics. The high temperature modification of ZrO_2 is tetragonal (t-ZrO_2) and has a much smaller specific volume than the monoclinic (m-ZrO_2) low temperature modification. By

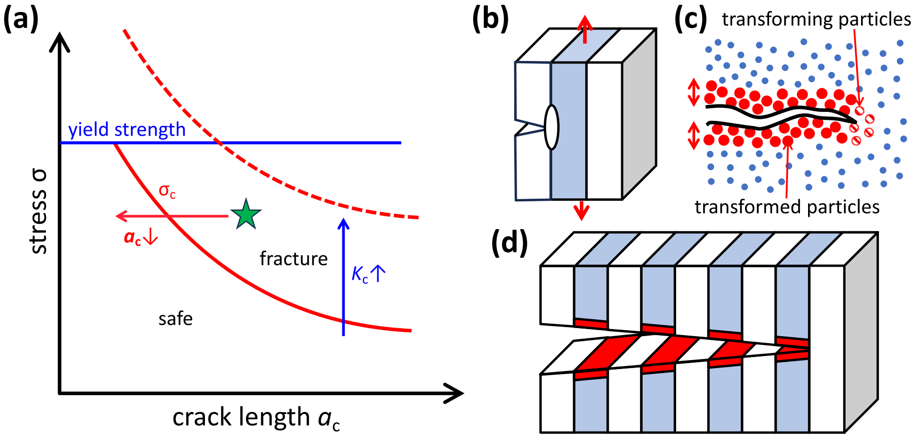

Fig. 28. (a) Schematic presentation of Eq. (27), where the green asterisk symbolizes a given loading σ at a given a_c. If the original conditions would be above σ_c (being in the fracture region), decreasing a_c or increasing K_c can change this so that for the same loading, σ is below σ_c (being in the safe region). (b) Schematic of the interaction of an approaching crack-tip and a second phase (maybe as layers perpendicular to the crack growth direction) having a different characteristic (different Young's modulus, different lattice parameter a for coherently grown layers, or lower crack resistance), adapted from [392]. (c) Schematic of transformation toughening mechanisms due to a martensitic transformation of particles with an associated volume increase (e.g. the t-ZrO_2-to-m-ZrO_2 transformation in thereby toughened ceramics, see text), adapted from [393,394]. (d) Schematic of a combination of (b) and (c), which might be accessible for multilayers or superlattices where one layer is epitaxially stabilized in its lower-volume metastable structure.

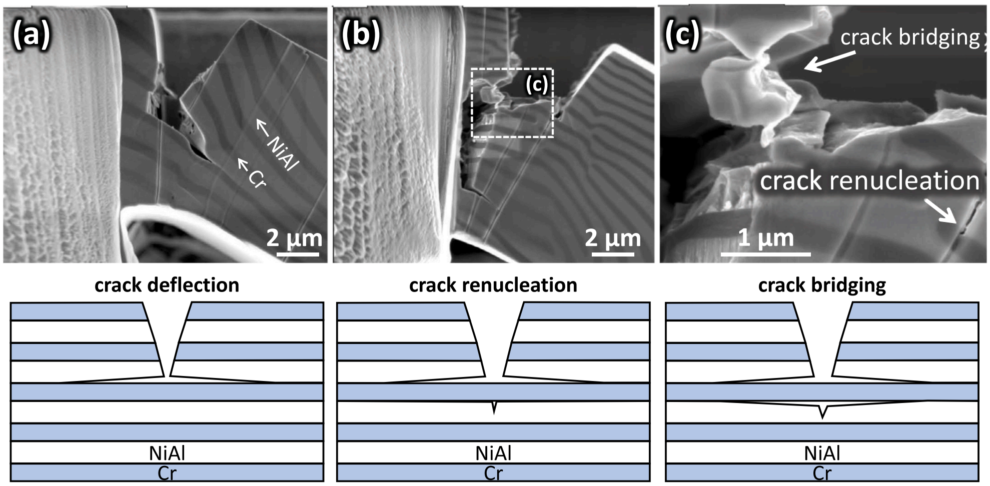

Fig. 29. SEM images of microcantilevers in the crack arresting orientation after testing, made from two 6 at% Mo-containing layered eutectic NiAl–Cr in-situ composites. (a) Sample with lowest fracture resistance, where mainly crack deflection contributes to dissipate energy, schema below. (b) Sample with highest fracture resistance, due to the joined effects of crack-deflection, −renucleation, and −bridging. (c) A higher-magnification image of the region boxed in (b). Adapted from [395].

adding other metal oxides such as MgO, Ce_2O_3, or Y_2O_3, the driving force for the transformation can be lowered, i.e. the t-ZrO_2-to-m-ZrO_2 transformation temperature is lowered. Above 2370 °C the cubic modification is preferred. An important consequence of the t-ZrO_2-to-m-ZrO_2 transformation (which could be initiated by the propagation of a crack, where the crack-wake or tensile stressed regions near the crack-tip would allow for this) and the associated increase in volume is that additional compressive stresses build up. These will influence the stress situation at the crack-tip – which is directed perpendicular to the crack propagation and thus relieves the effective tensile stresses at the crack front – and counteract further transformation of the t-ZrO_2 grains in the matrix. Such a scenario is schematically presented in Fig. 28c and d and can be extracted in hard coating materials through superlattices for example (see Ch. 4.2). Less effective than transformation strengthening/toughening is the toughness increase due to the formation of microcracks or pores in the process zone leading to a reduction of the effective energy on a crack. These could be triggered by microstructural elements that break or open respectively detach near the crack front due to the increased tensile stresses there. Possible features for such could be droplets within arc-evaporated coatings, but their size needs to be smaller than the critical size a_c.

Contact shielding (3): Everything that holds the crack together behind the crack-tip relieves the crack-tip and thus the "toughness" increases, since less stress is effective at the crack-tip. The most important mechanisms are grain bridging and fiber reinforcement. Bridging causes the crack flanks to interlock, e.g. via friction, and, thus, reduces the effective stress at the crack-tip. Through fiber reinforcement, energy is dissipated due to the deformation of the fibers (elongation and fracture) by pulling out fibers and

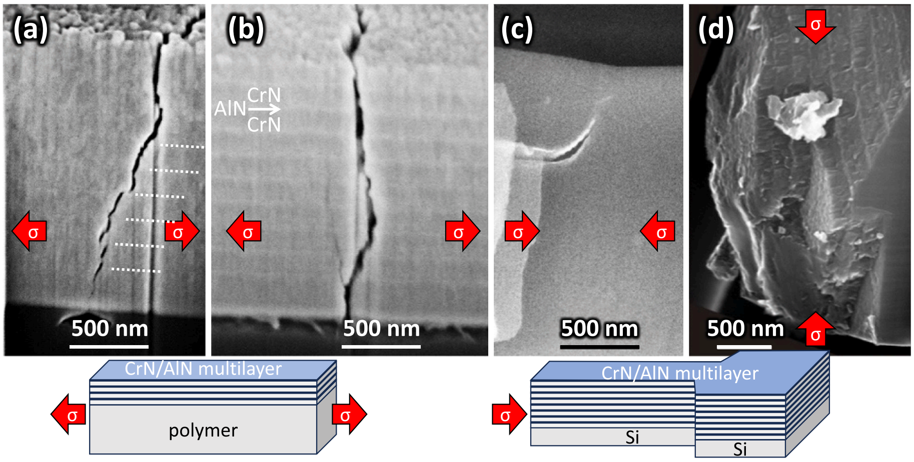

Fig. 30. (a), (b) Focus ion beam (FIB) cut through a crack introduced during straining (18 % with 0.6 mm/min) of a polymer substrate [397] that has been coated with CrN/AlN multilayers: (a) CrN and 3-nm-thin AlN layers (fcc due to coherent growth with fcc-CrN, AlN layers are marked by dashed white lines) and (b) CrN and 10-nm-thin AlN (hcp, as coherency to fcc-CrN breaks if too thick, see Ch. 4.2) [398]. (c), (d) In-situ compression test of coatings on massively thinned Si substrates (<400 nm) until failure. In (c) is the same coating as in (a) and in (d) the same as in (b) [398]. The loading (tensile or compressive) was always in-plane of the layers.

delamination from the matrix. As these are difficult to be used in hard ceramic thin film materials, we mainly concentrate on the energy dissipation mechanisms based on *crack deflection* (1), *crack shielding* (2), and *contact shielding* via bridging (3).

The impact of layers, within a hard coating, with a perpendicular arrangement to the crack propagation direction strongly depends on the nature of the layers, but also the stress field generated at their interfaces. Obviously, if one of the layer-materials is more ductile (like metals, Me, as compared to ceramic-type layers, e.g., TMN/Me, TMC/Me, or TMB_2/Me), the fracture toughness would increase with increasing metal-fraction. But this typically would be on the expense of strength [396], which we therefore will not discuss here further. However, as pointed out in [396] with the example of VC/W, the correct choice of the alternating-layer and the formation of superlattices (Ch. 4.2) allows to improve hardness and toughness. In addition to the more ductile character of one layer, the strain field generated by lattice-mismatched and/or elastic constants mismatched layers [396] influences the crack propagation.

Crack propagations due to tensile or compressive loading of CrN/AlN multilayers are captured in Fig. 30a to d.

If the AlN layers are grown coherently (thus only 2–3 nm thin) on fcc-CrN, the cracks passing through the CrN/AlN multilayers exhibit more deflection at the individual interfaces and even branching, than if the AlN layers are non-epitaxial and in their thermodynamically stable hcp structure (here, 10 nm thin). Compare Fig. 30a and b for samples that have been tensile strained respectively Fig. 30c and d for samples that have been compressed until failure. This impressively shows that the nature (or structure) of the individual layers (and the thereby associated strain fields) hugely impact the crack growth behavior. In the next chapter we will introduce the concept of epitaxial layers, termed epitaxial stabilization, and superlattices and why epitaxy maybe lost after a certain thickness of the layers.

4.2. Superlattices

First reports about superlattice (SL) structures date back to 1925, based on XRD studies of solid solutions within the systems Au–Cu and Pd–Cu [399]. Thus, they outdate the concept of crystal dislocations by Taylor [60] from 1934 or the assumption of such crystal defects (without naming them dislocations) made by Prandtl [66] in 1928. What they have in common is that Dehlinger – whom we mentioned during introducing the concept of dislocations in Ch. 2.1 for his “Verhakungen” [65] – together with Graf was also for superlattices among the first to study them and provide additional explanations [400–402]. The superlattice structure within some compositions of Au–Cu (essentially at 25, 50, but also 75 at% Cu) originate by their perfectly ordered arrangement of Au and Cu atoms within the fcc-structure (Cu is either at all corners or face centers of an fcc cell, thus for 25 or 75 at% Cu; or (0 0 1) and (0 0 2) planes alternate in being either Cu or Au, giving 50 at%). The $AuCu_3$-type (AB_3-type) is actually present in more than 75 different intermetallic systems and allows for densely packed crystals that the A-atom is only coordinated by B-atoms. The AuCu-type (AB-type) is actually tetragonally distorted in the [0 0 1] direction, along which Au (e.g. at 001-planes) and Cu (e.g. at 002-planes) monolayers alternate. Due to the distinct chemical difference of the layers (either Au or Cu), combined with atomically sharp “interfaces”, the AuCu-type provides pronounced satellite reflections during XRD investigations. Such satellite reflections arise from constructive interference of X-rays reflected from the upper and lower interfaces of the bilayer units (a bilayer period Λ denotes the combined thickness of layer A and B). The more pronounced the satellite reflexes are, the better the long-range coherent periodicity of these bilayers and the higher the quality of the SL in terms of planar and homogeneous interfaces. The smaller Λ, the further the satellite reflections deviate from their main Bragg peak. The bilayer period Λ can be calculated from XRD patterns with satellite reflections using the modified Bragg’s law:

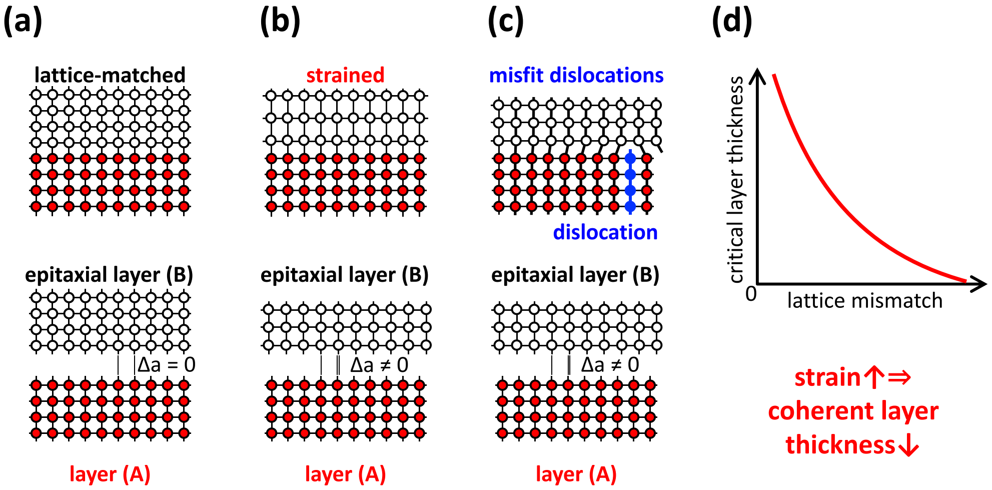

Fig. 31. Epitaxial growth of layers A and B with (a) lattice-matched layers ($\Delta a = 0$), (b) strained layers due to a lattice mismatch ($\Delta a \neq 0$, here layer B has a larger lattice parameter than layer A), (c) formation of misfit dislocations for too high misfit strains, and (d) dependence of the critical layer B thickness for an epitaxial growth on layer A with the lattice mismatch between these layers. Adapted from [406].

$$\Lambda = \pm\frac{n\lambda}{2sin\theta_n - 2sin\theta_{SL}} \tag{29}$$

with n for the order of the satellite reflection, λ the wavelength of the radiation, θ_n the diffraction angle of the corresponding (n^{th}-order) satellite reflection, and θ_{SL} for the diffraction angle of the main Bragg peak (around which satellites form). With their concept of artificially made superlattices [403] – essentially multilayered thin films, prepared by alternating two or more layers via vacuum deposition techniques – Esaki and Tsu initiated a new research-field in developing new "materials". Although their concept was motivated by the development of a one-dimensional periodic potential in monocrystalline semiconductors, this concept soon entered other research disciplines (beyond the field of semiconductors). Esaki and Tsu proposed that the one-dimensional periodic potential can be obtained by a periodic variation of the alloy composition or by a periodic variation of the doping content during an epitaxial crystal growth. In the same year (1970), Koehler proposed a composite material for a strong solid, which is similarly based on epitaxial growth of alternating layers of crystals A and B [404]. To this end, the two crystals should have the same lattice parameter but as different elastic constants as possible, and the layers should be sufficiently thin so that no dislocation generation mechanisms (such as Frank–Read sources) can operate, according to the schema presented in Fig. 31a. Koehler correctly mentions, that it is actually the difference in line energy of dislocations that matters. Dislocations would prefer to stay within the layer providing smallest line energy and to drive them into the other layer requires a very high stress. Lehoczky [405] was the first to report about the experimental verification of Koehler's attempt, using thin-layered Al–Cu and Al–Ag laminates. For example, the tensile yield strength of Al–Cu laminates (with equal Al and Cu thicknesses) increases from ≈ 140 MPa (rule of mixture for thick Al and Cu films) to ≈ 670 MPa with decreasing the layer thickness to 70 nm. With a further reduction (down to 20 nm) the tensile yield strength essentially stays at this high value. Contrary to the Hall–Petch type inverse-square-root variation with grain-size (Eq. (4)), Lehoczky observed a linear dependence of the tensile yield strength on the inverse layer thicknesses due the repulsive dislocation-image forces as described by Koehler.

In addition to this "*Koehler strengthening*" or modulus difference strengthening, superlattices or multilayers also allow for "*coherency stress strengthening*". Here, strains at coherent interfaces (for lattice mismatched materials, as schematically presented in Fig. 31b) impede the dislocation motion. They also allow for an "*epitaxial stabilization effect*", where the pseudomorphic forces of the stabilizing layer act on the surface of the other layer during nucleation and growth, causing it to crystallize in its metastable but more similar structure rather than its thermodynamically stable but different structure. Depending on the lattice mismatch and generated strain, misfit dislocations may form (Fig. 31c) and the critical layer thickness at which (partial) coherency breaks is inversely proportional to this strain, see Fig. 31d.

The coherency stresses may even result in enabling structures difficult to obtain otherwise, like the tetragonal β-Mo_2N phase, which has an ordered vacancy distribution on the N-sublattice. During growth of single-crystalline 001-oriented TiN/$MoN_{0.5}$ superlattices (Fig. 32a), the stretching of the lattice parameter a of $MoN_{0.5}$ to match that of TiN, causes a shortening of its [0 0 1] direction, promoting the formation of β-Mo_2N (having a c/a ratio of 1.96) over the fcc structured γ-Mo_2N [407], see Fig. 32b and c (corresponding to the schematic drawing presented in Fig. 31b). Both phases, β-Mo_2N and γ-Mo_2N can be imagined as an fcc NaCl (rocksalt) structure, where the metal sublattice is theoretically fully occupied and the N-sublattice is half vacant (ordered vacancies for β-Mo_2N and random

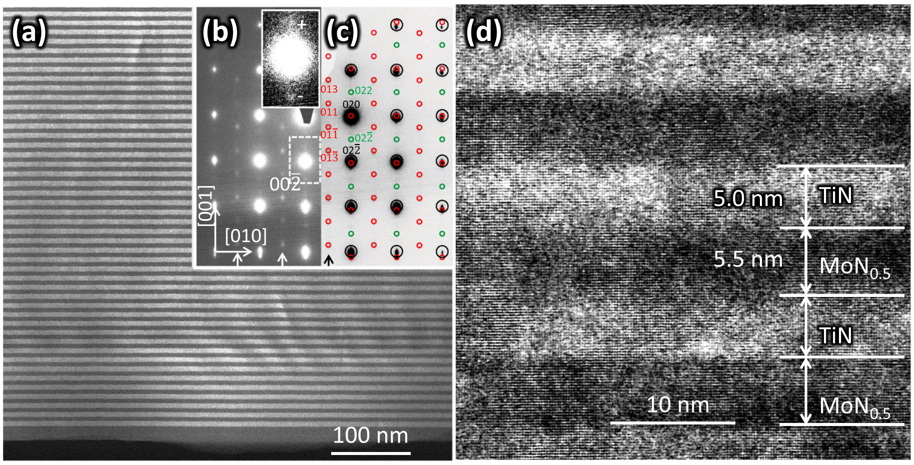

Fig. 32. Cross-sectional TEM investigations of a 001-oriented single-crystalline TiN/$MoN_{0.5}$ superlattice with $\Lambda = 9.9$ nm, grown on MgO(0 0 1). (a) STEM overview image. (b) [100] SAED pattern with most intense reflections from the fcc TiN/$MoN_{0.5}$ lattice and lower-intensity satellite reflections along [0 0 1] due to the superlattice. The latter are marked by + / − in the enlargement from the region marked by a white dashed rectangular. The other lower-intensity reflections (along lines marked with small arrows at the bottom) stem from the ordered tetragonal β-Mo_2N phase of the $MoN_{0.5}$ layers. (c) Simulated SAED pattern with reflections of fcc TiN (black circles) and β-Mo_2N (smaller red and green circles) overlaid on the inverted SAED image (the other half of (b)). (d) Lattice-resolved high-resolution TEM micrograph capturing several bilayers and showing the coherent growth of the fcc-TiN and β-Mo_2N layers. Adapted from [407]. (For interpretation of the references to colour in this figure legend, the reader is referred to the web version of this article.)

ones for γ-Mo_2N). Thus, β-Mo_2N itself has a superlattice structure, it also shows a higher Cauchy pressure (defined by the single crystal elastic constants as C_{12}–C_{44}) than γ-Mo_2N (125 vs 90 GPa). The Cauchy pressure is often treated as inherent ductility criteria (the higher the more ductile), which is introduced in Ch. 4.3. HRTEM investigations confirm the coherent growth of the TiN and $MoN_{0.5}$ layers with apparently few (misfit)dislocations, see Fig. 32d. However, this should not lead to the conclusion that such single-crystalline superlattices have low dislocation densities. Detailed investigations of single-crystalline TiN/$Cr_{0.37}Al_{0.63}N$ SLs show dislocation densities of $2.4\cdot10^{16}$ and $4.7\cdot10^{16}$ m^{-2} for bilayer periods of 2.5 and 7.3 nm, respectively [408].

A classic example for the *epitaxial stabilization effect* would be AlN, which is hcp in its thermodynamically most stable structure but also allows for a metastable fcc structure, typically for high compressive stresses. This is because fcc-AlN has an ≈ 26 % larger specific volume (volume/atom) than hcp-AlN (without external constrains) [124,125], and therefore also the critical Al content up to which $Ti_{1-x}Al_xN$ can be synthesized as single-phase fcc structured increases with increasing compressive stresses (see Ch. 2.2.3). Correspondingly, due to the epitaxial stabilization effects, AlN layers grow coherently in the fcc structure on fcc-CrN (or fcc-TiN) as long as they are only a few-nm thin, see Fig. 30, and as long as the supporting or stabilizing layer is at least as thick as the layer that should be stabilized (here AlN) [281]. Due to the higher mechanical properties and elastic constants of fcc-AlN compared to hcp-AlN, the strength of CrN/AlN superlattices is also higher when they contain AlN layers in their fcc structure. For CrN/AlN superlattices, the critical AlN layer thickness is 2–3 nm and the hardness peaks with ≈ 31.0 GPa for $\Lambda = 3$ and 5.5 nm when containing 1 and 2 nm thin AlN layers, respectively [281]. Detailed TEM studies highlight that the critical AlN layer thickness is larger on 100- and 110-oriented grains than on 111-oriented grains [409]. For TiN/AlN superlattices, the critical AlN layer thickness is 1.5 nm and highest hardness of ≈ 37.0 GPa is obtained with $\Lambda = 2.5$ nm when containing 0.9 nm thin AlN layers [410]. This nicely correlates with earlier reports about TiN/AlN, yielding 39.0 ± 6.7 GPa at $\Lambda = 2.5$ nm [411]. Due to epitaxial growth, not just metastable phases are accessible, but the interface-induced perturbation of the periodic crystal potential leads to Friedel oscillations of the charge density [412], which force the oscillatory behavior of the interplanar spacings [413]. These oscillations are more pronounced in TiN than AlN (within the TiN/AlN superlattice) because of its mobile electrons, which can redistribute as reported in [414].

In addition to these three coherent-layer-growth-induced strengthening effects, also other interface-induced strengthening effects can be active in such multilayers. These are the "*Orowan-like strengthening*" – plastic deformation by dislocation movement and bowing inside layers; thus, the mean spacing D of pinning-points retaining the dislocations for Eq. (6) would be the layer thickness – and "*Hall–Petch strengthening*" – due to a reduction in grain size of individual layers caused by the alternating layer-growth itself. Strictly, the latter is only active in polycrystalline superlattices – as obtained for example for (Ti,Al)N/(Ti,Al,Si)N multilayers, where the grain size decreases from 90 to 30 nm for a bilayer period of 7 nm [217] – and can contribute to the sometimes observed inverse-square-root dependence of hardness on the layer thicknesses ($\sim\Lambda^{-0.5}$). As mentioned above, Lehoczky [405] reported a linear dependence of the tensile yield strength on the inverse layer thicknesses ($\sim\Lambda^{-1}$) due the repulsive dislocation-image forces described by Koehler [404] and after the Chu and Barnett model [290] ΔH follows $\sim \Lambda^{-0.7}$ (Eq. (19)) for Λ beyond the peak.

Helmersson et al. [415] where the first to show that single-crystal nitride superlattices exhibit a pronounced peak-hardness when varying the bilayer period Λ. For TiN/VN (with symmetric bilayers) the microindentation hardness peaks with 5560 ± 1000 kg/mm^2 (≈ 54.5 ± 9.8 GPa) at $\Lambda = 5.2$ nm, which rapidly declines to 3950 ± 550 kg/mm^2 (≈ 38.7 ± 5.4 GPa) upon increasing Λ to 7.5 nm or to 4400 ± 830 kg/mm^2 (≈ 43.2 ± 8.1 GPa) upon decreasing Λ to 4.8 nm. A comprehensive overview on various TMN-based multilayered hard coatings is from Yashar and Sproul [416]. Based on their outstanding properties and property-combinations, such as high corrosion resistance, wear resistance, when combining the proper materials, PVD superlattices rapidly also entered industrial applications as protective coatings for machining tools and components [417–419], next to Esaki and Tsu's [403] concept for microelectronic applications. Early TEM [420] and SEM [421] investigations also show that multilayers and superlattices provide higher

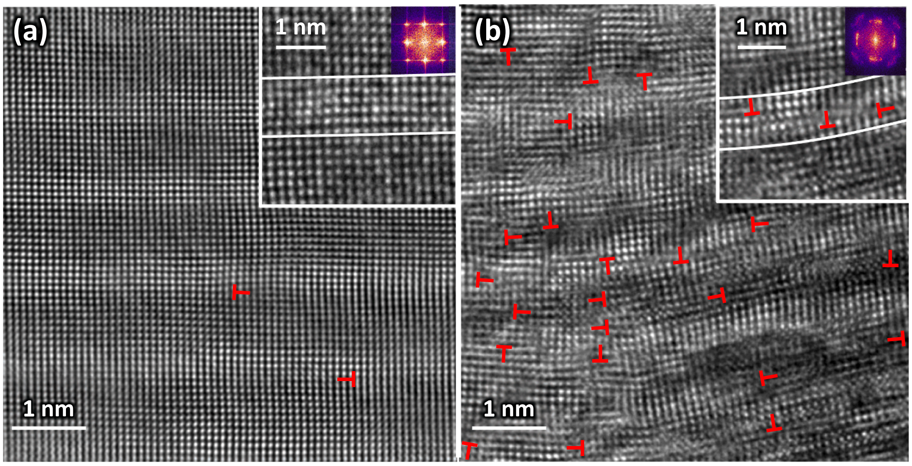

Fig. 33. Typical HRTEM images recorded from the as-deposited (a) and deformed (b) TiN/AlN superlattice (with $\Lambda = 1.7$ nm and an ≈ 0.8 nm thin AlN layer). The insets are corresponding HRTEM images of the interface structure and their fast Fourier transformation (FFT). The dislocation density in the as-deposited state is $(0.9–1.9)\cdot10^{17}$ m^{-2} and after deformation $(7.2–13.4)\cdot10^{17}$ m^{-2}. Adapted from [423].

resistance to crack propagation than their monolithically grown counterparts, even causing branching and deflection of the cracks when entering new layers, as presented in Fig. 30.

In addition to the superlattice-effect on hardness, superlattices also provide a superlattice-effect on fracture toughness, which was reported for the first time for ceramic-like hard coatings by Hahn et al. [422]. On the example of CrN/TiN superlattices, they showed that the hardness as well as the fracture toughness (Ch. 4.5) peak at a similar bilayer period of 8.6 nm and 6.2–8.6 nm, respectively. Compared with the $\Lambda = 1.8$ nm CrN/TiN superlattice (having the smallest H and K_{Ic}), an improvement by ≈ 34 % in H and ≈ 52 % in K_{Ic} was obtained. Even if the individual improvements are not outstanding, this study shows very clearly that strength and toughness – which are often counteractive – can be improved simultaneously by such superlattices. Recent detailed TEM and HRTEM studies of TiN/AlN superlattices in the as-deposited and deformed states [423] show that the interface, especially when the AlN layers grow coherently on fcc-TiN, is the source of nucleation and emission of numerous dislocations, see Fig. 33a and b, respectively. These may contribute to any microplasticity effects in front of a crack-tip, increasing the fracture toughness of the SL. Upon a heavy deformation, even intermixing of the individual layers is possible leading to the formation of a solid solution.

In addition, Koutná et al. [424] showed via *ab initio* molecular dynamics and classical molecular dynamics studies of TiN/AlN superlattices that especially when loaded in-plane (thus along [100] or [110] of 001-oriented TiN/AlN SLs) different plastic deformation mechanisms initiate in the AlN layers. These are the onset of $\{1\,1\,1\}\langle 110\rangle$ slip in AlN, which terminates at interfaces by formation of stacking faults, which themselves initiate a phase transformation of AlN from the B1 (fcc) to the cubic B3 (F $\bar{4}$ 3 m, zincblende) structure, see Fig. 34a. Similar to the fcc-AlN-to-hcp-AlN phase transformation, also here the volume increases by ≈ 26 % [428]. Furthermore, the structural changes and defect formations cause nucleation and emission of misfit-dislocations, like captured by the *ab initio* molecular dynamics snapshot of the 26 % strain TiN/AlN SL, Fig. 34a. All these processes consume energy and reduce the stress intensity at the crack-tip, which by plastic flow even may have a reduced sharpness, as indicated in Fig. 34b. This is a nice example that the mechanisms shortly introduced via Fig. 28d can be activated also in ceramic-like thin films.

Another possibility to simultaneously improve hardness and toughness is by increasing intrinsic material properties through *improved ductility* (4), allowing again for an easier mobilization of dislocation activities, which we introduce in the following chapter for ceramic-like materials.

4.3. Inherent ductility descriptors

Bonding in ceramic-like material structures involves a simultaneous contribution of covalent, ionic, and (to a lesser extent) metallic bonding to the cohesive energy. As a result, they are typically hard and relatively brittle, but exhibiting high thermal and electrical conductivity and a metallic character. They even display superconductivity like β-Mo_2N. A widely accepted empirical indicator is that more directional covalent and ionic bonding components lead to higher chemical stability and mechanical strength, while more metallic bonding contributes to better electrical conductivity, adhesion, as well as ductility. Because the delocalized electrons control the shearing resistance and, hence, plastic deformation [429]. This allows to characterize the important material feature – ductility – in terms of elastic constants. The Pugh criterion dates back to 1954 [430] and suggests that for a ductile (metallic) material the ratio between shear and bulk modulus (G/B) should be small, whereas high values imply brittle failure. He furthermore mentions that materials with small Poisson's ratio ν will be brittle, due to the correlation between G/B and ν. Although a critical value separating brittle from ductile failure is not given, the provided data suggest this to be at $G/B = 0.43$–0.56 and 0.60–0.63 or at $\nu = 0.26$–0.31 and

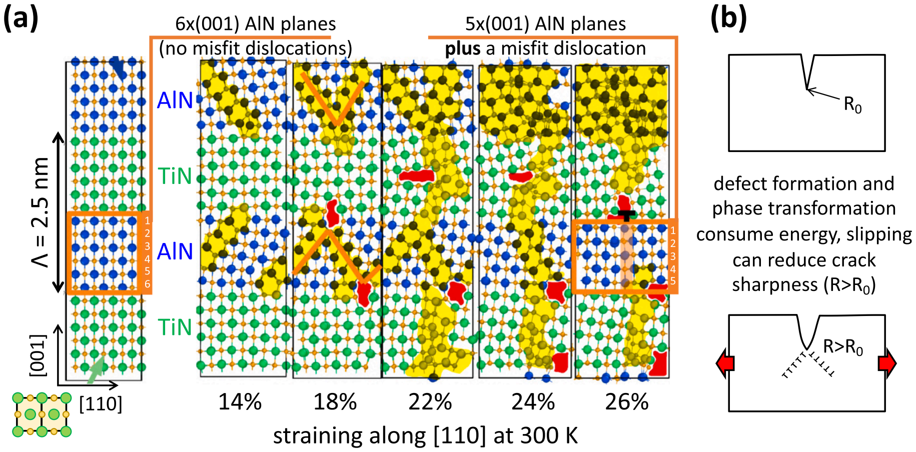

Fig. 34. (a) Ab initio molecular dynamics snapshots of AlN/TiN SLs with $\Lambda = 2.5$ nm strained in the [110] direction (parallel to interfaces) at 300 K. The yellow coloring highlights structural changes (leading to a B1-to-B3 phase transformation in AlN) and interface incoherency, while the red coloring marks initiating voids/cracks. The structural changes also lead to emission of misfit dislocations from the AlN/TiN interface, see the snapshot for 26 % straining [424]. (b) Schematic presentation of a reduced crack sharpness (from R_0 to R) due to activated slipping in front of the crack-tip, adapted from [425–427]. (For interpretation of the references to colour in this figure legend, the reader is referred to the web version of this article.)

0.25–0.27 for fcc and hcp metals, respectively. These values were also interpreted as such by Lewandowski et al. [431] and they found that bulk metallic glasses with $G/B > 0.41$–0.43 (equivalent to $\nu < 0.31$–0.32) are brittle.

Pettifor [432] described in 1992 that a change in Cauchy pressure (C_{12}–C_{44}) from negative to positive values is due to altered bonding types from directional covalent towards metallic. The improved ductility by this can be referred to the population of shear-sensitive metallic *d–d* states [433]. Shearing – which causes bending of shear-resistive non-metal–metal bonding states – increases the overlapping shear-sensitive metal–metal orbitals. This allows to activate slip systems, promoting dislocation activities, and hence plastic deformation as captured by HRTEM studies, see Fig. 33, and *ab initio* molecular dynamics, see Fig. 34. The plastic flow contributes to reduce intrinsic stresses and may even slightly blunt sharp crack-tips, such as indicated in Fig. 34b, as also proved experimentally [434]. Niu et al. [435] confirmed that many cubic-structured materials obey the general trend of ductile and brittle behavior for positive and negative Cauchy pressures, respectively. They furthermore showed by using cubic structured $Al_{12}X$ compounds (X = Cr, Mo, W, Mn, Tc, and Re) that the Pugh ratio (G/B) has a linear relation with C_{12}–C_{44}, such as shown in Fig. 35, within a material class. From such a plot, they derived that for C_{12}–C_{44} = 0 GPa the G/B ratio is 0.571, which is sometimes used to indicate the ductile-to-brittle transition (or its reciprocal 1.75). For the nitrides presented in Fig. 35 this would be at 0.59. Since Pugh did not provide a value (but he expected that the transition between ductile and brittle materials is sharp), the specification of $G/B < 0.571$ as the Pugh criterion would be not fully correct. Furthermore, Niu et al. [435] also showed that when comparing materials over a wide variety (332 compounds) there is no longer a linear relation between G/B and C_{12}–C_{44}, but there is a hyperbolic trend between G/B and $\frac{C_{12}-C_{44}}{E}$ (i.e. a Cauchy pressure normalized by the Young's modulus E), such as shown for our nitrides in the inset of Fig. 35. This as well indicates that if there is a linear relationship between G/B and C_{12}–C_{44}, the materials can be considered as belonging to the same class of materials. And only materials within the same class should be compared in terms of their Pugh ratio and Cauchy pressure, as to whether they tend to be more brittle or ductile.

This is also highlighted by Thompson and Clegg [436], because a change in crystal structure and Peierls' barrier can make a material brittle due to the difficulty of plastic flow. One of their examples is that although both the Pugh ratio and the normalized Cauchy pressure are between those of Cu and Au, the cubic Laves phase $NbCr_2$ is clearly brittle. The crystal structure of $NbCr_2$ is different from that of Cu and Au, but even for materials with the same crystal structure, a comparison based solely on elastic constants

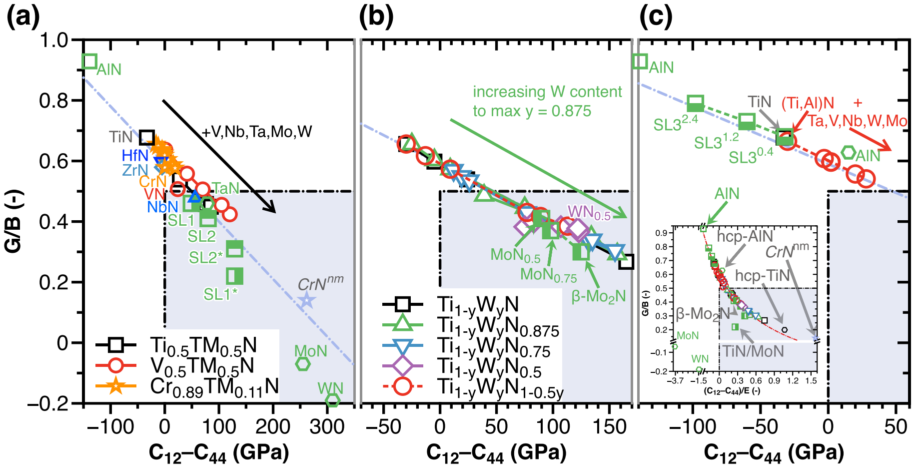

Fig. 35. Ab initio obtained relative indicators (G/B ratio and Cauchy pressure C_{12}–C_{44}) for inherent ductility of various fcc-TMN's. The dash-dotted box marks the region for G/B < 0.5 and C_{12}–C_{44} > 0 GPa. (a) Data for various TMNs are calculated from data presented in [56], TM-alloyed TiN and VN [433], and TM-alloyed (paramagnetic) CrN [447]. For comparison, also the position of non-magnetic CrN is added (CrN^{nm}) [445,446]. The data for $V_{0.5}TM_{0.5}N$ and $Cr_{0.89}TM_{0.11}N$ are shifted by +0.04 in y-direction for better differentiation. A negative G/B ratio, as obtained for MoN [407] and WN [449], indicates mechanical instability. This can be overcome by a superlattice structure with TiN for example, see the superlattice SL1* (TiN/MoN, Λ ≈ 4 nm [407]) and the SL2* (TiN/WN, Λ ≈ 4 nm [450]) data points. The corresponding superlattices with stable structured fcc-$MeN_{0.5}$ layers, SL1 (TiN/$MoN_{0.5}$) and SL2 (TiN/$WN_{0.5}$) with Λ ≈ 3 nm are not that deep in the indicated ductility region as SL1* and SL2*. The solid solutions $Ti_{0.5}Mo_{0.5}N$ [407] and $Ti_{0.5}W_{0.5}N$ [449] provide similar values. (b) Data of W-alloyed TiN_z having various vacancy-contents at the N-sublattice [449]. With increasing W, the descriptors indicate increasing ductility. But WN (as well as MoN) itself is mechanically instable in the fcc-structure, which therefore prefers the formation of fcc-$WN_{0.5}$ or hcp-WN (the latter is not considered here). By forming vacancies, the structure can be stabilized, see $MoN_{0.75}$ [407]. (c) Impact of alloying $Ti_{0.50}Al_{0.50}N$ with 25 at% (metal-fraction) Ta, V, Nb, W, and Mo (in this order G/B decreases or C_{12}–C_{44} increases) [451]. The TiN/AlN superlattices SL3 (here shown for Λ ≈ 3 nm: $SL3^{2.4}$, $SL3^{1.2}$, and $SL3^{0.4}$ with 2.4, 1.2, and 0.4 nm thin AlN layers, respectively) tend to have descriptors between those for AlN and TiN – the higher the AlN-fraction the closer to AlN and vice versa [413]. Only for very small Λ (<3 nm) this trend can be reversed. Essentially, the"best" TiN/AlN SL (SL3) only comes close to TiN [413], which itself is similar to the $Ti_{0.50}Al_{0.50}N$ solid solution [451]. For comparison, here also the position of hcp-AlN [452] is added (green hexagon), being much closer to the ductility region than fcc-AlN, while paramagnetic fcc-(Cr,Al)N [453] is further away, but can be made more ductile again through alloying with heave elements, like shown here for Ta (25 at% metal fraction, unpublished). Please note that the x-axis covers a different range in the individual panels, but the bluish dash-dotted line has the same parameters of G/B = 0.59–0.0019·(C_{12}–C_{44}). The inset of (c) shows the hyperbolic like trend of G/B with the normalized Cauchy pressure ($\frac{C_{12}-C_{44}}{E}$), according to $G/B = \frac{0.85}{1+(C_{12}-C_{44})/E} - 0.25$, for the fcc-structured nitrides presented.

(which are used to calculate the Pugh ratio, Poisson's ratio, and Cauchy pressure) can be misleading. Despite unchanged elastic constants, there could be changes in the Peierls' barrier or type of dislocations (e.g. full dislocations vs partial dislocations), which in turn leads to different plastic behavior [436]. Consequently, we use the Pugh ratio and Cauchy pressure only to indicate whether or not a material tends to be more ductile, and mark the region in a G/B-vs-C_{12}–C_{44} diagram where $G/B < 0.5$ and C_{12}–$C_{44} > 0$, based on the considerations mentioned and Refs. [437,438], see Fig. 35.

On the example of $Zr_{1-x}Al_xN$, Holec et al. [439] showed that fcc-$Zr_{1-x}Al_xN$ heavily outperform their hcp (ZnS-wurtzite structured) counterparts with these descriptors for ductility. A review about such inherent ductility criteria and toughness of hard TMN-based thin films is provided by Kindlund et al. [440], including an overview table on elastic constants and C_{12}–C_{44} and G/B.

We want to mention that for comparative reasons often the magnetic state of specific elements (like Cr) is not considered, but the elastic constants and lattice parameters of CrN hugely vary between non-magnetic and magnetic state. CrN is antiferromagnetic (next-nearest neighbor spins are antiparallel) below the Néel temperature (273–283 K) and paramagnetic above it [441,442]. While the difference in lattice parameter and elastic constants between antiferromagnetic and paramagnetic (being closest to experiments [443,444]) is little, non-magnetic CrN has much smaller lattice parameter and C_{44} values [445]. Thus, G/B and C_{12}–C_{44} is 0.14 and 202–262 GPa [445,446] for nonmagnetic CrN or 0.58 and –1 GPa [445,447] for paramagnetic CrN, respectively. Hence, either being considered ductile (nonmagnetic CrN, CrN^{nm}) or brittle (paramagnetic CrN), see their relative position in the G/B-vs-C_{12}–C_{44} plot, Fig. 35a, unfortunately, the latter is correct (without epitaxial stabilizing-effects and/or alloying). With experimental data [443,444], the G/B ratio is even 0.69 and C_{12}–C_{44} is only –61 GPa (actually very close to those of TiN in Fig. 35a). These are best captured by DFT when the strong Coulomb interaction (U) – due to strong electron correlation effects by the localized 3d electrons of chromium – is accounted for by using the generalized gradient approximation (GGA, or local density approximation, LDA) together with a Hubbard U-term [445,448].

Similarly, MoN and WN with fcc structure would have high Cauchy pressures of 255 and 310 GPa, respectively, rendering them as much more ductile compared to the other nitrides, but their negative C_{44} values (which also lead to negative G/B ratios) prove that they are mechanically not stable in fcc for an N/Me ratio of 1. However, these examples underline the importance of metastable structures, which are readily available via the formation of superlattices (especially for layer-thicknesses below 2 nm) [416] and PVD. Both these ductility criteria – similar to shear modulus and hardness – correlate with the valence electron concentration (VEC) as well, which is therefore also used as an indicator [446,447]. Essentially, when moving from IVB transition-metal-nitrides (TMN) to XIIB TMNs the criteria suggest increased ductility with increasing VEC. The close-to-linear decrease of G/B and increase of C_{12}–C_{44} (increased ductility criteria) with increasing VEC is nicely shown for (Cr,X)N (with X being IIIB, IVB, VB, and VIB elements) [447] and various TMN and TMC as well as $TMC_{1-z}N_z$ [446]. This is because the number of valence electrons per formula unit is related to shear-sensitive orbital interactions (d–t2g metal/metal). Thus, the shear modulus G and elastic constant C_{44} decrease (suggesting improved ductility) upon rising VEC. Therefore, when TMNs are alloyed with heavy elements (like V, Nb, Ta, Mo, and W, with their many electrons) both criteria come closer to the ductility region (or even enter it) [447], see Fig. 35a and c.

Because too high VECs induce a mechanical instability transition [454,455], fcc-structured nitrides should have VECs between 9 and 10, to exhibit ductility, high hardness as well as mechanical and dynamical stability. This is also the reason why fcc structured MoN and WN rather prefer a TM_2N chemistry, where half of the N-sublattice is vacant. As calculated for $Ti_{1-y}W_yN$ (Fig. 35a and b), both criteria (G/B and C_{12}–C_{44}) suggest increased ductility with increasing W content. However, this is limited by the preferred formation of an fcc-$WN_{0.5}$ structure, and therefore various N-sublattice populations (i.e. vacancy contents) have been calculated as well [449], Fig. 35b. Based on these descriptors, the solid solution fcc-$Ti_{0.5}W_{0.5}N$ and the TiN/MoN superlattice (SL1*, $\Lambda \approx 4$ nm [407]) are stable materials that are deepest in the considered ductility region of the individual nitrides compared here. Experimentally reported physical properties of TMN films vary widely and they depend largely on composition, presence and density of vacancies and voids, shape and size of grains, and film purity. But these criteria help to steer the development in the direction where materials and their structures show the desired properties. Another useful indicator for toughness, but specifically wear resistance, is the H/E ratio [456,457], which is particularly relevant for hard ceramic coatings with their variable fractions of metallic, covalent, and ionic bonds. In these materials, an increasing fraction of metallic bonds, which indicates increased ductility [56,433], typically results in a lower modulus of elasticity and consequently a higher H/E ratio. Additionally, their hardness is often more influenced by growth morphology – such as coarse, open columnar structures with low H versus dense, equiaxed structures with high H – than elasticity. Both scenarios – higher metallic bonding fractions leading to lower E values, and denser growth morphologies resulting in higher H values – generally contribute to increased toughness. However, similar to the G/B ratio, the H/E ratio should also be treated with caution, especially when comparing different classes of materials, crystal structures, or growth morphologies [449]. For example, if H in metallic materials is massively increased by strain, solid solution, and/or precipitation hardening (while their E modulus does not change as much, i.e. the H/E ratio increases), their toughness often suffers due to limited ductility. In contrast, grain-refinement strengthening, which also leads to a higher H/E ratio, does allow for an enhanced toughness. Although these ratios (G/B and H/E) could be useful indicators, experimental verification of toughness is required.

4.4. *In-situ micromechanical bending tests to obtain K_{Ic}*

There are many different attempts to quantify the fracture toughness of thin films, which can be divided into those where the film still adheres to the substrate (here symbolized with K^{f+s}) and those where the support from the substrate is removed (specifically at the regions used for testing the film). The latter are essentially based on micromechanical testing. One of the first, if not even the first for hard coatings, to develop an in-situ micromechanical testing procedure with a negligible support from the substrate were Kamiya et al. [458] and Massl et al. [459]. With FIB, microcantilevers of TiN hard coatings where machined and the substrate underneath was removed [458] or thinned to 2.2–10 μm [459]. Matoy et al. [460] further optimized the procedure and the cantilever geometries based on three-dimensional finite element (FEM) simulations, but most important they introduced the procedure of leaving small material-bridges on both sides of an already sharp FIB-machined notch, Fig. 36a and b. This guarantees the initiation of a really sharp crack-tip, Fig. 36c, as the FIB-machined notch itself would still be blunt and hence, the fracture toughness would be overestimated. Later, Brinkmann et al. [461,462] showed the importance of the correct geometry to have a valuable K_{Ic}, and as they used a representative geometry of dimensions of thickness w, breadth $b \approx w$, and length $l \approx 7 \cdot w$ (Fig. 36a), this is also used in most of our K_{Ic} investigations of hard coatings.

For such micromechanical bending tests, it is important to note that the test and the specimen geometries need to fulfil the traditional criteria associated with K_{Ic}, otherwise the obtained values are only conditional. These criteria are that the sample dimensions (w, notch depth a_0, and ligament size w–a_0) need to be larger than the plastic zone (such as that $a_0 \geq 2.5(K_{Ic}/\sigma_y)^2$ [463], with σ_y being the 0.2 % yield strength). Additionally, when wanting to compare individual K_{Ic} values, the geometries of the cantilevers should be alike. Important is further that for valuable comparison also the l/w ratios should be similar. Typically, smaller l/w ratios (due to shorter distances between loading and notch, l) lead to larger fracture toughness values.

A comparative study of various micromechanical techniques showed that each of them (single cantilever bending [460], clamped beam bending [464], double cantilever bending [465], pillar splitting [466], see Fig. 37a to d, respectively) has its merits and demerits, but essentially they all gave the same K_{Ic} of ≈ 0.8 MPa·m$^{0.5}$ for Si(1 0 0) [467]. For the other techniques, where the substrate (on which the film is deposited) is not removed, special care needs to be taken also for the still present macro-stresses. Many of them are summarized in Refs. [468,469].

These techniques, like the cube corner method [470], of course have their value especially for comparative studies and the possibility to investigate the crack geometry and crack formation by TEM or SEM [468], see Fig. 38a and b, respectively. Fig. 38a shows that directly underneath the indent there is a massive plastic deformation in the Si substrate due to the loading with 300 mN. Within the TiN–SiN$_z$ multilayer (but also in the substrate), cracks nucleated and propagated. Higher magnification micrographs demonstrate that the cracks propagate along the TiN–Si$_3$N$_4$ interfaces. Occasionally the cracks turned and propagated across a layer, but then continued along the interface again. Thus, the interlayers deflect cracks (crack deflection) and the repeated deflections consume energy, making the material tougher as described above. SEM top-view examinations of cube corner imprints (Fig. 38b) allow for a qualitative comparison of the fracture toughness and, taking into account some limitations, even a quantitative evaluation (if cracks form at the corners of the indent, following the procedure described in [470]). However, the latter should be used only with caution. Qualitative evaluation of Ti-W-N coatings using this technique [449] found that the imprint of Ti$_{0.42}$W$_{0.58}$N$_z$ (Fig. 38b) exhibits significant pile-up formations, which is a clear sign for plastic flow under the cube corner pressure load.

4.5. *Fracture toughness of TMNs and alloyed (Ti,Al)N*

TiN provides a reported hardness, Young's modulus, and K_{Ic} value in its bulk ceramic form (hot isostatic pressed, HIP) of 10.8 GPa, 353 GPa, and 3.5 MPa·m$^{0.5}$ having a relative density of 86.4 % [472], or 19.7 GPa, 430 GPa, and 4.3 MPa·m$^{0.5}$ having a relative density of 97 % [99], respectively. Bulk ceramic AlN (HIP) provides a hardness of 13.0 GPa and K_c of 3.9 MPa·m$^{0.5}$ [473] respectively $H = 17.7$ GPa and $K_c = 0.5$ MPa·m$^{0.5}$ for single-crystal AlN ceramic [212] (with $B = 220$ GPa, $E = 374$ GPa, and $G = 154$ GPa [474]). Reactive plasma sprayed TiN has a reported Vickers hardness H_v of 3.7 GPa and K_{Ic} of 4.5 MPa·m$^{0.5}$ [475]. Magnetron sputtered (Cr,Al)N exhibits an increase in H from 10.4 ± 1.8 to 25.8 ± 3.0 GPa and K_{Ic} from 1.67 to 2.02 MPa·m$^{0.5}$, as the grain size decreases from 52 to 13 nm, upon increasing the bias potential during deposition from −50 to −260 V. Thereby, also the compressive stresses increase from

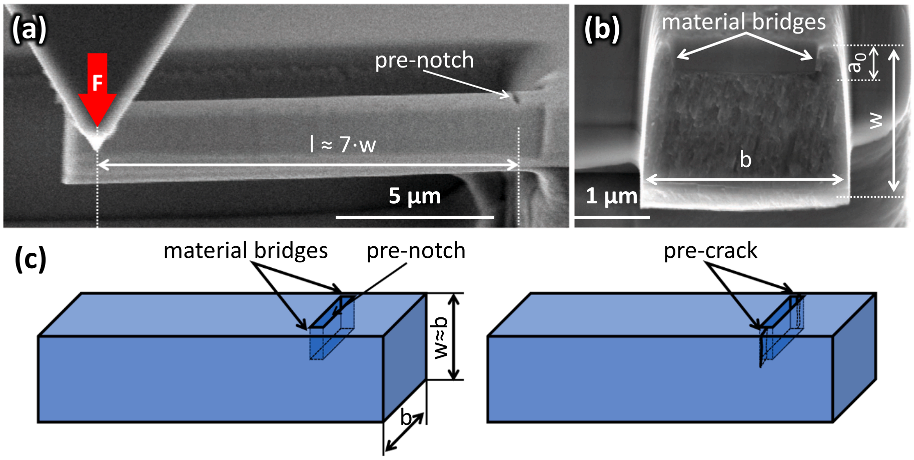

Fig. 36. SEM overview image of a micromechanical bending test on a free-standing cantilever (a), and the cross-sectional SEM image of the cantilever after fracture (b). (c) Schematic of the formation of a sharp pre-crack-tip at the material bridges left next to the FIB made notch, adapted from [460]. The notch root radius should be as small as experimentally possible.

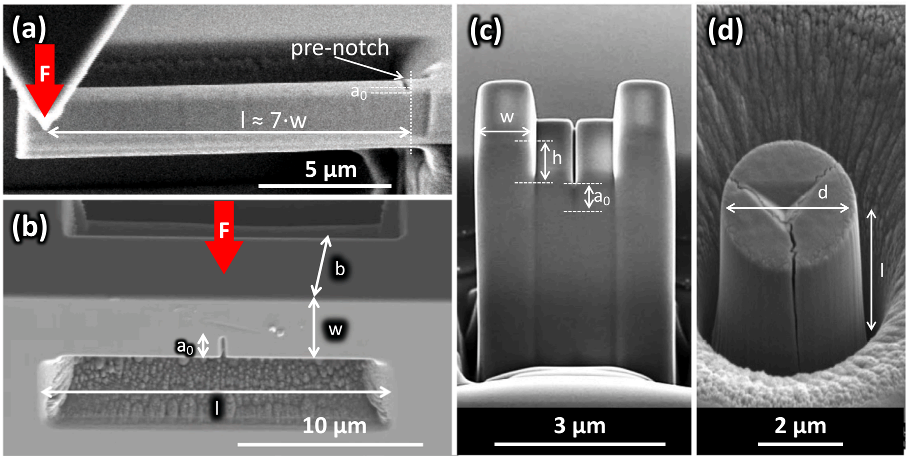

Fig. 37. Overview of four different geometries for fracture toughness testing with micromechanical techniques: (a) single cantilever bending, (b) clamped beam bending, adapted from [467], (c) double cantilever beam compression, adapted from [465], and (d) pillar splitting, adapted from [466].

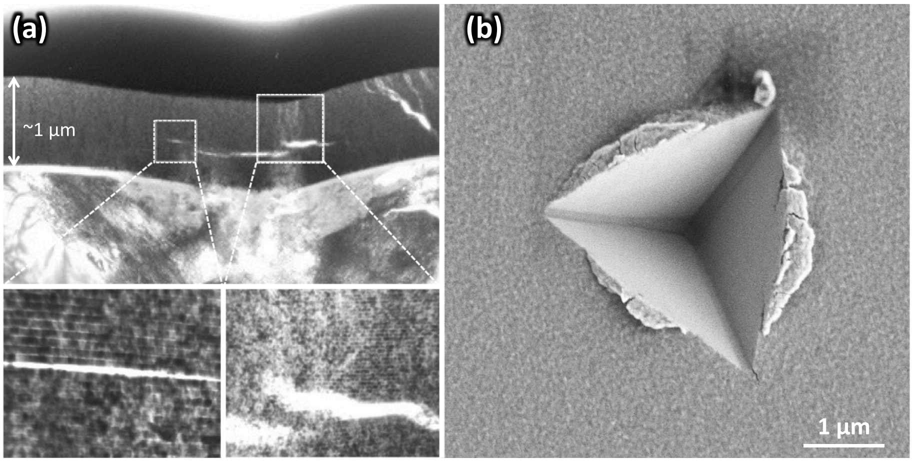

Fig. 38. (a) Cross-sectional TEM overview of a deformed TiN–SiN$_z$ multilayer with a low-cohesive-energy TiN/SiN$_z$ interface [471]. (b) Top view SEM micrograph of a cube corner indent performed with 150 mN on Ti$_{0.42}$W$_{0.58}$N$_z$ [449]. Adapted from [471,449].

−0.7 to −1.4 GPa [476]. CrN, (Cr,Ti)N, and (Cr,Al)N coatings yield H of 14.5, 13.9, and 17.7 GPa with K_{Ic} of 1.06, 2.73, and 2.70 MPa·m$^{0.5}$ [477]. Generally, the fracture of TMN hard coatings is determined by their intergranular cleavage behavior, which can already qualitatively be judged by their fracture cross-sectional appearance during SEM investigations, such as shown in Fig. 11. Such intergranular fracture appearance strongly varies with the deposition conditions, and especially bias potential applied or discharge current used during deposition. Because these parameters influence the growth morphology as well as residual stress state. Therefore, hardness, fracture toughness but also compressive residual stresses increase with increasing bias potential or increasing discharge current [478]. Different growth morphologies and preferred growth orientation are the major cause of the wide variation in K_{Ic} and H, as presented in Fig. 39a and b for TiN. Especially fracture toughness values obtained from films that are still on the substrate ($K^{\mathrm{f+s}}$) – as obtained by cube corner indentation for example – exhibit a strong dependence on the residual stresses present, see Fig. 39a.

However, there is no obvious difference between TiN, (Ti,Al)N, CrN, and (Cr,Al)N, as long as their residual stresses are comparable, but typically the CrN-based coatings exhibit lower compressive stresses if they are not even under tensile residual stress state [270]. Therefore, they exhibit lower fracture toughness values, especially if analyzed with indentation-based methods. Nevertheless, in agreement with *ab initio* obtained inherent ductility descriptors, Fig. 35, the Mo and Ta containing nitrides outscore CrN (considering the magnetic moments, because nonmagnetic CrN is not correct), TiN, (Cr,Al)N, and (Ti,Al)N for example. As mentioned above, the indentation-based evaluation of the fracture toughness requires a careful attention of their residual stresses. Therefore, micromechanical investigations of the film material (removed from the substrate) deliver more material-based (or architecture and morphology-based) data. A comparative study of TiN coatings revealed that the cube corner obtained fracture toughness overestimates that from microcantilever beams by ≈ 1 MPa·m$^{0.5}$ per 1 GPa compressive residual macrostresses [479], compare sample #1 in Fig. 39a

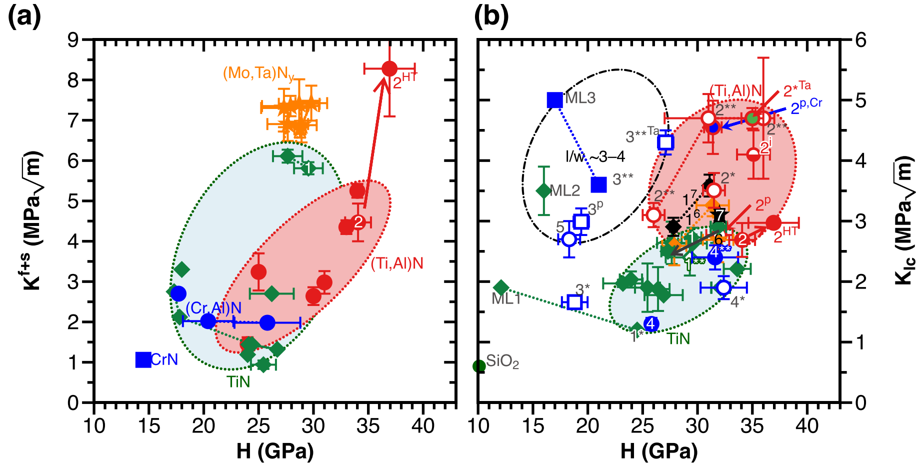

Fig. 39. Fracture toughness versus nanoindentation hardness H plots of various TMN-based films. The fracture toughness for (a) is obtained from films with substrates (K^{f+s}) and in (b) by in-situ micromechanically bending tests of film cantilevers from which the substrate was removed, according to Fig. 36a and 37a. The label numbers refer to different nitrides, with filled symbols for sputtered coatings, half-filled for HiPIMS, and empty for arc-evaporated (or also chemical vapor deposited coatings, like for (Ti,Al)N). (a) TiN [422,480–482] (#1 [81,479]), (Ti,Al)N [483] (#2, #2^{HT} (after vacuum-annealing at 900 °C) [484]), CrN [477], (Cr,Al)N [476,477], and (Mo,Ta)N$_z$ [272]. (b) TiN [81,210,407,408,422,449,450,479,485] (#1 [479]), TiN (#1*), SiO$_2$ and TiN/SiO$_2$ multilayer (ML1) with l/w ≈ 7 [486], and a similar TiN/SiO$_2$ multilayer (ML2) but with l/w ≈ 4 [487], TiN^{arc} (#1**) with l/w ≈ 3 [488], (Ti,Al)N (#2, #2^{HT} (after vacuum-annealing at 900 °C)) with l/w ≈ 6 [210], (Ti,Al)N^{arc} (#2*) and (Ti,Al,Ta)N^{arc} (#2^{*Ta}) [489], (Ti,Al)N^{arc} (#2^{P}) and (Ti,Al,Cr)N^{arc} (#2^{P,Cr}) [490] with a micro-pillar splitting test according to Fig. 37d, (Ti,Al)N^{HiPIMS} (2^{i}) with l/w ≈ 6 [491] (K$_{Ic}$ from [491] and H from [492]), (Ti,Al)N^{CVD} (2**) with l/w ≈ 5 [493], CrN (#3 [422]), CrN^{arc} (#3* [494]) with a double cantilever beam compression test according to Fig. 37c, CrN^{arc} (#3^{P} [490]) with a micro-pillar splitting test, CrN (#3**) and CrN/Cr multilayer (ML3) with l/w ≈ 3 [486], $Cr_{0.74}Ta_{0.26}N$ (3^{**Ta}) with l/w ≈ 3 [495], (Cr,Al)N (#4 [408]), (Cr,Al)N^{arc} (#4* [494]) with a double cantilever beam compression test, (Cr,Al)N (#4**) with l/w ≈ 3 [496]), hcp-structured (Al,Cr)N^{arc} (#5) with l/w ≈ 4 [497], MoN$_z$ (#6) and (Ti,Mo)N$_z$ (#1^{6}) [407], WN$_z$ (#7 [450]), and (Ti,W)N$_z$ (#1^{7} [449]). The l/w ratio of the cantilevers from samples (#1, 2*, 2^{*Ta}, 3, 4, 6, 7, 1^{6}, 1^{7}) was always ≥ 7. The black dash-dotted ellipse encloses K$_{Ic}$ data-points obtained from microcantilevers with l/w ≈ 3–4, the shaded green dotted and the shaded red dotted ellipses mark the regions of TiN and (Ti,Al)N coatings. The arrows in (a) and (b) indicate the change due to vacuum annealing at 900 °C for (Ti,Al)N [210,484] and at 500 °C for TiN [485]. (For interpretation of the references to colour in this figure legend, the reader is referred to the web version of this article.)

and b.

The massive change in compressive residual stresses (from −3.9 ± 0.3 to −6.2 ± 0.3 GPa) within (Ti,Al)N upon vacuum-annealing at 900 °C is also the major source of the pronounced increase of the indentation-obtained fracture toughness from 4.5 ± 0.5 to 8.3 ± 1.2 MPa·m$^{0.5}$ (combined with an increase in H from 34.1 ± 1.2 to 36.9 ± 2.3 GPa) [210]. The annealing-induced origin of this change stems from the decomposition of the fcc-(Ti,Al)N solid solution towards their stable constituents fcc-TiN and hcp-AlN via Ti-rich and Al-rich fcc-structured domains, as discussed above (Ch. 2.2.4, Figs. 5 and 9). As noted, the martensitic-like transformation of fcc-AlN to hcp-AlN would lead to a huge volume increase of ≈ 26 % without external constrains [124,125], this leads to the increase in residual stresses [127] (which would only be released during progressive annealing treatments due to stimulated plastic deformation of the particle and matrix, for which shearing is needed). The change in K_{Ic}, as obtained from micromechanical bending tests (details next paragraph), due to this is less pronounced, because there the massive compressive stresses are relieved due to the removal of the substrate (but still K_{Ic} increases from 2.7 ± 0.3 to 3.0 ± 0.2 MPa·m$^{0.5}$, cf. Fig. 39a and b).

Using the example of TiN – which was among the first PVD hard coatings to be tested for fracture toughness by micromechanical investigations, as mentioned above – Massl et al. [459] showed that the fracture toughness values obtained by this method were essentially due to the material-related properties and not influenced by high compressive stresses. This outcome was obtained by analyzing the fracture toughness values of the same TiN specimen (with a homogeneously distributed compressive stress state of –1.5 GPa) while its Si substrate was thinned to thicknesses between 2 to 10 μm, which leaves the TiN coating with different residual stress distributions in the microbeams. This essentially resembles a situation where residual stresses are externally applied, due to the fixture with a substrate. However, if the deposition process itself leaves the individual coatings with different residual stresses (on the same substrates), the fracture toughness values differ for the same kind of coating material, because their intergranular cleavage differs. Although macrostresses will be relieved when removing the substrate for the in-situ micromechanical investigations, their growth-induced origin (thus, without the effect induced by the differential thermal expansion coefficient between film and substrate) remains (e.g. growth-induced defects). Due to this, the fracture toughness of TiN varies between 1.2 MPa·m$^{0.5}$ [486] (grown at 200 °C and exhibiting a pronounced V-shaped open-columnar growth morphology) and 2.9 ± 0.1 MPa·m$^{0.5}$ [485] (grown at 380 °C and exhibiting a dense growth morphology), see Fig. 39b. When vacuum-annealing the latter TiN sample at 500 °C for 2 h, the residual stresses recover from –1.12 to –0.88 GPa (room-temperature values). This reduction by 0.25 GPa is due to structural recovery effects where growth-induced defects anneal-out or re-structure to lower-energy sites (resembling the classical recovery effects of materials), which causes the hardness to decrease from 31.9 ± 0.7 to 27.3 ± 0.6 GPa and the fracture toughness from 2.9 ± 0.1 to 2.5 ± 0.1 MPa·m$^{0.5}$ [485], indicated in Fig. 39b with a grey arrow.

An architectural design of TiN (#1*) through a multilayer-arrangement with SiO_2 (ML1 consisting of 35-nm-thin SiO_2 and 115-nm-thin TiN layers) allows to increase K_{Ic} from 1.2 to 1.9 MPa·m$^{0.5}$, see Fig. 39b, through introducing low-cohesive energy interfaces enabling crack-deflection as indicated also in Fig. 38a for a weak TiN–Si_3N_4 interface. Unfortunately, thereby also the hardness decreases from 24.5 to 12.1 GPa [486]. A furthermore modification of this architecture (20-nm-thin SiO_2 and 250-nm-thin TiN, which are additionally zig-zag tilted) allows to regain some hardness (16 GPa) and might further improve K_{Ic} (as suggested by Fig. 39b, ML2), but unfortunately this sample was tested with an l/w ratio of only ≈ 4 (of the cantilever-beam, Fig. 36a) [487]. When comparing thereby obtained data, the l/w ratio should be the same and preferably ≥ 7 [461,462]. Similarly, the K_{Ic} data for arc-evaporated TiN (1^{**}), CrN (3^{**}), CrN/Cr multilayer (ML3), $Cr_{0.74}Ta_{0.26}N$ (3^{**Ta}) and hcp-structured (Al,Cr)N^{arc} (#5) should be treated with caution, as these are obtained from beams with l/w only ≈ 3 [486,488,495] respectively ≈ 4 [497]. However, they do show the potential of a multilayer arrangement, where with additional repeated introduction of soft layers (SiO_2 for TiN respectively Cr for CrN) especially the fracture toughness can be improved due to additional energy consumption by for example crack deflection processes – unfortunately on the expense of hardness. K_{Ic} values of sputtered and arc-evaporated CrN are actually ≈ 1.5 MPa·m$^{0.5}$ as confirmed by two independent techniques (micro cantilever beam with $l/w \approx 7$ [422] and double cantilever beam compression test [494]), see samples 3 and 3* in Fig. 39b, respectively. With a slight advantage for the arc-evaporated coating, which typically also exhibits a more dense and compact growth morphology, see the growth-morphology-comparison of sputtered and arc-evaporated (Ti,Al)N in Fig. 11a and b, respectively. A corresponding outcome is obtained for (Ti,Al)N (2 and 2*) and (Cr,Al)N (4 and 4*). For example, the arc-evaporated (Ti,Al)N surpasses the sputtered one by 0.8 MPa·m$^{0.5}$ (3.5 ± 0.3 vs 2.7 ± 0.3 MPa·m$^{0.5}$). Unfortunately, the microcantilevers for the CVD (Ti,AlN) coatings (2^{**}) had an l/w of only ≈ 5 [493], which does not allow for a direct comparison. However, they show the potential of a hierarchical microstructure to dissipate and consume the energy of crack growth, allowing to increase K_{Ic} from 3.1 ± 0.2 to 4.7 ± 0.4 MPa·m$^{0.5}$. Similarly, the structural modifications of fcc-(Ti,Al)N upon annealing, where Al-rich and Ti-rich small fcc-structured domains formed (Ch. 2.2.4), are responsible for the increase in K_{Ic} upon annealing, cf. Fig. 39b. These materials also provide the potential of phase-transformation-induced toughening effects (due to the formation of hcp-AlN), as illustrated in Fig. 28c and 34.

In addition to the impact of multilayer and hierarchical structures, Fig. 39b shows the effectiveness of alloying CrN, TiN, or (Ti,Al)N with Mo, W, or Ta, which would bring their inherent ductility descriptors close-to or even into the ductility region, see Fig. 35. This is highlighted here with $Ti_{0.5}Mo_{0.5}N_{0.77}$ ($\#1^6$, 3.3 ± 0.2 MPa·m$^{0.5}$) and $Ti_{0.42}W_{0.58}N_z$ ($\#1^7$, 3.6 ± 0.2 MPa·m$^{0.5}$), which even outscore $MoN_{0.5}$ (#6, 2.8 ± 0.2 MPa·m$^{0.5}$) and WN_z (#7, 3.1 ± 0.1 MPa·m$^{0.5}$), because the solution with TiN allows their crystallization with single-phase fcc combined with a high nitrogen content. As mentioned above, MoN_z as well as WN_z would prefer crystallization with hcp for N/Me ratio (z) close to 1. However, DFT suggests that fcc-WN_1 is more ductile than fcc-$WN_{0.5}$ (which would be the preferred chemistry for fcc; similarly fcc-MoN_1 is more ductile than fcc-$MoN_{0.75}$), cf. Fig. 35a and b. Tantalum is not only capable of significantly increasing hardness and especially thermomechanical properties as well as oxidation resistance of (Ti,Al)N (as shown in the previous chapters), but Ta is also able to improve the fracture toughness – from 3.5 ± 0.3 to 4.7 ± 0.2 MPa·m$^{0.5}$ for arc-evaporated coatings [489], as indicated in Fig. 39b. Important to highlight is that these alloying concepts (with Mo, W, or Ta) allow to increase both, K_{Ic} and H.

The other important concept to improve K_{Ic} and H simultaneously is nanostructuring, as exemplarily shown in Fig. 40 for Si-alloyed TiN (#2, $\#2^+$), Si-alloyed (Ti,Al)N ($\#1^{**}$), and Si-alloyed (Cr,Al)N (#4 and 4^{**}), as well as various superlattice coatings, e.g. TiN/CrN (SL1, SL1$^+$, SL1*), TiN/MoN (SL2), TiN/WN (SL3), MoN/TaN (SL4), and TiN/(Cr,Al)N (SL5). The K_{Ic} values of these superlattices can be fitted proportionally to $\Lambda^{-0.5}$ for Λ beyond the peak, similar to the predicted increase in fracture strength of laminar composites made of layers with very different elastic moduli [498]. The TiN/(Cr,Al)N (SL5) is a modulus-matched superlattice, which does exhibit a superlattice-effect for H but not for K_{Ic}, cf. Fig. 40a and b, respectively.

Alloying Si to TiN improves its hardness (Fig. 40a), oxidation resistance (Fig. 27), and fracture toughness (Fig. 40b). Especially H and K_{Ic} peak at a certain Si content (often in the range 5–10 at%, not normalized to Ti) by forming a nanocomposite, as long as the SiN_z boundary phase is not too thick and a high-cohesive-energy interface is present (as discussed above when presenting the strengthening effects, Fig. 13b). The Ti-Si-N nanocomposites presented in Fig. 40 (#2) have a H-peak of 33.7 ± 0.9 GPa at 10.5 at% Si and a K_{Ic}-peak of 3.0 ± 0.2 MPa·m$^{0.5}$ at 8.5 at% Si [499]. Corresponding to TiN, improving the deposition conditions (especially with respect to plasma parameters and deposition temperature) their growth morphology can further be improved leading to H of 37.6 ± 1.5 GPa and K_{Ic} of 4.5 ± 0.6 MPa·m$^{0.5}$ at 8.5 at% Si, see data point $\#2^+$ in Fig. 40. This nanocomposite essentially is composed of 10–20 nm sized TiN crystals encapsulated by an ≈ 1 nm-thin SiN_z tissue phase [500]. The formation of a sharp and high-cohesive energy interface and essentially flaw-free TiN nanocrystals is crucial, as such structures require a much higher stress to induce and propagate cracks [504]. This is correspondingly valid also for (Ti,Al)N and (Cr,Al)N, samples $\#1^{**}$, 4 and 4^{**} in Fig. 40.

With the help of CrN/TiN superlattice coatings (SL1), Hahn et al. [422] were the first to show that in addition to the well-known superlattice-effect on hardness (partly presented in Fig. 13b) there is also a superlattice-effect on fracture toughness, as already mentioned. Both peak at a comparable modulation period Λ of 6–9 nm (Fig. 40a and b). Again, improving their deposition conditions (SL1$^+$) and especially by developing epitaxial layers (on MgO(1 0 0), SL1*) can further improve their H and K_{Ic}, peaking with 32.9 ± 1.0 GPa at $\Lambda = 4.7$ nm and 2.7 ± 0.2 MPa·m$^{0.5}$ at $\Lambda = 7.6$ nm [502]. These data are clearly outperformed (especially for K_{Ic}) by the TiN/MoN superlattice (SL2), with a hardness peak of 34.8 ± 1.6 GPa and a K_{Ic} peak of 4.1 ± 0.2 MPa·m$^{0.5}$, both at $\Lambda = 9.9$ nm, and the TiN/WN superlattice (SL3) – with peak-values of 36.7 ± 0.8 GPa (Λ = 8.1 nm) and 4.6 ± 0.2 MPa·m$^{0.5}$ (Λ = 10.2 nm). Out of these superlattice coatings, which show a clear K_{Ic}-vs-Λ peak (corresponding to that of H-vs-Λ), the TiN/WN (SL3) also exhibits a high K_{Ic} value of 3.9 ± 0.1 MPa·m$^{0.5}$ (and H of 33.5 ± 0.9 GPa) for the smallest bilayer period of $\Lambda = 2.8$ nm, Fig. 40b. An explanation for this alleged "outlier" can be obtained from DFT data (Fig. 35a), suggesting that TiN/WN is more ductile than TiN/$WN_{0.5}$. The fcc-structure

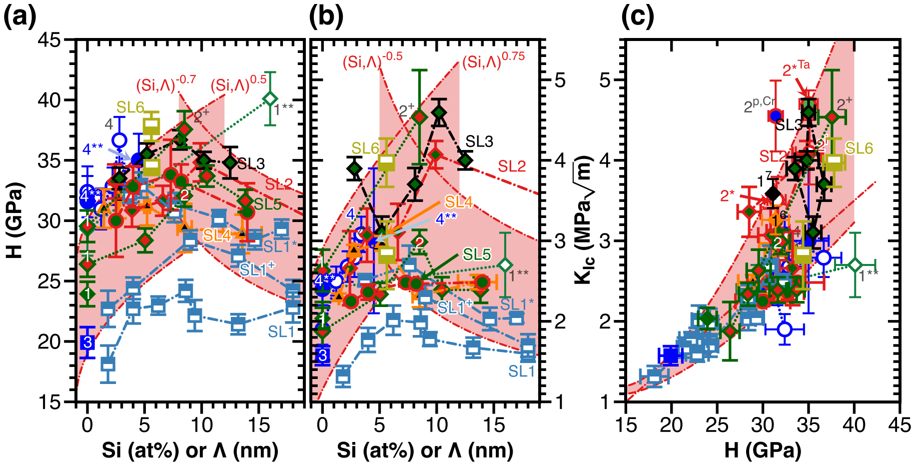

Fig. 40. (a) Nanoindentation hardness H and (b) fracture toughness K_{Ic} (by in-situ micromechanical bending tests) of Si-alloyed TiN (#2 [499], #2$^+$ [500]), arc-evaporated Si-alloyed (Ti,Al)N (#1** with l/w ≈ 3 [488]), Si-alloyed (Cr,Al)N (#4, with a double cantilever beam compression test [494], #4** with l/w ≈ 3 [496]), and various superlattice (SL) coatings with different bilayer periods Λ. SL1 (TiN/CrN [422]), SL1$^+$ (TiN/CrN [501]), SL1* (epitaxial TiN/CrN [502]), SL2 (TiN/MoN [407]), SL3 (TiN/WN [450]), SL4 (MoN/TaN [503]), SL5 (TiN/(Cr,Al)N [408]), SL6 (TiN/TaN and B-doped TiN/TaN, unpublished own data). For comparison, data for CrN (#3 [422]) and TiN (#1 [81,422,479,500]) are also added. The latter with a wide spread in H and K_{Ic} (see Fig. 39b) due to their different growth morphologies. If the Si content was normalized with the metals (to have Me + Si = 100 %), it was divided by 2 for the comparative plots. The red-shaded regions are bordered by fits proportional to $\sqrt{x}$ and $x^{-0.7}$ for x below and beyond the hardness peak according to the discussions when presenting Fig. 13, or proportional to $x^{0.75}$ and $x^{-0.5}$ for x below and beyond the K_{Ic} peak (x being the Si content or Λ). (c) K_{Ic} versus H plot of these coatings presented in (a) and (b) with the reference of arc-evaporated (Ti,Al)N (#2*), its Ta-alloyed variant (2^{*Ta}) [489], (Ti,Al,Cr)N^{arc} (#2^{p,Cr}) [490] with a micro-pillar splitting test, (Ti,Al)N^{HiPIMS} (2^{i}) [491], and the solid solutions $Ti_{0.5}Mo_{0.5}N_{0.77}$ (#1^6) [407] and $Ti_{0.42}W_{0.58}N_z$ (#1^7) [449] from Fig. 39b. The l/w ratio of the cantilevers from samples (#1, 2, 2$^+$, 2*, 2^{*Ta}, 3, 5, SL1, SL1$^+$, SL1*, SL2, SL3, SL4, SL5) was always ≥ 7. The red-shaded region is bordered by fits proportional to $H^{1.5}$ (upper bound: $K_{Ic} = 1.2 + \frac{1}{30}(H-15)^{1.55}$; lower bound: $K_{Ic} = 1.1 + \frac{1}{50}(H-15)^{1.45}$) and the red dash-dotted line, which extends slightly beyond this shaded region, is a linear fit through all data points (with $K_{Ic} = 0.1H - 0.5$). (For interpretation of the references to colour in this figure legend, the reader is referred to the web version of this article.)

of WN_z (which would prefer $y = 0.5$) with a high N-content can be stabilized through the epitaxial growth with TiN. Thus, the $\Lambda = 2.8$ nm TiN/WN superlattice might have a higher N content in their WN_z layers than those with a larger bilayer period, which are more likely TiN/$WN_{0.5}$ [502]. Correspondingly, the solid solution fcc-$Ti_{0.5}Mo_{0.5}N_{0.77}$ exhibits a higher K_{Ic} value than fcc-$Ti_{0.52}Mo_{0.48}N_{0.68}$ (3.3 ± 0.2 vs 2.6 ± 0.3 MPa·m$^{0.5}$) [407]. In addition to these intentionally designed superlattice coatings, a corresponding lattice and modulus mismatch due to chemical modulations along the growth direction may also originate from the deposition process itself. For example, an arc-evaporated (Ti,Al)N prepared in an industrial-sized machine with the help of a Ti, $Al_{0.67}Ti_{0.33}$, and Al target is composed of an alternating package of nm-thin TiN, $Al_{0.67}Ti_{0.33}N$, $Al_{0.67}Ti_{0.33}N$, and AlN layers [490]. Correspondingly, the (Ti,Al,Cr)N is composed of an alternating package of nm-thin TiN, $Al_{0.7}Cr_{0.3}N$, CrN, and AlN layers, which might explain their very high fracture toughness in combination to high hardness (#2^{p,Cr} in Fig. 39b).

In addition, in some PVD coatings and architectures nano-twins and stacking faults are present [409,505–507], which also have a high potential to improve both H and K_{Ic} – we have discussed this in more detail in Chs. 2.1 and 4.5 – as has been achieved for bulk metallic materials [508,509]. This may partly explain why the TiN/TaN superlattice (SL6 in Fig. 40) – prepared with a bilayer period of $\Lambda = 5.4$ nm and not yet optimized for its peak value – already demonstrates and outstanding combination of hardness H and fracture toughness K_{Ic} for such a small Λ. As Fig. 40 suggests, the peak values of H and K_{Ic} occur around $\Lambda \approx 8$–9 nm. Enhancing the interfaces between TiN and TaN layers with boron (the B-doped TiN/TaN SL6 has a total B content of 0.1 at% as confirmed by elastic recoil detection analysis) leads to even higher H and K_{Ic} values. Twinning-induced plasticity [510,511] has been little researched for hard ceramic-type coating materials such as transition metal nitrides, carbides, and borides, but deserves much more attention.

The combination of the data presented in Fig. 40a and b allowed to draw the K_{Ic}-vs-H plot shown in Fig. 40c. This nicely highlights the simultaneous improvement in K_{Ic} and H through the nanostructural design by Si-alloying and superlattices. Especially the well-defined superlattices TiN/MoN (SL2) and TiN/WN (SL3), solid solutions (Ti,Mo)N_z (#1^6) and (Ti,W)N_z (#1^7) and (Ti,Al,Ta)N (#2^{*Ta}), as well as the well-defined TiN/SiN_z nanocomposite (#2$^+$) noticeably deviate towards higher K_{Ic} values from the majority of the specimens (indicated by the red dash-dotted linear fit, following $K_{Ic} = 0.1 \cdot H$-0.5). The combination of several effects allows for an above-average consumption of cracking energy. These effects are for example increased ductility (through combination or alloying with Mo, W, or Ta, Fig. 35), stabilized crystal structure, alternating strain fields, and increased emission of dislocations at interfaces (through superlattices), and a nanostructure (through nanocomposites with high cohesive energy interfaces), which have been discussed above. The data suggest that especially the latter effects are responsible for the superlattices TiN/WN as well as TiN/MoN outperforming their solid solutions $Ti_{1-x}W_xN_z$ and $Ti_{1-x}Mo_xN_z$ in terms of hardness and fracture toughness, although their Pugh ratios and Cauchy pressures are similar. Coating developments resulting in data points outside the shaded region of Fig. 40c favor either fracture toughness (when above the upper bound) or hardness (when below the lower bound), compare also with Fig. 39b.

5. Summary and outlook

The $Ti_{1-x}Al_xN$ coating system, which is used in a wide range of industrial applications, allows the use of all four classical strengthening mechanisms (strain hardening, solid solution strengthening, fine grain strengthening, and particle strengthening). Strain hardening is based on a very high point defect density and dislocation density, which may well be 10^{17} m^{-2} due to the used PVD process. Solid solution strengthening is based on the formation of single-phase supersaturated fcc-$Ti_{1-x}Al_xN$ solid solutions, which can be realized in the way (with up to 70 or even 90 at% Al on the metal sublattice) only by vapor deposition. Similarly, fine grain strengthening is process-related, with grain sizes well below 100 nm being achieved. This can further be reduced (down to a few nm) by alloying with grain boundary active elements, like Si and B. The strongly Al supersaturated fcc-$Ti_{1-x}Al_xN$ solid solutions also allow the use of the fourth strengthening mechanism, namely particle strengthening.

The $Ti_{1-x}Al_xN$ hard coatings used in the processing industry consistently have Al contents of 50 or 66 at% (of the metal sublattice). Based on their *G–x* curve, such fcc-$Ti_{1-x}Al_xN$ solid solutions are actually chemically unstable, but the very limited kinetics in the PVD growth process of these hard coatings still enables their production. If these materials are used at elevated temperatures, e.g. temperatures of 1000 °C are easily possible in the machining process of metals at the cutting edge, the increased solid-state diffusion causes spinodal decomposition of these supersaturated solid solutions towards the formation of fcc-TiN and fcc-AlN. This process causes the formation of coherent fcc-structured domains, which are effective obstacles for the dislocation motion and thus counteract the generally observed hardness-decline by recovery processes. The spinodal decomposition allows a homogeneous and fine distribution of the formed domains, maximizing the associated hardness gain.

A further temperature increase finally leads to the phase transformation of fcc-AlN regions to their thermodynamically stable modification, i.e. hcp-AlN. Such a transformation typically occurs by shearing and resembles a martensitic-like transformation, which can only take place if the matrix also yields to deformation, e.g. by plastic deformation, which is particularly facilitated at higher temperatures. The associated volume increase of about 26 %, without external constraints, can even lead to cracking of the layer material or its spallation from the substrate, especially if shearing is limited. Density functional theory and corresponding experiments have shown that the alloying element Ta in particular has a very positive effect on the mechanical properties (hardness, fracture toughness, and thermomechanical properties) as well as oxidation resistance. Tantalum increases the cohesive energy and effectively slows down the thermally induced phase transformation of the forming Al-rich fcc-structured domains into hcp-AlN. This is accompanied not only by higher hardness values in the as-deposited state, but also by improved thermomechanical properties, whereby $Ti_{0.42}Al_{0.48}Ta_{0.10}N$ still exhibits a hardness of 42.0 ± 2.4 GPa even after annealing at 1100 °C. The fracture toughness of already morphologically optimized $Ti_{0.54}Al_{0.46}N$ hard coatings (K_{Ic} = 3.5 ± 0.2 MPa·$m^{0.5}$) could also be improved by alloying with Ta, as shown for $Ti_{0.44}Al_{0.41}Ta_{0.15}N$ exhibiting 4.7 ± 0.2 MPa·$m^{0.5}$.

The oxidation resistance of the Ta-alloyed $Ti_{1-x}Al_xN$ coatings is superior to that of all the alloys investigated due to the very dense oxide layer formed. For example, the approx. 3 μm thick $Ti_{0.42}Al_{0.58}N$ is completely oxidized after 10 h at 850 °C in an ambient atmosphere, whereas the Ta-alloyed $Ti_{0.42}Al_{0.48}Ta_{0.10}N$ hard coating has only an ≈ 1.3-μm-thin oxide layer even after 20 h at 950 °C. Further alloying concepts, like with Si or reactive elements (such as Y, Ce, and La) additionally boost their oxidation resistance. Combining these effects with production technology of the corresponding target materials led to the development of $CeSi_2$ an LaB_6 alloyed targets and coatings that outperform their relatives in strength, thermomechanical properties, as well as oxidation resistance. For example, the characteristics of $Ti_{0.50}Al_{0.50}N(CeSi_2)_{0.02}$ are, $H = 35.3 \pm 1.3$ GPa in the as-deposited state and still 31.9 ± 2.2 GPa after vacuum annealing for 10 min at 1200 °C and only an ≈ 0.6-μm-thin oxide scale after 10 h exposure at 950 °C in ambient air.

Multilayers and superlattices as well as nanocomposites allow for an additional degree of design-flexibility. For example, the oxide scale grown onto the $Ti_{0.34}Al_{0.48}Ta_{0.18}N/Ti_{0.56}Al_{0.34}Si_{0.10}N$-multilayer is only ≈ 0.3 μm thin after 10 h at 950 °C in ambient air. Such concepts are also highly beneficial for the fracture toughness without compromising strength or oxidation resistance. Superlattice structures are particularly advantageous here in order to achieve hardness and fracture toughness values that are far above the arithmetic mean value of their constituting layers. Especially when such structures are combined with alloying concepts – such as Ta, Mo, and W – able to increase the inherent ductility of TiN, CrN, or (Ti,Al)N, which are themselves rather brittle. But the use of epitaxial stabilization effects through superlattices can also enhance hardness and toughness, like shown for superlattices containing MoN_z, WN_z, SiN_z, or AlN layers. As a result, in addition to coherency stresses (due to lattice mismatches) and modulus mismatches, phases as well as stoichiometries that may exhibit higher inherent ductility, according to their decreased *G/B* ratio and increased Cauchy pressure, become accessible. Loading of such superlattices causes additional nucleation and emission of numerous dislocations at the layer-interfaces and triggers the transformation of the epitaxial stabilized layer-material towards its more thermodynamically stable state. Together, these effects dissipate additional energy and allow for an improved fracture toughness, as shown for TiN/WN superlattices ($H = 36.7 \pm 0.8$ GPa and $K_{Ic} = 4.6 \pm 0.2$ MPa·$m^{0.5}$ for $\Lambda = 8.1$ and 10.2 nm, respectively). Corresponding processes might be active in nanocomposites or (Ti,Al)N-based materials, where coherent Al-rich and Ti-rich fcc-structured domains form due to spinodal decomposition, explaining the observed increase in fracture toughness upon annealing.

Thus, with this review we have summarized and demonstrated that the thermomechanical properties, fracture toughness, and oxidation resistance of $Ti_{1-x}Al_xN$ can be improved simultaneously through knowledge-based materials developments. This is essential to meet the ever-increasing demands on this material system. However, the guidelines presented are by no means limited to (Ti,Al)N and similar nitrides, but are also relevant for other materials such as carbides and borides, as well as protective and functional thin films in general.

CRediT authorship contribution statement

Paul H. Mayrhofer: Conceptualization, Data curation, Formal analysis, Funding acquisition, Investigation, Methodology, Project administration, Resources, Software, Validation, Visualization, Writing – original draft, Writing – review & editing. **Helmut Clemens:** Conceptualization, Writing – review & editing. **Franz D. Fischer:** Conceptualization, Writing – review & editing.

Declaration of competing interest

The authors declare that they have no known competing financial interests or personal relationships that could have appeared to influence the work reported in this paper.

Data availability

Data will be made available on request.

Acknowledgments

PHM gratefully acknowledges the support from the Austrian Science Fund (FWF) 10.55776/PAT4425523. For open access purposes, the author has applied a CC BY public copyright license to any author accepted manuscript version arising from this submission. We acknowledge the use of the USTEM (the electron microscopy facility) and XRC (X-ray center) at TU Wien. The computational results presented have been achieved in part using the Vienna Scientific Cluster (VSC).

References

[1] Astakhov VP. Tribology of cutting tools. In: Davim PJ, editor. Tribology in manufacturing technology. Springer: New York; 2012. p. 1–66.
[2] Inspector A, Salvador PA. Architecture of PVD coatings for metalcutting applications: a review. Surf Coat Technol 2014;257:138–53.
[3] Wang B, Liud Z, Cai Y, Luo X, Ma H, Song Q, et al. Advancements in material removal mechanism and surface integrity of high speed metal cutting: a review. Int J Mach Tools Manuf 2021;166:103744.
[4] Pervaiz S, Deiab I, Wahba E, Rashid A, Nicolescu M. A numerical and experimental study to investigate convective heat transfer and associated cutting temperature distribution in single point turning. Int J Adv Manuf Technol 2018;94:897–910.
[5] Pliny the Elder. Natural History: A Selection. Penguin Classics 2004 ISBN: 9780140444131.
[6] Roberts PM. Gold brazing in antiquity: technical achievements in the earliest civilisations. Gold Bull 1973;6:112–9.
[7] Altman J. Gold in Ancient Palestine. methods of fabrication in successive cultures. Gold Bull 1979;12:75–82.
[8] Nicholson ED. The ancient craft of gold beating. Gold Bull 1979;12:161–6.
[9] Sachse M. Damaszener Stahl: Mythos, Geschichte, Technik, Anwendung, 1. Aufl, Wirtschaftsverl. NW, Verl. für Neue Wiss.: Bremerhaven; 1989.
[10] Verhoeven JD, Pendray AH, Dauksch WE. The key role of impurities in ancient Damascus steel blades. JOM 1998;50(9):58–64.
[11] Wadsworth J, Sherby OD. Damascus Steels. Sci Am 1985:94–9.
[12] Arzt E. Size effects in materials due to microstructural and dimensional constraints: a comparative review. Acta Mater 1998;46(16):5611–26.
[13] Dehm G. Miniaturized single-crystalline fcc metals deformed in tension: New insights in size-dependent plasticity. Prog Mater Sci 2009;54(6):664–88.
[14] Veprek S, Argon AS, Zhang RF. Design of ultrahard materials: Go nano! Philos Mag 2010;90(31–32):4104–15.
[15] Greene JE. Low-energy ion/surface interactions during crystal growth from vapor phase: Effects on nucleation and growth, defect creation and annihilation, microstructure evolution and synthesis of metastable phases. In: Handbook of Crystal Growth, Vol. I: Fundamentals. a: thermodynamics and kinetics; b: transport and stability. (edited by Hurle DTJ) Elsevier Science Publishers; 1993, pp. 41.
[16] Greene JE. Thin Film Nucleation, Growth, and Microstructural Evolution: An Atomic Scale View. In: Martin PM, editor. Handbook of Deposition Technologies for Films and Coatings (Third Edition). Oxford: William Andrew Publishing; 2010. p. 554.
[17] Holleck H. Möglichkeiten und Grenzen einer gezielten Stoffauswahl für verschleißfeste Hartstoffschichten. Z Werkstofftech 1986;17:334–49.
[18] Knotek O, Bosch W, Leyendecker T. Verschleissmindernde Schichten im System Ti-Al-C-N-O durch Kathodenzerstäubung. In: Proc 11th Int Plansee Sem May 20–24 1985, Metallwerk Plansee: Reutte, 1985:677–691.
[19] Knotek O, Bohmer M, Leyendecker T. On structure and properties of sputtered Ti and Al based hard compound films. J Vac Sci Technol A 1986;4:2695–700.
[20] Münz W-D. Titanium aluminum nitride films: a new alternative to TiN coatings. J Vac Sci Technol A 1986;4:2717–25.
[21] Hultman L. Thermal stability of nitride thin films. Vacuum 2000;57(1):1–30.
[22] Mitterer C, Mayrhofer PH, Musil J. Thermal stability of PVD hard coatings. Vacuum 2003;71(1–2):279–84.
[23] Mayrhofer PH, Mitterer C, Hultman L, Clemens H. Microstructural design of hard coatings. Prog Mater Sci 2006;51(8):1032–114.
[24] Ikeda T, Satoh H. Phase formation and characterization of hard coatings in the Ti-Al-N system prepared by the cathodic arc ion plating method. Thin Solid Films 1991;195:99–110.
[25] Münz W-D, Hurkmans T, Keiren G, Trinh T. Comparison of TiAlN coatings grown by unbalanced magnetron and arc bond sputtering techniques. J Vac Sci Technol A 1993;11:2583–9.
[26] Stueber M, Holleck H, Leiste H, Seemann K, Ulrich S, Ziebert C. Concepts for the design of advanced nanoscale PVD multilayer protective thin films. J Alloys Compd 2009;483(1–2):321–33.
[27] Schwarz K, Blaha P, Trickey SB. Electronic structure of solids with WIEN2k. Mol Phys 2010;108(21–23):3147–66.
[28] Mayrhofer PH, Hörling A, Karlsson L, Sjölén J, Larsson T, Mitterer C, et al. Self-organized nanostructures in the Ti–Al–N system. Appl Phys Lett 2003;83(10):2049–51.
[29] Münz WD, Gobel J. Properties of CrN and (Ti, Al)N coatings produced by high rate sputter deposition. Surf Eng 1987;3:47–52.
[30] PalDey S, Deevi SC. Single layer and multilayer wear resistant coatings of (Ti, Al)N: a review. Mater Sci Eng A 2003;342(1–2):58–79.
[31] Navinsek B, Panjan P, Urankar I, Cvahte P, Gorenjak F. Improvement of hot-working processes with PVD coatings and duplex treatment. Surf Coat Technol 2001;142–144:1148–54.
[32] Mayrhofer PH, Tischler G, Mitterer C. Microstructure and mechanical/thermal properties of Cr–N coatings deposited by reactive unbalanced magnetron sputtering. Surf Coat Technol 2001;142–144:78–84.
[33] Panjan P, Boncina I, Bevk J, Cékada M. PVD hard coatings applied for the wear protection of drawing dies. Surf Coat Technol 2005;200:133–6.
[34] Li WZ, Wang QM, Gong J, Sun C, Jiang X. Interdiffusion reaction in the CrN interlayer in the NiCrAlY/CrN/DSM11 system during thermal treatment. Appl Surf Sci 2009;255:8190–3.

[35] Park K-C, Kim K-B, Raaijmakers IJMM, Ngan K. The effect of density and microstructure on the performance of TiN barrier films in Cu metallization. J Appl Phys 1996;80:5674–81.
[36] Manaud JP, Poulon A, Gomez S, Le Petitcorps Y. A comparative study of CrN, ZrN, NbN and TaN layers as cobalt diffusion barriers for CVD diamond deposition on WC–Co tools. Surf Coat Technol 2007;202:222–31.
[37] Fox-Rabinovich GS, Veldhuis SC, Dosbaeva GK, Yamamoto K, Kovalev AI, Wainstein DL, et al. Nanocrystalline coating design for extreme applications based on the concept of complex adaptive behavior. J Appl Phys 2008;103:083510.
[38] Shizhi L, Yulong S, Hongrui P. Ti–Si–N films prepared by plasma-enhanced chemical vapor deposition. Plasma Chem Plasma Process 1992;12:287–97.
[39] Diserens M, Patscheider J, Lévy F. Mechanical properties and oxidation resistance of nanocomposite TiN–SiN physical-vapor-deposited thin films. Surf Coat Technol 1999;120–121:158–65.
[40] Patscheider J, Zehnder T, Diserens M. Structure–performance relations in nanocomposite coatings. Surf Coat Technol 2001;146–147:201–8.
[41] Münz WD, Lewis DB, Hovsepian PE, Schonjahn C, Ehiasarian A, Smith IJ. Industrial scale manufactured superlattice hard PVD coatings. Surf Eng 2001;17:15–27.
[42] Wasa K, Hayakawa S. Structures and resistive properties of sputtered Ti-Zr-Al-N thin films. Thin Solid Films 1972;10:367–75.
[43] Beensh-Marchwicka G, Krol-Stepniewska L, Posadowski W. Structure of thin films prepared by the cosputtering of titanium and aluminium or titanium and silicon. Thin Solid Films 1981;82:313–20.
[44] Fleischer RL. Solution Hardening. Acta Metall 1961;9:996–1000.
[45] Fleischer RL. Substitutional Solution Hardening. Acta Metall 1963;11:203–9.
[46] Labusch R. A statistical theory of solid solution hardening. Phys Status Solidi 1970;41(2):659–69.
[47] Labusch R. Statistical theories of solid solution hardening. Acta Metall 1972;20:917–27.
[48] Labusch R. Statistical theory of dislocation configurations in a random array of point obstacles. J Appl Phys 1977;48:4550–6.
[49] Schwarz RB, Labusch R. Dynamic simulation of solution hardening. J Appl Phys 1978;49:5174–87.
[50] Gypen LA, Deruyttere A. The combination of atomic size and elastic modulus misfit interactions in solid solution hardening. Scr Metall 1981;15:815–20.
[51] Bhakhri V, Wang J, Ur-rehman N, Ciurea C, Giuliani F, Vandeperre LJ. Instrumented nanoindentation investigation into the mechanical behavior of ceramics at moderately elevated temperatures. J Mater Res 2012;27(1):65–75.
[52] Giuliani F, Ciurea C, Bhakhri V, Werchota M, Vandeperre LJ, Mayrhofer PH. Deformation behaviour of TiN and Ti–Al–N coatings at 295 to 573K. Thin Solid Films 2019;688:137363.
[53] Hill R. The elastic behaviour of a crystalline aggregate. Proc Phys Soc A 1952;65:349–54.
[54] Voigt W. Lehrbuch der Kristallphysik (mit Ausschluss der Kristalloptik). Leipzig: Teubner; 1910. p. 1–964.
[55] Reuss A. Berechnung der Fließgrenze von Mischkristallen auf Grund der Plastizitätsbedingung für Einkristalle. Angew Math Mech 1929;9:49–58.
[56] Holec D, Friák M, Neugebauer J, Mayrhofer PH. Trends in the elastic response of binary early transition metal nitrides. Phys Rev B 2012;85:064101.
[57] Ranganathan SI, Ostoja-Starzewski M. Universal elastic anisotropy index. Phys Rev Lett 2008;101:055504.
[58] Tasnádi F, Abrikosov IA, Rogström L, Almer J, Johansson MP, Odén M. Significant elastic anisotropy in $Ti_{1-x}Al_xN$ alloys. Appl Phys Lett 2010;97:231902.
[59] Tasnádi F, Odén M, Abrikosov IA. Ab initio elastic tensor of cubic $Ti_{0.5}Al_{0.5}N$ alloys: Dependence of elastic constants on size and shape of the supercell model and their convergence. Phys Rev B 2012;85:144112.
[60] Taylor GI. The mechanism of plastic deformation of crystals. Part I -Theoretical. Proc R Soc A 1934;145:362–87.
[61] Orowan E. Zur Kristallplastizität I Z Phys 1934;89:605–13.
[62] Orowan E. Zur Kristallplastizität II Z Phys 1934;89:614–33.
[63] Orowan E. Zur Kristallplastizität III Z Phys 1934;89:634–59.
[64] Polanyi M. Über eine Art Gitterstörung, die einen Kristall plastisch machen könnte. Z Phys 1934;89:660–4.
[65] Dehlinger U. Zur Theorie der Rekristallisation reiner Metalle. Annalen der Physik 1929;2:749–93.
[66] Prantl L. Ein Gedankenmodell zur kinetischen Theorie der festen Körper. Z Angew Math Mech 1928;8:85–106.
[67] Masing G, Polanyi M. Kaltreckung und Verfestigung. In: der Naturwissenschaften S, editor. Ergebnisse der Exakten Naturwissenschaften. Heidelberg: Springer, Berlin; 1923.
[68] Polanyi M. Kristalldeformation und Verfestigung. Z Metallkd 1925;17:94–5.
[69] Polanyi M. Deformation von Einkristallen. Z. Kristallogr 1925;61:49–57.
[70] Frenkel J. Zur Theorie der Elastizitätsgrenze und der Festigkeit kristallinischer Körper. Z Phys 1926;37:572–609.
[71] Timpe A. Probleme der Spannungsverteilung in ebenen Systemen einfach gelöst mit Hilfe der Airyschen Funktion. Dissertation, Göttingen; 1905.
[72] Volterra V. Sur l'équilibre des corps élastiques multiplement connexes. Ann Sci Éc Norm Supér 1907;3(24):401–517.
[73] Meissner W, Polanyi M, Schmid E. Messungen mit Hilfe von flüssigem Helium. XII Z Phys 1930;66:477–89.
[74] Joffé AF. The physics of crystals. New-York/London: McGraw-Hill; 1928.
[75] Burgers WG. How my brother and i became interested in dislocations. Proc Roy Soc Lond A Math Phys Sci 1980;371(1744):125–30.
[76] Burgers JM. Some considerations on the fields of stress connected with dislocations in a regular crystal lattice I. Proc K Ned Akad Wet XLII 1939;4:293–325.
[77] Burgers JM. Some considerations on the fields of stress connected with dislocations in a regular crystal lattice II. (Solutions of the equations of elasticity for a non-isotropic substance of regular crystalline symmetry). Proc K Ned Akad Wet XLII 1939;5:378–99.
[78] Burgers JM. Geometrical considerations concerning the structural irregularities to be assumed in a crystal. Proc Phys Soc 1940;52:23–33.
[79] Burgers JM, Burgers WG. Dislocations in crystal lattices. In: Eirich FR (Ed). Rheology, vol I: New York; 1956.
[80] Dislocations FJ. International Series of Monographs on Solid State Physics. Oxford: Pergamon Press; 1964.
[81] Xu Z, Zhang Z, Bartosik M, Zhang Y, Mayrhofer PH, He Y. Insight into the structural evolution during TiN film growth via atomic resolution TEM. J Alloys Comp 2018;754:257–67.
[82] Hall EO. The deformation and ageing of mild steel: III discussion of results. Proc Phys Soc London B 1951;64:747–53.
[83] Petch NJ. The cleavage strength of polycrystals. J Iron Steel Inst 1953;174:25–8.
[84] Lu L, Chen X, Huang X, Lu K. Revealing the maximum strength in nanotwinned copper. Science 2009;323:607–10.
[85] Xiao J, Deng C. Mitigating the Hall-Petch breakdown in nanotwinned Cu by amorphous intergranular films. Scripta Mater 2021;194:113682.
[86] Naik SN, Walley SM. The Hall-Petch and inverse Hall-Petch relations and the hardness of nanocrystalline metals. J Mater Sci 2020;55:2661–81.
[87] Shen YF, Lu L, Lu QH, Jin ZH, Lu K. Tensile properties of copper with nano-scale twins. Scripta Mater 2005;52:989–94.
[88] Kelly A, Fine ME. The strength of an alloy-containing zones. Acta Metall 1957;5:365–7.
[89] Orowan E. Symposium on Internal Stresses in Metals and Alloys, Session III Discussion. London: Institute of Metals; 1948. p. 451–3.
[90] Gottstein G. Physical foundations of materials science. Berlin: Springer; 2004.
[91] Bacon D, Kocks U, Scattergood R. The effect of dislocation self-interaction on the Orowan stress. Philos Mag 1973;28:1241–63.
[92] Tabor D. A simple theory of static and dynamic hardness. Proc Roy Soc Lond A Math Phys Sci 1948;192:247–74.
[93] Atkins AG, Tabor D. Plastic indentation in metals with cones I. J Mech Phys Solids 1965;13:149–64.
[94] Schuh CA, Argon AS, Nieh TG, Wadsworth J. The transition from localized to homogeneous plasticity during nanoindentation of an amorphous metal. Philos Mag 2003;83(22):2585–97.
[95] Cheng YT, Cheng CM. Scaling approach to conical indentation in elastic-plastic solids with work hardening. J Appl Phys 1998;84:1284–91.
[96] Clausner A, Richter F. Determination of yield stress from nano-indentation experiments. Eur J Mech A/Solids 2015;51:11–20.
[97] Fischer-Cripps AC. Analysis of instrumented indentation test data for functionally graded materials. Surf Coat Technol 2003;168:136–41.
[98] Yang Q, Lengauer W, Koch T, Scheerer M, Smid I. Hardness and elastic properties of $Ti(C_xN_{1-x})$, $Zr(C_xN_{1-x})$ and $Hf(C_xN_{1-x})$. J Alloys Compd 2000;309:L5–9.
[99] Kuwahara H, Mazaki N, Takahashi M, Watanabe T, Yang X, Aizawa T. Mechanical properties of bulk sintered titanium nitride ceramics. Mater Sci Eng A 2001;319:687–91.

[100] El Azhari I, Garcia J, Zamanzade M, Soldera F, Pauly C, Llanes L, et al. Investigations on micro-mechanical properties of polycrystalline Ti(C, N) and Zr(C, N) coatings. Acta Mater 2018;149:364–76.

[101] Vandeperre LJ, Giuliani F, Clegg WJ. Effect of elastic surface deformation on the relation between hardness and yield strength. J Mater Res 2004;19(12): 3704–14.

[102] Yu T, Xue P. Introduction to engineering plasticity. Higher Education Press; 2022.

[103] Hencky H. Zur Theorie plastischer Deformationen und der hierdurch im Material hervorgerufenen Nachspannungen. Z Angew Math Mech 1924;4:323–34.

[104] v Mises R. Mechanik der festen Körper im plastisch-deformablen Zustand. Nachr Ges Wiss Gottingen Math-Phys Kl 1913;582–592.

[105] Lockett FJ. Indentation of a rigid/plastic material by a conical indenter. J Mech Phys Solids 1963;11:345–55.

[106] Schmid E. Zn-normal stress law. Proc Int Conf Appl Mech, Delft 1924;342.

[107] Schmid E. Bemerkungen über die plastische Deformation von Kristallen. Z Phys 1924:328–33.

[108] Sachs G. Zur Ableitung einer Fliessbedingung. Z Ver Dtsch Ing 1928;72:734–6.

[109] Taylor GI. Plastic strain in metals. J Inst Metals 1938;62:307–24.

[110] Clausen B. Characterisation of Polycrystal Deformation by Numerical Modelling and Neutron Diffraction Measurements. PhD thesis Risø National Laboratory: Roskilde; 1997.

[111] Liu S, Wheeler JM, Michler J, Zeng XT, Clegg WJ. Plastic flow at the theoretical yield stress in ceramic films. Scripta Mater 2016;117:24–7.

[112] Karlsson L, Hörling A, Johansson MP, Hultman L, Ramanath G. The influence of thermal annealing on residual stresses and mechanical properties of arc-evaporated TiC_xN_{1-x} thin films. Acta Mater 2002;50:5103–14.

[113] Reiter AE, Derflinger VH, Hanselmann B, Bachmann T, Sartory B. Investigation of the properties of $Al_{1-x}Cr_xN$ coatings prepared by cathodic arc evaporation. Surf Coat Technol 2005;200(7):2114–22.

[114] McIntyre D, Greene JE, Håkansson G, Sundgren JE, Münz WD. Oxidation of metastable single-phase polycrystalline $Ti_{0.5}Al_{0.5}N$ films: Kinetics and mechanisms. J Appl Phys 1990;67:1542–53.

[115] Hasegawa H, Suzuki T. Effects of second metal contents on microstructure and micro-hardness of ternary nitride films synthesized by cathodic arc method. Surf Coat Technol 2004;188–189:234–40.

[116] Chim YC, Ding XZ, Zeng XT, Zhang S. Oxidation resistance of TiN, CrN, TiAlN and CrAlN coatings deposited by lateral rotating cathode arc. Thin Solid Films 2009;517:4845–9.

[117] Hörling A, Hultman L, Odén M, Sjölén J, Karlsson L. Mechanical properties and machining performance of $Ti_{1-x}Al_xN$-coated cutting tools. Surf Coat Technol 2005;191:384–92.

[118] Barshilia HC, Selvakumar N, Deepthi B, Rajam KS. A comparative study of reactive direct current magnetron sputtered CrAlN and CrN coatings. Surf Coat Technol 2006;201(6):2193–201.

[119] Lin J, Mishra B, Moore JJ, Sproul WD. A study of the oxidation behavior of CrN and CrAlN thin films in air using DSC and TGA analyses. Surf Coat Technol 2008;202:3272–83.

[120] Schuster JC, Bauer J. The ternary system titanium-aluminum-nitrogen. J Solid State Chem 1984;53:260–5.

[121] Prange R, Cremer R, Neuschütz D. Plasma-enhanced CVD of (Ti, Al)N films from chloridic precursors in a DC glow discharge. Surf Coat Technol 2000;133–134: 208–14.

[122] Barbee TW, Holmes WH, Keith DL, Pyzyna MK, Ilonca G. Synthesis of amorphous niobium-nickel alloys by vapor quenching. Thin Solid Films 1977;45(3): 591–9.

[123] Holleck H. Metastable coatings – prediction of composition and structure. Surf Coat Technol 1988;36:151–9.

[124] Mayrhofer PH, Fischer FD, Böhm HJ, Mitterer C, Schneider JM. Energetic balance and kinetics for the decomposition of supersaturated $Ti_{1-x}Al_xN$. Acta Mater 2007;55(4):1441–6.

[125] Xia Q, Xia H, Ruoff AL. Pressure-induced rocksalt phase of aluminum nitride: a metastable structure at ambient condition. J Appl Phys 1993;73:8198–200.

[126] Zhang RF, Veprek S. Deformation paths and atomistic mechanism of B4 → B1 phase transformation in aluminium nitride. Acta Mater 2009;57:2259–65.

[127] Fischer FD, Antretter T. Deformation, stress state and thermodynamic force for a growing void in an elastic–plastic material. Int J Plast 2009;25:1819–32.

[128] Zhou M, Makino Y, Nose M, Nogi K. Phase transition and properties of Ti–Al–N thin films prepared by r.f.-plasma assisted magnetron sputtering. Thin Solid Films 1999;339:203–8.

[129] Mayrhofer PH, Music D, Schneider JM. Influence of the Al distribution on the structure, elastic properties, and phase stability of supersaturated $Ti_{1-x}Al_xN$. J Appl Phys 2006;100(9):094906.

[130] Cremer R, Witthaut M, Neuschütz D. Experimental determination of the metastable (Ti, Al)N phase diagram up to 700 °C. In: Cho WD, Sohn HY, editors. Value-Edition-Metallurgy. The Minerals &. Warrendale: Metals Society; 1998.

[131] Kimura A, Hasegawa H, Yamada K, Suzuki T. Effects of Al content on hardness, lattice parameter and microstructure of $Ti_{1-x}Al_xN$ films. Surf Coat Technol 1999; 120–121:438–41.

[132] Kutschej K, Mayrhofer PH, Kathrein M, Polcik P, Tessadri R, Mitterer C. Structure, mechanical and tribological properties of sputtered $Ti_{1-x}Al_xN$ coatings with $0.5 \leq x \leq 0.75$. Surf Coat Technol 2005;200(7):2358–65.

[133] Hugosson HW, Hogberg H, Algren M, Rodmar M, Selinder TI. Theory of the effects of substitutions on the phase stabilities of $Ti_{1-x}Al_xN$. J Appl Phys 2003;93: 4505–11.

[134] Mayrhofer PH, Music D, Schneider JM. Ab initio calculated binodal and spinodal of cubic $Ti_{1-x}Al_xN$. Appl Phys Lett 2006;88(7):071922.

[135] Zhang RF, Veprek S. Metastable phases and spinodal decomposition in $Ti_{1-x}Al_xN$ system studied by ab initio and thermodynamic modeling, a comparison with the $TiN–Si_3N_4$ system. Mater Sci Eng A 2007;448:111–9.

[136] Alling B, Ruban AV, Karimi A, Peil OE, Simak SI, Hultman L, et al. Mixing and decomposition thermodynamics of c-$Ti_{1-x}Al_xN$ from first-principles calculations. Phys Rev B 2007;75:045123.

[137] Makino Y. Prediction of phase change in pseudobinary transition metal aluminum nitrides by band parameters method. Surf Coat Technol 2005;193:185–91.

[138] Knotek O, Loffler F, Scholl H-J. Properties of arc-evaporated CrN and (Cr, Al)N coatings. Surf Coat Technol 1991;45:53–8.

[139] Kaindl R, Franz R, Soldan J, Reiter A, Polcik P, Mitterer C, et al. Structural investigations of aluminum-chromium-nitride hard coatings by Raman micro-spectroscopy. Thin Solid Films 2006;515:2197–202.

[140] Kawate M, Kimura A, Sezuki T. Microhardness and lattice parameter of $Cr_{1-x}Al_xN$ films. J Vac Sci Technol A 2002;20:569–71.

[141] Makino Y, Nogi K. Synthesis of pseudobinary Cr-Al-N films with Bl structure by rf-assisted magnetron sputtering method. Surf Coat Technol 1998;98:1008–12.

[142] Sugishima A, Kajioka H, Makino Y. Phase transition of pseudobinary Cr–Al–N films deposited by magnetron sputtering method. Surf Coat Technol 1997;97: 590–4.

[143] Zhang RF, Veprek S. Phase stabilities and spinodal decomposition in the $Cr_{1-x}Al_xN$ system studied by ab initio LDA and thermodynamic modeling: Comparison with the $Ti_{1-x}Al_xN$ and TiN/Si_3N_4 systems. Acta Mater 2007;55:4615–24.

[144] Mayrhofer PH, Music D, Reeswinkel T, Fuß HG, Schneider JM. Structure, elastic properties and phase stability of $Cr_{1-x}Al_xN$. Acta Mater 2008;56:2469–75.

[145] Alling B, Marten T, Abrikosov IA, Karimi A. Comparison of thermodynamic properties of cubic $Cr_{1-x}Al_xN$ and $Ti_{1-x}Al_xN$ from first-principles calculations. J Appl Phys 2007;102:044314.

[146] Bobzin K, Lugscheider E, Nickel R, Immich P. (Cr_{1-x}, A_lx)N ein Review über ein vielseitig einsetzbares Schichtsystem. Materwiss Werksttech 2006;37:833–41.

[147] Makino Y, Mori M, Miyake S, Saito K, Asami K. Characterization of Zr–Al–N films synthesized by a magnetron sputtering method. Surf Coat Technol 2005;193 (1–3):219–22.

[148] Sheng SH, Zhang RF, Veprek S. Phase stabilities and thermal decomposition in the $Zr_{1-x}Al_xN$ system studied by ab initio calculation and thermodynamic modeling. Acta Mater 2008;56(5):968–76.

[149] Sanjinés R, Sandu CS, Lamni R, Lévy F. Thermal decomposition of $Zr_{1-x}Al_xN$ thin films deposited by magnetron sputtering. Surf Coat Technol 2006;200: 6308–12.

[150] Holec D, Rachbauer R, Chen L, Wang L, Luef D, Mayrhofer PH. Phase stability and alloy-related trends in Ti–Al–N, Zr–Al–N and Hf–Al–N systems from first principles. Surf Coat Technol 2011;206:1698–704.

[151] Hasegawa H, Kawate M, Suzuki T. Effects of Al contents on microstructures of Cr$_{1-x}$Al$_x$N and Zr$_{1-x}$Al$_x$N films synthesized by cathodic arc method. Surf Coat Technol 2005;200:2409–13.

[152] Selinder TI, Miller DJ, Gray KE, Sardela MR, Hultman L. Phase formation and microstructure of Nb$_{1-x}$Al$_x$N alloy films grown on MgO (001) by reactive sputtering: a new ternary phase. Vacuum 1995;46(12):1401–6.

[153] Holec D, Franz R, Mayrhofer PH, Mitterer C. Structure and stability of phases within the NbN–AlN system. J Phys D: Appl Phys 2010;43(14):145403.

[154] Rafaja D, Wüstefeld C, Dopita M, Klemm V, Heger D, Schreiber G, et al. Formation of defect structures in hard nanocomposites. Surf Coat Technol 2008;203: 572–8.

[155] Rachbauer R, Massl S, Stergar E, Holec D, Kiener D, Keckes J, et al. Decomposition pathways in age hardening of Ti-Al-N films. J Appl Phys 2011;110:023515.

[156] Jehn HA, Hofmann S, Rückborn VE, Münz WD. Morphology and properties of sputtered (Ti, Al)N layers on high speed steel substrates as a function of deposition temperature and sputtering atmosphere. J Vac Sci Technol A 1986;4(6):2701–5.

[157] Jehn HA, Hofmann S, Münz W-D. Surface and interface characterization of heat-treated (Ti, Al)N coatings on high speed steel substrates. Thin Solid Films 1987;153(1–3):45–53.

[158] Cremer R, Witthaut M, Von Richthofen A, Neuschütz D. Determination of the cubic to hexagonal structure transition in the metastable system TiN-AlN. Fresenius J Anal Chem 1998;361(6–7):642–5.

[159] Hasegawa H, Kimura A, Suzuki T. Ti$_{1-x}$Al$_x$N, Ti$_{1-x}$Zr$_x$N and Ti$_{1-x}$Cr$_x$N films synthesized by the AIP method. Surf Coat Technol 2000;132(1):76–9.

[160] Spencer P. Thermodynamic Prediction of Metastable Coating Structures in PVD Processes. Z Metallkd 2001;92(10):1145–50.

[161] Chen L, Paulitsch J, Du Y, Mayrhofer PH. Thermal stability and oxidation resistance of Ti–Al–N coatings. Surf Coat Technol 2012;206:2954–60.

[162] Wuhrer R, Yeung WY, Phillips MR, McCredie G. Study on d.c. magnetron sputter deposition of titanium aluminium nitride thin films: effect of aluminium content on coating. Thin Solid Films 1996;290–291:339–42.

[163] Vaz F, Rebouta L, Andritschky M, Da Silva MF, Soares JC. Thermal oxidation of Ti$_{1-x}$Al$_x$N coatings in air. J Eur Ceram 1997;17(15–16):1971–7.

[164] Rebouta L, Vaz F, Andritschky M, da Silva MF. Oxidation resistance of (Ti, Al, Zr, Si)N coatings in air. Surf Coat Technol 1995;76:70–4.

[165] Vaz F, Rebouta L, Andritschky M, Da Silva MF, Soares JC. Oxidation resistance of (Ti, Al, Si)N coatings in air. Surf Coat Technol 1998;98(1–3):912–7.

[166] Huang JL, Shew BY. Effects of aluminum concentration on the oxidation behaviors of reactively sputtered TiAlN films. J Am Ceram Soc 1999;82(3):696–704.

[167] Hugon MC, Varniere F, Letendu F, Agius B, Vickridge I, Kingon AI. ^{18}O study of the oxidation of reactively sputtered Ti$_{1-x}$Al$_x$N barrier. J Mater Res 2001;16(9): 2591–9.

[168] PalDey S, Deevi SC. Properties of single layer and gradient (Ti, Al)N coatings. Mater Sci Eng A 2003;361(1–2):1–8.

[169] Brizuela M, Garcia-Luis A, Braceras I, Onate JI, Sánchez-Lopez JC, Martinez-Martinez D, et al. Magnetron sputtering of Cr(Al)N coatings: mechanical and tribological study. Surf Coat Technol 2005;200(1–4):192–7.

[170] Klostermann H, Fietzke H, Modes T, Zywitzki O. Zr-Al-N nanocomposite coatings deposited by pulse magnetron sputtering. Rev Adv Mater Sci 2007;15(1): 33–7.

[171] Barshilia HC, Deepthi B, Rajam KS, Bhatti KP, Chaudhary S. Structure and properties of reactive direct current magnetron sputtered niobium aluminum nitride coatings. J Mater Res 2008;23(5):1258–68.

[172] Kolozsvari S, Pesch P, Ziebert C, Stueber M, Ulrich S. Deposition and characterization of hard coatings in the material system V-Al–N by reactive magnetron sputter deposition. Plasma Processes Polym 2009;6(1):146–51.

[173] Franz R, Lechthaler M, Polzer C, Mitterer C. Structure, mechanical properties and oxidation behaviour of arc-evaporated NbAlN hard coatings. Surf Coat Technol 2010;204(15):2447–53.

[174] Mayrhofer PH, Kunc F, Musil J, Mitterer C. A comparative study on reactive and non-reactive unbalanced magnetron sputter deposition of TiN coatings. Thin Solid Films 2002;415:151–9.

[175] Mayrhofer PH, Mitterer C, Musil J. Structure–property relationships in single- and dual-phase nanocrystalline hard coatings. Surf Coat Technol 2003;174–175: 725–31.

[176] Ohring M. Materials Science of Thin Films - Deposition & Structure. San Diego: Academic Press; 2002.

[177] Cahn JW. On spinodal decomposition. Acta Met 1961;9:795–801.

[178] Cahn JW. Hardening by spinodal decomposition. Acta Met 1963;11:1275–82.

[179] Mayrhofer PH, Mitterer C, Clemens H. Self-organized nanostructures in hard ceramic coatings. Adv Eng Mater 2005;7(12):1071–82.

[180] Hörling A, Hultman L, Oden M, Sjolen J, Karlsson L. Thermal stability of arc evaporated high aluminum-content Ti$_{1-x}$Al$_x$N thin films. J Vac Sci Technol A 2002; 20:1815.

[181] Mayrhofer PH, Hultman L, Schneider JM, Staron P, Clemens H. Spinodal decomposition of cubic Ti$_{1-x}$Al$_x$N: comparison between experiments and modeling. Int J Mater Res 2007;11:1054–9.

[182] Alling B, Odén M, Hultman L, Abrikosov IA. Pressure enhancement of the isostructural cubic decomposition in Ti$_{1-x}$Al$_x$N. Appl Phys Lett 2009;95(18):181906.

[183] Abrikosov IA, Knutsson A, Alling B, Tasnádi F, Lind H, Hultman L, Odén M. Phase Stability and Elasticity of TiAlN. Materials 2011;4:1599–618.

[184] Porter AD, Easterling KE. Phase Transformations in Metals and Alloys. Cornwall: Stanley Thornes; 2000.

[185] Holec D, Rovere F, Mayrhofer PH, Barna PB. Pressure-dependent stability of cubic and wurtzite phases within the TiN–AlN and CrN–AlN systems. Scripta Mater 2010;62(6):349–52.

[186] Vegard L. Die Konstitution der Mischkristalle und die Raumfüllung der Atome. Z Phys 1921;5(1):17–26.

[187] Christensen NE, Gorczyca I. Calculated structural phase transitions of aluminum nitride under pressure. Phys Rev B 1993;47(8):4307–14.

[188] Alling B, Karimi A, Hultman L, Abrikosov IA. First-principles study of the effect of nitrogen vacancies on the decomposition pattern in cubic Ti$_{1-x}$Al$_x$N$_{1-y}$. Appl Phys Lett 2008;92(7):071903.

[189] Rachbauer R, Massl S, Stergar E, Felfer P, Mayrhofer PH. Atom probe specimen preparation and 3D interfacial study of Ti–Al–N thin films. Surf Coat Technol 2010;204:1811–6.

[190] Knutsson A, Ullbrand J, Rogström L, Norrby N, Johnson LJS, Hultman L, et al. Microstructure evolution during the isostructural decomposition of TiAlN-A combined in-situ small angle x-ray scattering and phase field study. J Appl Phys 2013;113:213518.

[191] Zhou JJ, Zhong J, Chen L, Zhang L, Du Y, Liu Z-K, et al. Phase equilibria, thermodynamics and microstructure simulation of metastable spinodal decomposition in c–Ti$_{1-x}$Al$_x$N coatings. Calphad: Comput Coupling Ph Diagr Thermochem 2017;56:92–101.

[192] Knutsson A, Johansson MP, Karlsson L, Odén M. Thermally enhanced mechanical properties of arc evaporated Ti$_{0.34}$Al$_{0.66}$N/TiN multilayer coatings. J Appl Phys 2010;108:044312.

[193] Rachbauer R, Holec D, Mayrhofer PH. Increased thermal stability of Ti–Al–N thin films by Ta alloying. Surf Coat Technol 2012;211:98–103.

[194] Cahn JW, Haasen P. Phase transformations in materials. New York: VCH; 1991.

[195] Mayrhofer PH, Fischer FD, Böhm HJ, Mitterer C, Schneider JM. Erratum to "Energetic balance and kinetics for the decomposition of supersaturated Ti$_{1-x}$Al$_x$N" [Acta Materialia 55 (2007) 1441–1446]. Acta Mater 2022;227:117741.

[196] Kato M. Hardening by spinodally modulated structure in bcc alloys. Acta Metall 1980;29:79–86.

[197] Kato M. Selected topics on material strength and thermally activated deformation processes. Mater Trans 2015;56:175–81.

[198] Chen L, Du Y, Mayrhofer PH, Wang SQ, Li J. The influence of age-hardening on turning and milling performance of Ti–Al–N coated inserts. Surf Coat Technol 2008;202:5158–61.

[199] Humphreys FJ, Hatherly M. Recrystallization and Related Annealing Phenomena. Oxford: Elsevier; 1995.

[200] Mayrhofer PH, Mitterer C, Wen JG, Petrov I, Greene JE. Thermally induced self-hardening of nanocrystalline Ti-B-N thin films. J Appl Phys 2006;100:044301.

[201] Chen J, Lu L, Lu K. Hardness and strain rate sensitivity of nanocrystalline Cu. Scripta Mater 2006;54:1913–8.

[202] Lin Y, Pan J, Luo Z, Lu Y, Lu K, Li Y. A grain-size-dependent structure evolution in gradient-structured (GS) Ni under tension. Nano Mater Sci 2020;2:39–49.

[203] Schuh CA, Nieh TG, Iwasaki H. The effect of solid solution W additions on the mechanical properties of nanocrystalline Ni. Acta Mater 2003;51:431–43.

[204] Li CL, Mei QS, Li JY, Chen F, Ma Y, Mei XM. Hall-Petch relations and strengthening of Al-ZnO composites in view of grain size relative to interparticle spacing. Scripta Mater 2018;153:27–30.

[205] Wollmershauser JA, Feigelson BN, Gorzkowski EP, Ellis CT, Goswami R, Qadri SB, et al. An extended hardness limit in bulk nanoceramics. Acta Mater 2014;69:9–16.

[206] Karlsson L. Arc Evaporated Titanium Carbonitride Coatings PhD thesis, (Linköping Studies in Science and Technology, dissertation no. 565, Linköping University, Sweden, 1999. ISBN: 9172194200.

[207] Knotek O, Münz WD, Leyendecker T. Industrial deposition of binary, ternary, and quaternary nitrides of titanium, zirconium, and aluminum. J Vac Sci Technol A 1987;5:2173–9.

[208] Erdemir A. A crystal chemical approach to the formulation of self-lubricating nanocomposite coatings. Surf Coat Technol 2005;200:1792–6.

[209] Gassner G, Mayrhofer PH, Kutschej K, Mitterer C, Kathrein M. Magnéli phase for-mation of PVD Mo-N and W-N coatings. Surf Coat Technol 2006;201:3335–41.

[210] Bartosik M, Rumeau C, Hahn R, Zhang ZL, Mayrhofer PH. Fracture toughness and structural evolution in the TiAlN system upon annealing. Sci Rep 2017;7:16476.

[211] Zagorac D, Zagorac J, Djukic MB, Jordanov D, Matović B. Theoretical study of AlN mechanical behaviour under high pressure regime. Theor Appl Fract Mech 2019;103:102289.

[212] Yonenaga I, Nikolaev A, Melnik Y, Dmitriev V. High-temperature hardness of bulk single-crystal AlN. MRS Online Proc Libr 2001;693:104–9.

[213] Flink A, Andersson JM, Alling B, Daniel R, Sjölén J, Karlsson L, et al. Structure and thermal stability of arc evaporated $(Ti_{0.33}Al_{0.67})_{1-x}Si_xN$ thin films. Thin Solid Films 2008;517(2):714–21.

[214] Heim D, Hochreiter R. TiAlN and TiAlCN deposition in an industrial PaCVD-plant. Surf Coat Technol 1998;98(1–3):1553–6.

[215] Holubář P, Jílek M, Šíma M. Nanocomposite nc-TiAlSiN and nc-TiN–BN coatings: their applications on substrates made of cemented carbide and results of cutting tests. Surf Coat Technol 1999;120–121:184–8.

[216] Rebholz C, Schneider JM, Voevodin AA, Steinebrunner J, Charitidis C, Logothetidis S, et al. Structure, mechanical and tribological properties of sputtered TiAlBN thin films. Surf Coat Technol 1999;113(1–2):126–33.

[217] Durand-Drouhin O, Santana AE, Karimi A, Derflinger VH, Schütze A. Mechanical properties and failure modes of TiAl(Si)N single and multilayer thin films. Surf Coat Technol 2003;163–164:260–6.

[218] Lackner JM, Waldhauser W, Ebner R, Bakker RJ, Schöberl T, Major B. Room temperature pulsed laser deposited (Ti, Al)$_{\mathrm{C}}$x$_{\mathrm{N1}}$-x coatings—chemical, structural, mechanical and tribological properties. Thin Solid Films 2004;468(1–2):125–33.

[219] Parlinska-Wojtan M, Karimi A, Coddet O, Cselle T, Morstein M. Characterization of thermally treated TiAlSiN coatings by TEM and nanoindentation. Surf Coat Technol 2004;188–189(1–3):344.

[220] Stueber M, Barna PB, Simmonds MC, Albers U, Leiste H, Ziebert C, et al. Constitution and microstructure of magnetron sputtered nanocomposite coatings in the system Ti–Al–N–C. Thin Solid Films 2005;493(1–2):104–12.

[221] Veprek S, Reiprich S. A concept for the design of novel superhard coatings. Thin Solid Films 1995;268:64–71.

[222] Mollart TP, Baker M, Haupt J, Steiner A, Hammer P, Gissler W. Nanostructured titanium boron nitride coatings of very high hardness. Surf Coat Technol 1995;74:491–6.

[223] Chaleix L, Machet J. Study of the composition and of the mechanical properties of TiBN films obtained by d.c. magnetron sputtering. Surf Coat Technol 1997;91:74–82.

[224] Rebholz C, Leyland A, Larour P, Charitidis C, Logothetidis S, Matthews A. The effect of boron additions on the tribological behaviour of TiN coatings produced by electron-beam evaporative PVD. Surf Coat Technol 1999;116–119:648–53.

[225] Donohue LA, Smith IJ, Münz W-D, Petrov I, Greene JE. Microstructure and oxidation-resistance of $Ti_{1-x-y-z}Al_xCr_yY_zN$ layers grown by combined steered-arc/unbalanced-magnetron-sputter deposition. Surf Coat Technol 1997;94–95:226–31.

[226] Donohue LA, Lewis DB, Münz W-D, Stack MM, Lyon SB, Wang H-W, et al. The influence of low concentrations of chromium and yttrium on the oxidation behaviour, residual stress and corrosion performance of TiAlN hard coatings on steel substrates. Vacuum 1999;55(2):109–14.

[227] Pflüger E, Schroer A, Voumard P, Donohue L, Münz W-D. Influence of incorporation of Cr and Y on the wear performance of TiAlN coatings at elevated temperatures. Surf Coat Technol 1999;115(1):17–23.

[228] Moser M, Kiener D, Scheu C, Mayrhofer PH. Influence of Yttrium on the Thermal Stability of Ti-Al-N Thin Films. Materials 2010;3:1573–92.

[229] Riedl H, Holec D, Rachbauer R, Polcik P, Hollerweger R, Paulitsch J, et al. Phase stability, mechanical properties and thermal stability of Y alloyed Ti–Al–N coatings. Surf Coat Technol 2013;235:174–80.

[230] Gil A, Rajchel B, Zheng N, Quadakkers WJ, Nickel H. The influence of implanted chromium and yttrium on the oxidation behaviour of TiAl-based intermetallics. J Mater Sci 1995;30:5793–8.

[231] Pint BA. Experimental observations in support of the dynamic-segregation theory to explain the reactive-element effect. Oxid Met 1996;45:1–37.

[232] Grabke HJ, Schütze M, editors. Oxidation of Intermetallics. Weinheim: Wiley-VCH GmbH; 1998.

[233] Lang E, editor. The role of Active Elements in the Oxidation Behaviour of High Temperature Metals and Alloys. London: Elsevier; 1989.

[234] Moon DP. Role of reactive elements in alloy protection. Mater Sci Technol 1989;5:754–64.

[235] Mrowec S, Jedliński J, Gil A. The influence of certain reactive elements on the oxidation behaviour of chromia- and alumina-forming alloys. Mater Sci Eng A 1989;120:169–73.

[236] Choi WS, Hwang SK, Lee CM. Microstructure and chemical state of $Ti_{1-x}Y_xN$ film deposited by reactive magnetron sputtering. J Vac Sci Technol A 2000;18:2914–21.

[237] Moser M, Mayrhofer PH. Yttrium-induced structural changes in sputtered $Ti_{1\text{-}x}Al_xN$ thin films. Scripta Mater 2007;57:357–60.

[238] Knotek O, Leyendecker T, Jungblut F. On the properties of physically vapour-deposited Ti-Al-V-N coatings. Thin Solid Films 1987;153:83–90.

[239] Kutschej K, Mayrhofer PH, Kathrein M, Polcik P, Mitterer C. A new low-friction concept for $Ti_{1-x}Al_xN$ based coatings in high-temperature applications. Surf Coat Technol 2004;188:358–63.

[240] Mayrhofer PH, Hovsepian PE, Mitterer C, Münz W-D. Calorimetric evidence for frictional self-adaptation of TiAlN/VN superlattice coatings. Surf Coat Technol 2004;177–178:341–7.

[241] Kutschej K, Mayrhofer PH, Kathrein M, Polcik P, Mitterer C. Influence of oxide phase formation on the tribological behaviour of Ti–Al–V–N coatings. Surf Coat Technol 2005;200:1731–7.

[242] Pfeiler M, Kutschej K, Penoy M, Michotte C, Mitterer C, Kathrein M. The influence of bias voltage on structure and mechanical/tribological properties of arc evaporated Ti–Al–V–N coatings. Surf Coat Technol 2007;202:1050–4.

[243] Glatz SA, Koller CM, Bolvardi H, Kolozsvári S, Riedl H, Mayrhofer PH. Influence of Mo on the structure and the tribomechanical properties of arc evaporated Ti-Al-N. Surf Coat Technol 2017;311:330–6.

[244] Knotek O, Böhmer M, Leyendecker T, Jungblut F. The Structure and Composition of Ti-Zr-N, Ti-Al-Zr-N and Ti-A-V-N Coatings. Mater Sci Eng A 1988;105–106:481–8.

[245] Donohue LA, Cawley J, Brooks JS, Münz W-D. Deposition and characterization of TiAlZrN films produced by a combined steered arc and unbalanced magnetron sputtering technique. Surf Coat Technol 1995;74–75:123–34.

[246] Cremer R, Neuschütz D. A combinatorial approach to the optimization of metastable multicomponent hard coatings. Surf Coat Technol 2001;146–147:229–36.

[247] Kutschej K, Fateh N, Mayrhofer PH, Kathrein M, Polcik P, Mitterer C. Comparative study of $Ti_{1-x}Al_xN$ coatings alloyed with Hf, Nb, and B. Surf Coat Technol 2005;200:113–7.

[248] Feng C, Zhu S, Li M, Xin L, Wang F. Effects of incorporation of Si or Hf on the microstructure and mechanical properties of Ti–Al–N films prepared by arc ion plating (AIP). Surf Coat Technol 2008;202:3257–62.

[249] Pfeiler M, Fontalvo GA, Wagner J, Kutschej K, Penoy M, Michotte C, et al. Arc Evaporation of Ti–Al–Ta–N coatings: the effect of bias voltage and Ta on high-temperature tribological properties. Tribol Lett 2008;30(2):91–7.

[250] Pfeiler M, Scheu C, Hutter H, Schnöller J, Michotte C, Mitterer C, et al. On the effect of Ta on improved oxidation resistance of Ti–Al–Ta–N coating. J Vac Sci Technol A 2009;27(3):554–60.

[251] Braic V, Zoita CN, Balaceanu M, Kiss A, Vladescu A, Popescu A, et al. TiAlN/TiAlZrN multilayered hard coatings for enhanced performance of HSS drilling tools. Surf Coat Technol 2010;204(12–13):1925–8.

[252] Chen L, Holec D, Du Y, Mayrhofer PH. Influence of Zr on structure, mechanical and thermal properties of Ti–Al–N. Thin Solid Films 2011;519(16):5503–10.

[253] Rovere F, Mayrhofer PH, Reinholdt A, Mayer J, Schneider JM. The effect of yttrium incorporation on the oxidation resistance of Cr-Al-N coatings. Surf Coat Technol 2008;202:5870–5.

[254] Berg S, Katardjiev IV. Preferential sputtering effects in thin film processing. J Vac Sci Technol A 1999;17:1916–25.

[255] Asanuma H, Klimashin FF, Polcik P, Kolozsvári S, Riedl H, Mayrhofer PH. Impact of lanthanum and boron on the growth, thermomechanical properties and oxidation resistance of Ti–Al–N thin films. Thin Solid Films 2019;688(137239):1–8.

[256] Asanuma H, Polcik P, Kolozsvari S, Klimashin FF, Riedl H, Mayrhofer PH. Cerium doping of Ti-Al-N coatings for excellent thermal stability and oxidation resistance. Surf Coat Technol 2017;326:165–72.

[257] Asanuma H, Klimashin FF, Polcik P, Kolozsvari S, Riedl H, Mayrhofer PH. Thermomechanical properties and oxidation resistance of Ce–Si alloyed Ti–Al–N thin films. Vacuum 2019;166:231–8.

[258] Asanuma H, Klimashin FF, Polcik P, Kolozsvári S, Riedl H, Mayrhofer PH. Hard Ti-Al-N endowed with high heat-resistance through alloying with Ta and Ce. Surf Coat Technol 2019;372:26–33.

[259] Rachbauer R, Holec D, Lattemann M, Hultman L, Mayrhofer PH. Electronic origin of structure and mechanical properties in Y and Nb alloyed Ti–Al–N thin films. Int J Mater Res 2011;102:735–42.

[260] Rachbauer R, Blutmager A, Holec D, Mayrhofer PH. Effect of Hf on structure and age hardening of Ti-Al-N thin films. Surf Coat Technol 2012;206:2667–72.

[261] Rachbauer R, Holec D, Mayrhofer PH. Phase stability and decomposition products of Ti–Al–Ta–N thin films. Appl Phys Lett 2010;97:151901.

[262] Mayrhofer PH, Kagerer S, Polcik P, Kirnbauer A. Superior oxidation resistance of the chemically complex but structurally simple Ti-Al-Ta-Ce-Si-La-B-nitride. Mater Des 2023;227(111722):1–9.

[263] Yang Y, Xu YX, Chen L, Mayrhofer PH. Improved Ti-Al-N coatings through Ta alloying and multilayer architecture. Surf Coat Technol 2017;328:428–35.

[264] Seidl WM, Bartosik M, Kolozsvári S, Bolvardi H, Mayrhofer PH. Influence of coating thickness and substrate on stresses and mechanical properties of (Ti, Al, Ta)N/(Al, Cr)N multilayers. Surf Coat Technol 2018;347:92–8.

[265] Petrov I, Barna PB, Hultman L, Greene JE. Microstrtuctural evolution during film growth. J Vac Sci Technol A 2003;21(5):117–28.

[266] Ebner AS, Jakob S, Clemens H, Pippan R, Maier-Kiener V, He S, et al. Grain boundary segregation in Ni-base alloys: a combined atom probe tomography and first principles study. Acta Mat 2021;221:117354.

[267] Hans M, Music D, Chen Y-T, Patterer L, Eriksson AO, Kurapov D, et al. Crystallite size-dependent metastable phase formation of TiAlN coatings. Sci Rep 2017;7:16096.

[268] Mayrhofer PH, Rachbauer R, Holec D. Influence of Nb on the phase stability of Ti–Al–N. Scripta Mater 2010;63:807–10.

[269] Euchner H, Mayrhofer PH. Vacancy dependent stability of cubic and wurtzite $Ti_{1-x}Al_xN$. Surf Coat Technol 2015;275:214–8.

[270] Mayrhofer PH, Mitterer C. Structure/property relations in PVD hard coatings, in Recent Research Developments in Vacuum Science & Technology, Vol. 4 edited by S.G. Pandalai (Transworld Research Network, Trivandrum, 2003) 71–97 ISBN: 81-7895-067-7.

[271] Koller CM, Marihart H, Bolvardi H, Kolozsvári S, Mayrhofer PH. Structure, phase evolution, and mechanical properties of DC, pulsed DC, and high power impulse magnetron sputtered Ta–N films. Surf Coat Technol 2018;347:304–12.

[272] Klimashin FF, Lobmaier L, Koutná N, Holec D, Mayrhofer PH. The MoN–TaN system: Role of vacancies in phase stability and mechanical properties. Mater Des 2021;202(109568):1–12.

[273] Koutna N, Holec D, Friák M, Mayrhofer PH, Šob M. Stability and elasticity of metastable solid solutions and superlattices in the MoN-TaN system: First-principles calculations. Mater Des 2018;144:310–22.

[274] Saha B, Lawrence SK, Schroeder JL, Birch J, Bahr DF, Sands TD. Enhanced hardness in epitaxial TiAlScN alloy thin films and rocksalt TiN/(Al, Sc)N superlattices. Appl Phys Lett 2014;105:151904.

[275] Pei F, Xu YX, Chen L, Du Y, Zou HK. Structure, mechanical properties and thermal stability of $Ti_{1-x}Si_xN$ coatings. Ceram Int 2018;44:15503–8.

[276] Jiang N, Shen YG, Zhang HJ, Bao SN, Hou XY. Superhard nanocomposite Ti–Al–Si–N films deposited by reactive unbalanced magnetron sputtering. Mater Sci Eng B 2006;135:1–9.

[277] Pei F, Liu HJ, Chen L, Xu YX, Du Y. Improved properties of TiAlN coating by combined Si-addition and multilayer architecture. J Alloys Compd 2019;790:909–16.

[278] Söderber H, Odén M, Molina-Aldareguia JM, Hultman L. Nanostructure formation during deposition of TiN/SiNx nanomultilayer films by reactive dual magnetron sputtering. J Appl Phys 2005;97:114327.

[279] Barshilia HC, Deepthi B, Rajam KS, Bhatti KP, Chaudhary S. Growth and characterization of TiAlN/CrAlN superlattices prepared by reactive direct current magnetron sputtering. J Vac Sci Technol A 2009;27(1):29–36.

[280] Park J-K, Ziebert C, Stüber M, Baik Y-J. Improvement of hardness and toughness of TiAlN coating by nanoscale multilayered structurization with Si_3N_4. Plasma Process Polym 2007;4:902–5.

[281] Schlögl M, Mayer B, Paulitsch J, Mayrhofer PH. Influence of CrN and AlN layer thicknesses on structure and mechanical properties of CrN/AlN superlattices. Thin Solid Films 2013;545:375–9.

[282] Hao SQ, Delley B, Veprek S, Stampfl C. Superhard nitride-based nanocomposites: role of interfaces and effect of impurities. Phys Rev Lett 2006;97:086102.

[283] Veprek S, Argon AS, Zhang RF. Origin of the hardness enhancement in superhard nc-TiN/a-Si_3N_4 and ultrahard nc-TiN/a-Si_3N_4/$TiSi_2$ nanocomposites. Philos Mag Lett 2007;87:955–66.

[284] Kauffmann F, Baohua J, Dehm G, Gao H, Arzt E. A quantitative study of the hardness of a superhard nanocrystalline titanium nitride/silicon nitride coating. Scripta Mater 2005;52:1269–74.

[285] Barna PB, Adamik M. Formation and characterisation of the structure of surface coatings. In: Protective Coatings and Thin Films: Synthesis, Characterisation and Applications NATO ASI Series, 3. High Technology, Vol.21, (1997) (Eds.: Y.Pauleau and P.B.Barna, Kluwer Academic Publishers, Netherlands) pp.279–297. (Proc. NATO HTECH.ARW 950730, 1996, Portimao, Algarve, Portugal).

[286] Barna PB, Adamik M. Fundamental structure forming phenomena of polycrystalline films and the structure zone models. Thin Solid Films 1998;317:27–33.

[287] Liu ZR, Pei F, Chen L, Mayrhofer PH. Effect of Si-addition on structure and thermal stability of Ti-Al-N coatings. J Alloys Compd 2022;917:165483.

[288] Fischer-Cripps AC, Bull SJ, Schwarzer N. Critical review of claims for ultra-hardness in nanocomposite coatings. Philos Mag 2012;92:1601–30.

[289] Brazhkin VV, Solozhenko VL. Myths about new ultrahard phases: Why materials that are significantly superior to diamond in elastic moduli and hardness are impossible. J Appl Phys 2018;125:130901.

[290] Chu X, Barnett SA. Model of superlattice yield stress and hardness enhancements. J Appl Phys 1995;77:4403–11.

[291] Barnett S, Madan A. Superhard Superlattices. Phys World 1998;11:45–8.

[292] Pacher F, Mayrhofer PH, Holec D. Vacancy-driven extended stability of cubic metastable Ta-Al-N and Nb-Al-N phases. Surf Coat Technol 2017;326:37–44.

[293] Rovere F, Music D, To Baben M, Fuss H-G, Mayrhofer PH, Schneider JM. Experimental and computational study on the phase stability of Al-containing cubic transition metal nitrides. J Phys D: Appl Phys 2010;43(3):035302.

[294] Mayrhofer PH, Willmann H, Reiter AE. Structure and phase evolution of Cr-Al-N during annealing. Surf Coat Technol 2008;202:4935–8.

[295] Rachbauer R, Stergar E, Massl S, Moser M, Mayrhofer PH. Three-dimensional atom probe investigations of Ti–Al–N thin films. Scripta Mater 2009;61:725–8.

[296] Kretschmer A, Holec D, Yalamanchili K, Rudigier H, Hans M, Schneider JM, et al. Strain-stabilized Al-containing high-entropy sublattice nitrides. Acta Mater 2022;224:117483.

[297] Pshyk OV, Li X, Petrov I, Sangiovanni DG, Palisaitis J, Hultman L, et al. Discovery of Guinier-Preston zone hardening in refractory nitride ceramics. Acta Mater 2023;255:119105.

[298] Kretschmer A, Kirnbauer A, Moraes V, Primetzhofer D, Yalamanchili K, Rudigier H, et al. Improving phase stability, hardness, and oxidation resistance of reactively magnetron sputtered (Al, Cr, Nb, Ta, Ti)N thin films by Si-alloying. Surf Coat Technol 2021;416:127162.

[299] Darken LS, Gurry RW. Physical Chemistry of Metals. New York: McGraw-Hill; 1953.

[300] Trethewey KR, Chamberlain J. Corrosion for Science and Engineering. 2nd ed. Longman Group Ltd: Singapore; 1995.

[301] Roberge PR. Handbook of Corrosion Engineering, 3rd ed. McGraw-Hill Education: New York 2019. ISBN: 9781260116977.

[302] Hindam H, Whittle DP. Microstructure, adhesion and growth kinetics of protective scales on metals and alloys. Oxid Met 1982;18:245–84.

[303] Birks N, Meier GH. Introduction to High Temperature Oxidation of Metals. London: Edward Arnold Ltd; 1983.

[304] Ashby MF, Jones DRH. Engineering Materials 1. Oxford: Butterworth-Heinemann; 1996.

[305] Korb LJ (Ed). Corrosion, Vol 13. In: ASM Metals Handbook, 9th ed. ASM International, Materials Park: Ohio, 1987. ASTM D2688-11.

[306] In PB. Landolt-Börnstein – Group IV Physical Chemistry. In: Madelung O, editor. Numerical Data and Functional Relationships in Science and Technology, Ac–Au – Au–Zr. Berlin Heidelberg: Springer; 1991.

[307] Predel B. In: Landolt-Börnstein – Group IV Physical Chemistry, Madelung O (Ed). Numerical Data and Functional Relationships in Science and Technology, Cr–Cs – Cu–Zr. Springer: Berlin Heidelberg; 1994.

[308] Haynes WM, ed. (2011). CRC Handbook of Chemistry and Physics (92nd ed.). Boca Raton, FL: CRC Press. ISBN 1-4398-5511-0.

[309] Predel B. In Landolt-Börnstein – Group IV Physical Chemistry, Madelung O (Ed). Numerical Data and Functional Relationships in Science and Technology, Dy–Er – Fr–Mo. Springer: Berlin Heidelberg, 1995.

[310] Hagel WC. Factors controlling the high-temperature oxidation of chromium. Trans Am Soc Metals 1963;56:583–99.

[311] Giggins CS, Pettit FS. The oxidation of TD NiC (Ni-20Cr-2 vol pct ThO2) between 900° and 1200°C. Metall Trans 1971;2:1071–8.

[312] Lillerud KP, Kofstad P. On high temperature oxidation of chromium: I. Oxidation of annealed, thermally etched chromium at 800°–1100°C. J Electrochem Soc 1980;127:2397–410.

[313] Kofstad P, Lillerud KP. On high temperature oxidation of chromium: II. Properties of Cr_2O_3 and the oxidation mechanism of chromium. J Electrochem Soc 1980;127:2410–9.

[314] Kofstad P, Lillerud KP. Chromium transport through Cr_2O_3 scales: I. On lattice diffusion of chromium. Oxid Met 1982;17:177–94.

[315] Lillerud KP, Kofstad P. Chromium transport through Cr_2O_3 scales: II. Changes in scale morphology during high vacuum treatment of oxidized chromium specimens. Oxid Met 1982;17:195–203.

[316] Atkinson A, Taylor RI, Hughes AE. A quantitative demonstration of the grain boundary diffusion mechanism for the oxidation of metals. Philos Mag A 1982;45:823–33.

[317] Caplan D, Sproule GI. Effect of oxide grain structure on the high-temperature oxidation of Cr. Oxid Met 1975;9:459–72.

[318] Quadakkers WJ, Holzbrecher H, Briefs KG, Beske H. Differences in growth mechanisms of oxide scales formed on ODS and conventional wrought alloys. Oxid Met 1989;32:67–88.

[319] Young EWA, De Wit JHW. The use of a ^{18}O tracer and Rutherford backscattering spectrometry to study the oxidation mechanism of NiAl. Solid State Ion 1985;16:39–46.

[320] Ben Abderrazik G, Moulin G, Huntz AM, Young EWA, De Wit JHW. Growth mechanism of Al_2O_3 scales developed on Fe Cr Al alloys. Solid State Ion 1987;22:285–94.

[321] Reddy KPR, Smialek JL, Cooper AR. ^{18}O Tracer studies of Al_2O_3 scale formation on NiCrAl alloys. Oxid Met 1982;17:429–49.

[322] Stroosnijder MF, Sunderkötter JD, Cristóbal MJ, Jenett H, Isenbügel K, Baker MA. The influence of yttrium ion implantation on the oxidation behaviour of powder metallurgically produced chromium. Surf Coat Technol 1996;83:205–11.

[323] Hagel WC. Anion Diffusion in α-Cr_2O_3. J Am Ceram Soc 1965;48:70–5.

[324] Oishi Y, Kingery WD. Self-diffusion of oxygen in single crystal and polycrystalline aluminum oxide. J Chem Phys 1960;33:480–6.

[325] Prescott R, Graham MJ. The formation of aluminum oxide scales on high-temperature alloys. Oxid Met 1992;38:233–54.

[326] Über TG, von Metallen A. Z Anorg Allg Chem 1920;111(1):78–89.

[327] Wagner C. Beitrag zur Theorie des Anlaufvorgangs. Z Phys Chem 1933;21B:25–41.

[328] Tammann G, Köster W. Die Geschwindigkeit der Einwirkung von Sauerstoff, Schwefelwasserstoff und Halogenen auf Metall. Z Anorg Allg Chem 1922;123(1):196–224.

[329] Fick A. Ueber diffusion. Ann Phys 1855;94:59–86.

[330] Atkinson A. Transport processes during the growth of oxide films at elevated temperature. Rev Mod Phys 1985;57(2):437–70.

[331] Cabrera N, Mott NF. Theory of the oxidation of metal. Rep Prog Phys 1949;12:163–84.

[332] Quadakkers WJ, Naumenko D, Wessel E, Kochubey V, Singheiser L. Growth rates of alumina scales on Fe–Cr–Al Alloys. Oxid Met 2004;61:17–37.

[333] Gulbransen EA, Andrew KF. Kinetics of the oxidation of chromium. J Electrochem Soc 1957;104:334–8.

[334] Tedmon CSJ. The effect of oxide volatilization on the oxidation kinetics of Cr and Fe-Cr alloys. J Electrochem Soc 1966;113:766–8.

[335] Mayrhofer PH, Willmann H, Mitterer C. Oxidation kinetics of sputtered Cr-N coatings. Surf Coat Technol 2001;146–147:222–8.

[336] Grabke HJ. Oxidation of aluminides. Mater Sci Forum 1997;251–254:149–61.

[337] Stott FH. The oxidation of alumina-forming alloys. Mater Sci Forum 1997;251–254:19–32.

[338] Graham MJ, Eldrige JI, Mitchell DF, Hussey RJ. Anion transport in growing Cr_2O_3 scales. Mater Sci Forum 1989;43:207–42.

[339] Van Manen PA, Young EWA, Schalkoord D, van der Wekken CJ, De Wit JHW. The influence of Y on the structure and growth mechanism of alumina scales. Surf Interface Anal 1988;12:391–6.

[340] Rybicki GC, Smialek JL. Effect of the θ-α-Al_2O_3 transformation on the oxidation behavior of β-NiAl + Zr. Oxid Met 1989;31:275–304.

[341] Leyens C. Oxidation and Protection of Titanium Alloys and Titanium Aluminides. In: Leyens C, Peters M, editors. Titanium and Titanium Alloys. WILEY-VCH: Köln; 2003.

[342] Pettit FS, Meier GH. Oxidation and Hot Corrosion of Superalloys. In: Fifth International Symposium on Superalloys. The metallurgical Society of AIME: Seven Springs; 1984.

[343] Pilling NB, Bedworth RE. The oxidation of metals at high temperature. J Inst Met 1923;29:529–91.

[344] Hollerweger R, Riedl H, Arndt M, Kolozsvari S, Primig S, Mayrhofer PH. Guidelines for increasing the oxidation resistance of Ti-Al-N based coatings. Thin Solid Films 2019;688:137290.

[345] Hanaor DAH, Sorrell CC. Review of the anatase to rutile phase transformation. J Mater Sci 2010;46:855–74.

[346] Muscat J, Swamy V, Harrison N. First-principles calculations of the phase stability of TiO_2. Phys Rev B 2002;65:224112.

[347] Mayrhofer PH, Rovere F, Moser M, Strondl C, Tietema R. Thermally induced transitions in CrN thin films. Scripta Mater 2007;57:249–52.

[348] Mayrhofer PH, Willmann H, Hultman L, Mitterer C. Influence of different atmospheres on the thermal decomposition of Al-Cr-N. J Phys D: Appl Phys 2008;41:155316.

[349] Willmann H, Mayrhofer PH, Beschliesser M, Mitterer C. Thermal stability of sputtered nanocrystalline hard coatings. Pract Metallogr 2004;41(8):397–408.

[350] Chen H-Y, Lu F-H. Oxidation behavior of chromium nitride films. Thin Solid Films 2006;515:2179–84.

[351] Ichimura H, Kawana A. High temperature oxidation of ion-plated CrN films. J Mater Res 1994;9:151–5.

[352] Hagel WC, Seybolt AU. Cation diffusion in Cr_2O_3. J Electrochem Soc 1961;108:1146–52.

[353] Lindner R, Åkerström Å. Selbstdiffusion und Reaktion in Oxyd- und Spinellsystemen. Z Phys Chem 1956;6:162–77.

[354] Hofmann S, Jehn HA. Oxidation behavior of CrN and (Cr, AI)N hard coatings. Werkst Korros 1990;41:756–60.

[355] Young DJ, Cohen M. Oxidation behavior of chromium between 300° and 600°C. J Electrochem Soc 1977;124:769–74.

[356] Hofmann S. Formation and diffusion properties of oxide films on metals and on nitride coatings studied with auger electron spectroscopy and x-ray photoelectron spectroscopy. Thin Solid Films 1990;193:648–64.
[357] Üstel F, Mayrhofer PH, Mitterer C. The influence of the ion bombardment conditions on the oxidation behavior of sputtered TiN coatings. Pract Metallogr 2002;39(11):587–98.
[358] Hollerweger R, Riedl H, Paulitsch J, Arndt M, Rachbauer R, Polcik P, et al. Origin of high temperature oxidation resistance of Ti-Al-Ta-N coatings. Surf Coat Technol 2014;257:78–86.
[359] Koller CM, Hollerweger R, Sabitzer C, Rachbauer R, Polcik P, Paulitsch J, et al. Thermal stability and oxidation resistance of arc evaporated TiAlN, TaAlN, TiAlTaN, and TiAlN/TaAlN coatings. Surf Coat Technol 2014;259:599–607.
[360] Chen L, He L, Xu Y, Zhou L, Pei F, Du Y. Influence of ZrN on oxidation resistance of Ti–Al–N coating. Surf Coat Technol 2014;244:87–91.
[361] Xu YX, Riedl H, Holec D, Chen L, Du Y, Mayrhofer PH. Thermal stability and oxidation resistance of sputtered Ti-Al-Cr-N hard coatings. Surf Coat Technol 2017;324:48–56.
[362] Kretschmer A, Mayrhofer PH. High-temperature oxidation resistance of sputtered (Al,Cr,Nb,Ta,Ti,Si)N coatings. 2024:in revision.
[363] Seidl WM, Bartosik M, Kolozsvári S, Bolvardi H, Mayrhofer PH. Improved mechanical properties, thermal stabilities, and oxidation resistance of arc evaporated Ti-Al-N coatings through alloying with Ta. Surf Coat Technol 2018;344:244–9.
[364] Aschauer E, Wojcik T, Polcik P, Hunold O, Arndt M, Dalbauer V, et al. Ultra-high oxidation resistance of nano-structured thin films. Mater Des 2021;201:109499.
[365] Koller CM, Glatz SA, Kolozsvári S, Bolvardi H, Mayrhofer PH. Thermal stability and oxidation resistance of architecturally designed Ti-Al-N and Ti-Al-Ta-N-based coatings. Surf Coat Technol 2020;385:125444.
[366] Zhang J, Chen L, Kong Y, Hu C, Liu Z, Du Y, et al. Microstructure, mechanical and thermal properties of TiAlTaN/TiAlSiN multilayer. Vacuum 2021;187:110138.
[367] Leyens C. In: Peters M, editor. Titanium and Titanium Alloys. Wiley-VCH: New York; 2003.
[368] Wu Q, Li D, Hou Y, Wu L, Fu X, Wang X. Study of relationship between surface transient photoconductivity and liquid-phase photocatalytic activity of titanium dioxide. Mater Chem Phys 2007;102:53–9.
[369] Wang J, Mishra AK, Zhao Q, Huang L. Size effect on thermal stability of nanocrystalline anatase TiO_2. J Phys D Appl Phys 2013;46:255303.
[370] Kirillova SA, Almjashev VI, Stolyarova VL. Phase equilibria and materials in the TiO_2–SiO_2–ZrO_2 system: a review. Nanosyst Phys Chem Math 2021;12(6):711–27.
[371] Kaufman L. Calculation of multicomponent ceramic phase diagrams. Physica B+C 1988;150(1–2):99–114.
[372] McMurdie HF, Hall FP. Phase diagrams for ceramists: Supplement No 1. J Am Ceram Soc 1949;32(s1):154–64.
[373] Heimann RB. Classic and Advanced Ceramics: From Fundamentals to Applications. John Wiley & Sons; 2010.
[374] Simondon E, Giroux P-F, Chaffron L, Fitch A, Castany P, Gloriant T. Mechanical synthesis of nanostructured $Y_2Ti_2O_7$ pyrochlore oxides. Solid State Sci 2018;85:54–9.
[375] Hofmann S, Jehn HA. Selective oxidation and chemical state of Al and Ti in (Ti, Al)N coatings. Surf Interface Anal 1988;12:329–33.
[376] Lavrenko VA, Alexeev AF. Oxidation of sintered aluminium nitride. Ceram Int 1983;9:80–2.
[377] Katnani AD, Papathomas KI. Kinetics and initial stages of oxidation of aluminum nitride: thermogravimetric analysis and x-ray photoelectron spectroscopy study. J Vac Sci Technol A 1987;5:1335–40.
[378] Münster A. Über die Oxydation metallischer Hartstoffe. Z Elektrochem 1959;63:807–18.
[379] Bradt RC, Munz D, Sakai M, Shevchenko VYa, White KW. Fracture Mechanics of Ceramics: Volume 13. Crack-Microstructure Interaction, R-Curve Behavior, Environmental Effects in Fracture, and Standardization. Springer; 2002.
[380] Launey ME, Ritchie RO. On the fracture toughness of advanced materials. Adv Mater 2009;21:2103–210.
[381] Kiener D, Han SM. 100 years after Griffith: From brittle bulk fracture to failure in 2D materials. MRS Bulletin 2022;47:792–9.
[382] Clarke DR, Faber KT. Fracture of ceramics and glasses. J Phys Chem Solids 1987;48:1115–57.
[383] Zhu T, Li J. Ultra-strength materials. Prog Mater Sci 2010;55:710–57.
[384] Quinn GD. Strength and Proof Testing, Ceramics and Glasses, Vol 4. In: Engineering Materials Handbook, ASM International, 1991:585–598.
[385] Griffith AA. The Phenomena of Rupture and Flow in Solids. Philos Trans R Soc A 1921;221:163–98.
[386] Lawn B. Fracture of Brittle Solids. Cambridge University Press; 1993.
[387] Toughness AKE. Hardness, and Wear, Ceramics and Glasses. In: Schneider SJ, editor. Engineered Materials Handbook, Vol 4. ASM International; 1991. p. 599–609.
[388] Irwin GR. Fracture. In: Flügge S, editor. Encyclopedia of physics, Vol 6. Springer: Berlin; 1958. p. 551–90.
[389] Danzer R, Lube T, Supancic P, Damani R. Fracture of Ceramics Adv Eng Mater 2008;10:275–98.
[390] Ritchie RO. The conflicts between strength and toughness. Nat Mater 2011;10:817–22.
[391] Mechanical Testing and Evaluation, Vol 8. In: ASM Handbook. Kuhn H, Medlin D (Eds). ASM International; 2000.
[392] Pohl PM, Kümmel F, Schunk C, Serrano-Munoz I, Markötter H, Göken M, et al. About the role of interfaces on the fatigue crack propagation in laminated metallic composites. Materials 2021;14:2564.
[393] Butler EP. Transformation-toughened zirconia ceramics. Mater Sci Technol 1985;1:417–32.
[394] Piconi C, Maccauro G. Zirconia as a ceramic biomaterial. Biomater 1999;20:1–25.
[395] St G, Giese S, Merle B, Sprenger I, Heilmaier M, St N, et al. Microcantilever fracture tests on eutectic NiAl–Cr(Mo) in situ composites. Adv Eng Mater 2021;23:2001464.
[396] Wang C, Shi K, Gross C, Pureza JM, de Mesquita LM, Chung Y-W. Toughness enhancement of nanostructured hard coatings: design strategies and toughness measurement techniques. Surf Coat Technol 2014;257:206–12.
[397] Cordill MJ, Fischer FD, Rammerstorfer FG, Dehm G. Adhesion energies of Cr thin films on polyimide determined from buckling: experiment and model. Acta Mater 2010;58:5520–31.
[398] Schlögl M, Kirchlechner C, Paulitsch J, Keckes J, Mayrhofer PH. Effects of structure and interfaces on fracture toughness of CrN/AlN multilayer coatings. Scripta Mater 2013;68:917–20.
[399] Johansson CH, Linde JO. Röntgenographische Bestimmung der Atomanordnung in den Mischkristallreihen Au–Cu und Pd–Cu. Annalen der Physik 1925;383:439–60.
[400] Dehlinger U, Über GL. Umwandlungen von festen Metallphasen. I. Die tetragonale Gold=Kupferlegierung AuCu. Z Phys 1930;64:359–77.
[401] Dehlinger U. Über Umwandlungen von festen Metallphasen. III. Kinetik auf atomistischer Grundlage. Z Phys 1932;74:267–90.
[402] Über DU. Umwandlungen von festen Metallphasen. V. Berechnung kinetischer Kurven im System Au–Cu. Z Phys 1933;78:832–42.
[403] Esaki L, Tsu R. Superlattice and negative differential conductivity in semiconductors. IBM J Res Dev 1970;14:61–5.
[404] Koehler JS. Attempt to design a strong solid. Phys Rev B 1970;2:547–51.
[405] Lehoczky SL. Retardation of dislocation generation and motion in thin-layered metal laminates. Phys Rev Lett 1978;41:1814–8.
[406] Dai Y, Schubert J, Hollmann E, Mussler G, Wordenweber R. Engineering of the Curie temperature of epitaxial $Sr_{1-x}Ba_xTiO_3$ films via strain. J Appl Phys 2016;120:114101.
[407] Gao Z, Buchinger J, Koutná N, Wojcik T, Hahn R, Mayrhofer PH. Ab initio supported development of TiN/MoN superlattice thin films with improved hardness and toughness. Acta Mater 2022;231:117871.
[408] Buchinger J, Wagner A, Chen Z, Zhang ZL, Holec D, Mayrhofer PH, et al. Fracture toughness trends of modulus-matched TiN/(Cr, Al)N thin film Superlattices. Acta Mater 2021;202:376–86.
[409] Chen Z, Shao Q, Bartosik M, Mayrhofer PH, Chen H, Zhang Z. Growth-twins in CrN/AlN multilayers induced by hetero-phase interfaces. Acta Mater 2020;185:157–70.

[410] Fallmann M, Chen Z, Zhang ZL, Mayrhofer PH, Bartosik M. Mechanical properties and epitaxial growth of TiN/AlN superlattices. Surf Coat Technol 2019;375:1–7.
[411] Setoyama M, Nakayama A, Tanaka M, Kitagawa N, Nomura T. Formation of cubic-AIN in TiN/AIN superlattice. Surf Coat Technol 1996;86:225–30.
[412] Zhang R, Argon A, Veprek S. Friedel oscillations are limiting the strength of superhard nanocomposites and heterostructures. Phys Rev Lett 2009;102(1):015503.
[413] Koutná N, Řehák P, Chen Z, Bartosik M, Fallmann M, Černý M, et al. Correlating structural and mechanical properties of AlN/TiN superlattice films. Scripta Mater 2019;165:159–63.
[414] Řehák P, Černý M, Holec D. Interface-induced electronic structure toughening of nitride superlattices. Surf Coat Technol 2017;325:410–6.
[415] Helmersson U, Todorova S, Barnett SA, Sundgren J-E, Markert LC, Greene JE. Growth of single-crystal TiN/VN strained-layer superlattices with extremely high mechanical hardness. J Appl Phys 1987;62:481–4.
[416] Yashar PC, Sproul WD. Nanometer scale multilayered hard coatings. Vacuum 1999;55:179–90.
[417] Hurkmans T, Trinh T, Lewis DB, Brooks JS, Münz W-D. Multilayered titanium tungsten nitride coatings with a superlattice structure grown by unbalanced magnetron sputtering. Surf Coat Technol 1995;76(77):159–66.
[418] Hovsepian PE, Lewis DB, Münz WD, Lyon SB, Tomlinson M. Combined cathodic arc/unbalanced magnetron grown CrN/NbN superlattice coatings for corrosion resistant applications. Surf Coat Technol 1999;120(121):535–41.
[419] Sproul WD. Multilayer, multicomponent, and multiphase physical vapor deposition coatings for enhanced performance. J Vac Sci Technol A 1994;12:1595–601.
[420] Luo Q, Rainforth WM, Münz W-D. TEM observations of wear mechanisms of TiAlCrN and TiAlN/CrN coatings grown by combined steered-arc/unbalanced magnetron deposition. Wear 1999;225–229:74–82.
[421] Wiklund U, Hedenqvist P, Hogmark S. Multilayer cracking resistance in bending. Surf Coat Technol 1997;97:773–8.
[422] Hahn R, Bartosik M, Soler R, Kirchlechner C, Dehm G, Mayrhofer PH. Superlattice effect for enhanced fracture toughness of hard coatings. Scripta Mater 2016;124:67–70.
[423] Chen Z, Zheng Y, Löfler L, Bartosik M, Nayak GK, Renk O, et al. Atomic insights on intermixing of nanoscale nitride multilayer triggered by nanoindentation. Acta Mater 2021;214:117004.
[424] Koutná N, Löfler L, Holec D, Chen Z, Zhang Z, Hultman L, et al. Atomistic mechanisms underlying plasticity and crack growth in ceramics: a case study of AlN/TiN superlattices. Acta Mater 2022;229:117809.
[425] Koyama M, Noguchi H, Tsuzaki K. Microstructural Crack Tip Plasticity Controlling Small Fatigue Crack Growth. In: Tanaka I, Tsuji N, Inui H, editors. The Plaston Concept. Singapore: Springer; 2022.
[426] Rice JR, Thomson R. Ductile versus brittle behaviour of crystals. Phil Mag 1974;29:73–97.
[427] Rice JR. Dislocation nucleation from a crack tip: An analysis based on the Peierls concept. J Mech Phys Solid 1992;40:239–71.
[428] Zhang RF, Sheng SH, Veprek S. Mechanism of the B3 to B1 transformation in cubic AlN under uniaxial stress. Phys Rev B 2007;76:075208.
[429] Oyama ST. Introduction to the chemistry of transition metal carbides and nitrides. In: Oyama ST, editor. The Chemistry of Transition Metal Carbides and Nitrides. Dordrecht: Springer; 1996. p. 1–27.
[430] Pugh SXCII. Relations between the elastic moduli and the plastic properties of polycrystalline pure metals. Lond Edinb Dublin Philos Mag J Sci 1954;45:823–43.
[431] Lewandowski JJ, Wang WH, Greer AL. Intrinsic plasticity or brittleness of metallic glasses. Philos Mag Lett 2005;85:77–87.
[432] Pettifor D. Theoretical predictions of structure and related properties of intermetallics. Mater Sci Technol 1992;8:345–9.
[433] Sangiovanni DG, Hultman L, Chirita V. Supertoughening in B1 transition metal nitride alloys by increased valence electron concentration. Acta Mater 2011;59:2121–34.
[434] Kindlund H, Sangiovanni D, Lu J, Jensen J, Chirita V, Birch J, et al. Vacancy-induced toughening in hard single-crystal $V_{0.5}Mo_{0.5}N_x$/MgO (001) thin films. Acta Mater 2014;77:394–400.
[435] Niu H, Chen X-Q, Liu P, Xing W, Cheng X, Li D, et al. Extra-electron induced covalent strengthening and generalization of intrinsic ductile-to-brittle criterion. Sci Rep 2012;2:718.
[436] Thompson RP, Clegg WJ. Predicting whether a material is ductile or brittle. Curr Opin Solid State Mater Sci 2018;22:100–8.
[437] Christensen RM. The ductile/brittle transition, is it well posed and determinable. Proc R Soc A 2020;476:20190719.
[438] Christensen RM. Mechanisms and measures for the ductility of materials failure. Int J Eng Sci 2021;158:103424.
[439] Holec D, Zhou L, Riedl H, Koller CM, Mayrhofer PH, Friák M, et al. Atomistic modeling-based design of novel materials. Adv Eng Mater 2017;19(4):1600688.
[440] Kindlund H, Sangiovanni DG, Petrov I, Greene JE, Hultman L. A review of the intrinsic ductility and toughness of hard transition-metal nitride alloy thin films. Thin Solid Films 2019;688:137479.
[441] Corliss LM, Elliott N, Hastings JM. Antiferromagnetic Structure of CrN. Phys Rev 1960;117:929–36.
[442] Eddine MN, Sayetat F, Bertaut EF. Contribution à l'étude de CrN à basses temperatures par diffraction de rayons X et de neutrons. CR Acad Sci Ser B 1969;269:574–7.
[443] Almer J, Lienert U, Peng RL, Schlauer C, Odén M. Strain and texture analysis of coatings using high-energy x-rays. J Appl Phys 2003;94:697–702.
[444] Martinschitz KJ, Daniel R, Mitterer C, Keckes J. Elastic constants of fibre-textured thin films determined by X-ray diffraction. J Appl Crystallogr 2009;42:416–28.
[445] Zhou L, Körmann F, Holec D, Bartosik M, Grabowski B, Neugebauer J, et al. Structural stability and thermodynamics of CrN magnetic phases from ab initio and experiment. Phys Rev B 2014;90:184102.
[446] Balasubramanian K, Khare SV, Gall D. Valence electron concentration as an indicator for mechanical properties in rocksalt structure nitrides, carbides and carbonitrides. Acta Mater 2018;152:175–85.
[447] Zhou L, Holec D, Mayrhofer PH. Ab initio study of the alloying effect of transition metals on structure, stability and toughness of CrN. J Phys D Appl Phys 2013;46:365301.
[448] Alling B, Marten T, Abrikosov IA. Effect of magnetic disorder and strong electron correlations on the thermodynamics of CrN. Phys Rev B 2010;82:184430.
[449] Buchinger J, Koutná N, Kirnbauer A, Holec D, Mayrhofer PH. Heavy-element-alloying for toughness enhancement of hard nitrides on the example of Ti-W-N. Acta Mater 2022;231:117897.
[450] Buchinger J, Koutná N, Chen Z, Zhang Z, Mayrhofer PH, Holec D, et al. Toughness enhancement in TiN/WN superlattice thin films. Acta Mater 2019;172:18–29.
[451] Sangiovanni DG, Chirita V, Hultman L. Toughness enhancement in TiAlN-based quarternary alloys. Thin Solid Films 2012;520:4080–8.
[452] Wang AJ, Shang SL, Dua Y, Kong Y, Zhang LJ, Chen L, et al. Structural and elastic properties of cubic and hexagonal TiN and AlN from first-principles calculations. Comput Mater Sci 2010;48:705–9.
[453] Zhou L, Holec D, Mayrhofer PH. First-principles study of elastic properties of cubic $Cr_{1-x}Al_xN$ alloys. J Appl Phys 2013;113:043511.
[454] Sangiovanni DG, Chirita V, Hultman L. Electronic mechanism for toughness enhancement in $Ti_xM_{1-x}N$ (M=Mo and W). Phys Rev B 2010;81:105107.
[455] Jhi S-H, Louie SG, Cohen ML, Morris JW. Mechanical instability and ideal shear strength of transition metal carbides and nitrides. Phys Rev Lett 2001;87(7):075503.
[456] Leyland A, Matthews A. On the significance of the H/E ratio in wear control: a nanocomposite coating approach to optimised tribological behaviour. Wear 2000;246:1–11.
[457] Beake BD. The influence of the H/E ratio on wear resistance of coating systems – Insights from small-scale testing. Surf Coat Technol 2022;442:128272.
[458] Kamiya S, Hanyu H, Amaki S, Yanase H. Statistical evaluation of the strength of wear-resistant hard coatings. Surf Coat Technol 2007;202:1154–9.
[459] Massl S, Thomma W, Keckes J, Pippan R. Investigation of fracture properties of magnetron-sputtered TiN films by means of a FIB-based cantilever bending technique. Acta Mater 2009;57:1768–76.

[460] Matoy K, Schönherr H, Detzel T, Schöberl T, Pippan R, Motz C, et al. A comparative micro-cantilever study of the mechanical behavior of silicon based passivation films. Thin Solid Films 2009;518:247–56.

[461] Brinckmann S, Kirchlechner C, Dehm G. Stress intensity factor dependence on anisotropy and geometry during micro-fracture experiments. Scripta Mater 2017;127:76–8.

[462] Brinckmann S, Matoy K, Kirchlechner C, Dehm G. On the influence of microcantilever pre-crack geometries on the apparent fracture toughness of brittle materials. Acta Mater 2017;136:281–7.

[463] Saxena AK, Brinckmann S, Völker B, Dehm G, Kirchlechner C. Experimental conditions affecting the measured fracture toughness at the microscale: Notch geometry and crack extension measurement. Mater Des 2020;191:108582.

[464] Jaya BN, Jayaram V, Biswas SK. A new method for fracture toughness determination of graded (Pt, Ni)Al bond coats by microbeam bend tests. Philos Mag 2012;92:3326–45.

[465] Liu S, Wheeler JM, Howie PR, Zeng XT, Michler J, Clegg WJ. Measuring the fracture resistance of hard coatings. Appl Phys Lett 2013;102:171907.

[466] Sebastiani M, Johanns KE, Herbert EG, Carassitti F, Pharr GM. A novel pillar indentation splitting test for measuring fracture toughness of thin ceramic coatings. Philos Mag 2014;95:1928–44.

[467] Jaya BN, Kirchlechner Ch, Dehm G. Can microscale fracture tests provide reliable fracture toughness values? A case study in silicon. J Mater Res 2015;30:686–98.

[468] Zhang S, Zhang X. Toughness evaluation of hard coatings and thin films. Thin Solid Films 2012;520:2375–89.

[469] Zhang S, Sun D, Fu Y, Du H. Toughness measurement of thin films: a critical review. Surf Coat Technol 2005;198:74–84.

[470] Zhang T, Feng Y, Yang R, Jiang P. A method to determine fracture toughness using cube-corner indentation. Scripta Mater 2010;62:199–201.

[471] Söderberg H. Microstructural Characterization and Hardening Behavior of Reactive Magnetron Sputtered TiN/Si_3N_4 Multilayer Thin Films. Licenciate Thesis, 2004:58 | ISSN: 1402-1757 | ISRN: LTU-LIC – 04/58 – SE.

[472] Moriyama M, Aoki H, Kobayashi Y, Kamata K. The Mechanical Properties of Hot-Pressed TiN Ceramics with Various Additives. J Ceram Soc Jpn 1993;101:279–84.

[473] Kobayashi Y, Li J, Kawasaki A, Watanabe R. Microstructure and high-temperature property of reaction HIP-sintered SiC-AlN ceramic alloys. Mater Trans JIM 1996;37:807–12.

[474] Yonenaga I, Shima T, Sluiter MHF. Nano-indentation hardness and elastic moduli of bulk single-crystal AlN. Jpn J Appl Phys 2002;41:4620–1.

[475] Feng W, Yan D, He J, Zhang G, Chen G, Gu W, et al. Microhardness and toughness of the TiN coating prepared by reactive plasma spraying. Appl Surf Sci 2005;243:204–13.

[476] Wang YX, Zhang S, Lee JW, Lew WS, Li B. Influence of bias voltage on the hardness and toughness of CrAlN coatings via magnetron sputtering. Surf Coat Technol 2012;206:5103–7.

[477] Wang Q, Zhou F, Yan J. Evaluating mechanical properties and crack resistance of CrN, CrTiN, CrAlN and CrTiAlN coatings by nanoindentation and scratch tests. Surf Coat Technol 2016;285:203–13.

[478] Tanabe H, Miyoshi Y, Takamatsu T, Sugiura H. Effects of bias voltage and discharge current on mechanical properties of TiN film deposited by DC magnetron sputtering. Mater Sci Res Int 2003;9:143–8.

[479] Zhang Z, Ghasemi A, Koutná N, Xu Z, Grünstäudl T, Song K, et al. Correlating point defects with mechanical properties in nanocrystalline TiN thin films. Mater Des 2021;207:109844.

[480] Wei G, Bhushan B, Jacobs SJ. Nanoscale fatigue and fracture toughness measurements of multilayered thin film structures for digital micromirror devices. J Vac Sci Technol A 2004;22:1397–405.

[481] Kataria S, Srivastava SK, Kumar P, Srinivas G, Khan Siju J, Rao DVS, et al. Nanocrystalline TiN coatings with improved toughness deposited by pulsing the nitrogen flow rate. Surf Coat Technol 2012;206:4279–86.

[482] Wang A-N, Yu G-P, Huang J-H. Fracture toughness measurement on TiN hard coatings using internal energy induced cracking. Surf Coat Technol 2014;239:20–7.

[483] Scheu T. Impact of the change in power density by variations of the duty cycle on the properties of (Ti,Al)N HiPIMS coatings [unpublished diploma thesis, TU Wien University]. TU Wien Hauptbibliothek; 2021.

[484] Bartosik M, Böhm HJ, Krywka C, Zhang ZL, Mayrhofer PH. Influence of phase transformation on the damage tolerance of Ti-Al-N coatings. Vacuum 2018;155:153–7.

[485] Buchinger J, Löfler L, Ast J, Wagner A, Chen Z, Michler J, et al. Fracture properties of thin film TiN at elevated temperatures. Mater Des 2020;194:108885.

[486] Daniel R, Meindlhumer M, Zalesak J, Sartory B, Zeilinger A, Mitterer C, et al. Fracture toughness enhancement of brittle nanostructured materials by spatial heterogeneity: a micromechanical proof for CrN/Cr and TiN/SiO_x multilayers. Mater Des 2016;104:227–34.

[487] Daniel R, Meindlhumer M, Zalesak J, Baumegger W, Todt J, Ziegelwanger T, et al. Multi-scale interface design of strong and damage resistant hierarchical nanostructured materials. Mater Des 2020;196:109169.

[488] Moritz Y, Kainz Ch, Tkadletz M, Czettl Ch, Pohler M, Schalk N. Microstructure and mechanical properties of arc evaporated Ti(Al, Si)N coatings. Surf Coat Technol 2021;421:127461.

[489] Seidl WM, Bartosik M, Kolozsvári S, Bolvardi H, Mayrhofer PH. Influence of Ta on the fracture toughness of arc evaporated Ti-Al-N. Vacuum 2018;150:24–8.

[490] Best JP, Wehrs J, Polyakov M, Morstein M, Michler J. High temperature fracture toughness of ceramic coatings evaluated using micro-pillar splitting. Scripta Mater 2019;162:190–4.

[491] Völker B, Du C, Fager H, Rueß H, Soler R, Kirchlechner C, et al. How tensile tests allow a screening of the fracture toughness of hard coatings. Surf Coat Technol 2020;390:125645.

[492] Zauner L, Ertelthaler Ph, Wojcik T, Bolvardi H, Kolozsvári S, Mayrhofer PH, et al. Reactive HiPIMS deposition of Ti-Al-N: Influence of the deposition parameters on the cubic to hexagonal phase transition. Surf Coat Technol 2020;382:125007.

[493] Meindlhumer M, Zalesak J, Pitonak R, Todt J, Sartory B, Burghammer M, et al. Biomimetic hard and tough nanoceramic Ti–Al–N film with self-assembled six-level hierarchy. Nanoscale 2019;11:7986–95.

[494] Liu S, Wheeler JM, Davis CE, Clegg WJ, Zeng XT. The effect of Si content on the fracture toughness of CrAlN/Si_3N_4 coatings. J Appl Phys 2016;119:025305.

[495] Kainz Ch, Pohler M, Gruber GC, Tkadletz M, Ebner AS, Czettl Ch, et al. Influence of bias voltage on microstructure, mechanical properties and thermal stability of arc evaporated $Cr_{0.74}Ta_{0.26}N$ coatings. Surf Coat Technol 2021;417:127212.

[496] Drnovšek A, Vo HT, Rebelo de Figueiredo M, Kolozsvári S, Hosemann P, Franz R. High temperature fracture toughness of single-layer CrAlN and CrAlSiN hard coatings. Surf Coat Technol 2021;409:126909.

[497] Meindlhumer M, Ziegelwanger T, Zalesak J, Hans M, Löfler L, Spor S, et al. Precipitation-based grain boundary design alters Inter- to Trans-granular Fracture in AlCrN Thin Films. Acta Mater 2022;237:118156.

[498] Kolednik O, Predan J, Fischer FD, Fratzl P. Bioinspired design criteria for damage-resistant materials with periodically varying microstructure. Adv Funct Mater 2011;21:3634–41.

[499] Bartosik M, Hahn R, Zhang ZL, Ivanov I, Arndt M, Polcik P, et al. Fracture toughness of Ti-Si-N thin films. Int J Refract Hard Mater 2018;72:78–82.

[500] Sperr M, Zhang ZL, Ivanov YP, Mayrhofer PH, Bartosik M. Correlating elemental distribution with mechanical properties of TiN/SiN_x nanocomposite coatings. Scripta Mater 2019;170:20–3.

[501] Hahn R, Bartosik M, Arndt M, Polcik P, Mayrhofer PH. Annealing effect on the fracture toughness of CrN/TiN superlattices. Int J Refract Hard Mater 2018;71:352–6.

[502] Löfler L, Hahn R, Mayrhofer PH, Bartosik M, Holec D. Mechanical properties of CrN-based superlattices: impact of magnetism. Acta Mater 2021;218:117095.

[503] Hahn R, Koutna N, Wójcik T, Davydok A, Kolozsvári S, Krywka C, et al. Mechanistic study of superlattice-enabled high toughness and hardness in MoN/TaN coatings. Commun Mater 2020;1:62.

[504] Veprek S. Superhard and functional nanocomposites formed by self-organization in comparison with hardening of coatings by energetic ion bombardment during their deposition. Rev Adv Mater Sci 2003;5:6–16.
[505] Yang S, Guo T, Yan X, Gao K, Qiu J, Pang X. Nanotwinned transition metal nitride coating with excellent thermal stability. Acta Mater 2024;267:119743.
[506] Patel N, Wang S, Inspektor A, Salvador PA. Secondary hardness enhancement in large period TiN/TaN superlattices. Surf Coat Technol 2014;254:21–7.
[507] Huang Y, Chen Z, Wagner A, Mitterer A, Song K, Zhang Z. High density of stacking faults strengthened TaN/TiN multilayer. Acta Mater 2023;255:119027.
[508] Gludovatz B, Hohenwarter A, Catoor D, Chang EH, George EP, Ritchie RO. A fracture-resistant high-entropy alloy for cryogenic applications. Science 2014;345:1153–8.
[509] Luo H, Lu W, Fang X, Ponge D, Li Z, Raabe D. Beating hydrogen with its own weapon: Nano-twin gradients enhance embrittlement resistance of a high-entropy alloy. Mater Today 2018;21:1003–9.
[510] De Cooman BC, Estrin Y, Kim SK. Twinning-induced plasticity (TWIP) steels. Acta Mater 2018;142:283–362.
[511] Zhao S, Zhang R, Yu Q, Ell J, Ritchie RO, Minor AM. Cryoforged nanotwinned titanium with ultrahigh strength and ductility. Science 2021;373:1363–8.